Crystallographic and computational studies of organic non-linear optical materials

Turner, Michael James

Crystallographic and Computational Studies of Organic Non-linear Optical Materials

Michael James Turner

A Thesis presented for the degree of
Doctor of Philosophy

Department of Chemistry
University of Durham
England

June 2007

Dedicated to

my parents

Crystallographic and Computational Studies of Organic Non-linear Optical Materials

Michael James Turner

Submitted for the degree of Doctor of Philosophy
June 2007

Abstract

This thesis presents work on the determination of both linear and non-linear optical properties of organic molecular crystals from high-resolution X-ray diffraction data. The eventual goal of this work is to obtain accurate and reliable estimates of the non-linear optical properties for these materials of proven technological importance and to further our understanding of the factors affecting the relationship between molecular structure and macroscopic properties in order to aide our quest in designing new and better non-linear optical materials.

The basic theory of crystallography is discussed in Chapter 1, with a particular emphasis on obtaining accurate charge densities from high-resolution X-ray diffraction data. Chapter 2 summarises the theory behind modern quantum chemistry calculations for single molecules and periodic materials. Also introduced is the relatively new method for obtaining 'experimental' wavefunctions by constraining the wavefunction with structure factors obtained from X-ray diffraction experiments. This technique, devised by D. Jayatilaka, is the basis for much of the work carried out in this thesis. In Chapter 3, the definitions of the dipole (hyper)polarisabilities and related bulk susceptibilities are given along with a scheme for the calculation of approximate dipole polarisabilities attributed to Sylvain and Csizmadia.

Chapter 4 discusses the equations required for the calculation of dipole polarisabilities and hyperpolarisabilities derived from coupled-perturbed Hartree-Fock theory (CPHF). In addition, a scheme was presented for the calculation of refractive indices proposed by Rohleder and Munn. Routines for the calculation of these quan-

tities were implemented in the Tonto quantum chemistry package. This has allowed us for the first time to determine CPHF polarisabilities and hyperpolarisabilities from constrained wavefunction calculations.

Constrained wavefunction calculations were performed on three compounds, benzene, urea and 2-methyl-4-nitroaniline. CPHF polarisabilities and related refractive indices were calculated and compared with the Sylvain-Csizmadia values from the previous study by A.E. Whitten at the University of New England. The CPHF polarisabilities and refractive indices were comparable to experimental values and those obtained from the Sylvain-Csizmadia approach, but unfortunately no significant improvement was observed using the more rigorous CPHF approach.

Similar constrained wavefunction calculations were performed on three well known organic non-linear optical materials, 4-(*N*,*N*-dimethylamino)-3-acetamidonitrobenzene (DAN), 2-(*N*-L-prolinol)-5-nitropyridine (PNP) and (S)-2-(α-methylbenzylamino)-5-nitropyridine (MBANP), selected from the literature due to their importance in the field of non-linear optics. Enhancements in the calculated dipole polarisability, hyperpolarisability and refractive indices were observed after wavefunction fitting, which is attributed to the effects of the crystal field and intermolecular interactions included by way of the X-ray diffraction data. A comparison between the CPHF hyperpolarisabilities from wavefunction fitting and experimental values from EFISH (Electric Field Induced Second Harmonic generation) experiments, showed that the former were underestimated by on average 16.7 $\times 10^{-51} \mathrm{Cm}^3\mathrm{V}^{-2}$.

A comprehensive comparison of various properties determined from wavefunction fitting and multipole refinements of the *same* X-ray diffraction data, was reported in Chapter 6, in order to further our understanding of the effect of wavefunction fitting and the nature of the 'experimental' wavefunctions. Notable differences were observed between properties obtained from the multipole model and experimental wavefunction, with large differences observed for the electron densities of the atomic core regions.

Finally, Chapter 7 presents a charge-density study on the non-linear optical prototype material *N*,*N*-dimethyl-4-nitroaniline (NNDPNA). The multipole model obtained suggests a dipole moment enhancement of some 24 Debyes over that of the

isolated molecule. Unreasonable estimates for the electrostatic properties such as this, are thought to be the result of the limitations of using X-ray diffraction data alone to obtain accurate charge densities.

Declaration

The work in this thesis is based on research carried out at the Department of Chemistry at the University of Durham between September 2003 and June 2007 under the supervision of Professor Judith A. K. Howard. All the work is my own unless otherwise stated and no part of this thesis has been submitted elsewhere for any other degree or qualification at this or any other university.

Michael James Turner

Acknowledgements

It can take a lot of blood, sweat and tears to finish a Ph.D. One person who knows that more than anybody is my supervisor Professor Judith Howard who managed to keep the ship afloat despite all the odds. Thank you for all your support, encouragement and patience during my time in Durham and thank you also for giving the numerous opportunities to attend conferences around the world and for allowing me to spend a three-month sojourn in Australia.

I am indebted to Associate Professor Dylan Jayatilaka at the University of Western Australia for committing so much time, energy and inspiration to my work. Thank you also for the unrivalled hospitality during my stay in Perth.

I would also like to thank Sax Mason for his help and effort in my attempts to collect neutron diffraction data at the Institut Laue-Langevin and all of my new colleagues at the ILL who have supported and encouraged this endeavour, Dr David Tozer for many helpful discussions on the subtleties of quantum chemistry calculations, Dr Dmitrii Yufit for sharing his charge-density work on the compounds DAN, MBANP and PNP. Dr Alex Blatch for help with the synthesis of AANP and COANP, Dr Pedireddi and his students Sunil Varughese and Seetha Lekshmi for providing me with some very challenging crystals over the years, and finally many thanks to Dr Andrew Whitten and Professor Mark Spackman for involving me in their research.

Thanks to all the members, past and present, of the crystallography group at Durham, who have made my time there so memorable. Special mention goes to Dr Elinor Spencer for teaching me the basics of crystallography and also not forget-

ting Dr Andres Goeta who got me started on the study of organic non-linear optical materials way back in my undergraduate days.

Thanks to Adam, Ella and Katie with whom I've had so many great times in *and* out of the gym. Thanks also to Neil, Anna – two great housemates, to my friends down-under, Ben Corry, Rasha Ruhayel and Birger Dittrich for making me feel so welcome, and to the boys from the old days, Richard and Joe. And finally thanks go to Mike Probert and Gregg Capon, my two partners in crime. I've had many unforgettable adventures over the last four years with you two. Thank you Mike for keeping me sane during my Ph.D. (a difficult task I know) and also teaching me valuable lessons about generosity, friendship and above all drinking. And Gregg, I'm so grateful I've had the opportunity to renew my friendship with you. Thank you for reminding me not to take myself so seriously all the time.

And of course I would never have made it this far with my family. You are all never very far from my thoughts.

June 28, 2007

Contents

Abstract iii

Declaration vi

Acknowledgements vii

1 Introduction 1

1.1 Crystallography 1

1.1.1 X-ray Diffraction 1

1.1.2 Charge-Density Analysis 10

1.1.3 Neutron Diffraction 17

2 Introduction to Quantum-Chemistry Calculations 20

2.1 Hartree-Fock Theory 20

2.1.1 Restricted Hartree-Fock Wavefunction 21

2.1.2 Electronic Energy of the HF Wavefunction 22

2.1.3 Expansion of Orbitals in Terms of a Basis set 24

2.1.4 Solving the Schrödinger Equation 24

2.1.5 Interpretation and Analysis of the Wavefunction 28

2.1.6 Deficiencies of Hartree-Fock Theory 28

2.2 Periodic Hartree-Fock Calculations 29

2.2.1 Definition of the Basis-set 30

2.2.2 **k**-point Sampling 31

2.2.3 Integral Series Truncation 31

2.3 Experimental Wavefunctions 32

2.3.1 Constrained Wavefunction Fitting 32

3 Organic Non-linear Optical Materials: Stucture and Properties 36

3.1 Introduction 36

3.2 Definition of Dipole (Hyper)polarisabilities and Related Bulk Susceptibilities 37

3.3 Calculation of Dipole Polarisabilities and Hyperpolarisabilities 40

3.3.1 Approximate Polarisabilities (Sylvain and Csizmadia) 41

3.4 Organic Molecular Crystals as NLO Prototypes 44

3.5 Compounds of Interest 45

3.6 Outline of the Work 46

4 Solid-state Linear and Non-linear Optical Properties 49

4.1 Introduction 49

4.2 Coupled Perturbed Hartree-Fock Theory 51

4.2.1 Derivatives of the Molecular Orbitals 51

4.2.2 Hartree-Fock Energy (Electric-Field Case) 52

4.2.3 First-order CPHF Equations for Electric Fields 54

4.2.4 Second-order CPHF Equations for Electric Fields 55

4.3 Analytical Derivatives of the Hartree-Fock Energy 56

4.3.1 Dipole Moment 56

4.3.2 CPHF Polarisability 56

4.3.3 CPHF First-order Hyperpolarisability 59

4.4 Calculation of Refractive Indices 61

4.5 Implementation of Routines 62

4.6 Compounds of Interest 63

4.7 Fitting Calculations 64

4.7.1 Verification of the Code 65

4.8 Results 67

4.8.1 Benzene 67

4.8.2 Urea 70

4.8.3 MNA 73

4.9 Conclusions 75

5 A Series of Constrained Wavefunction-Fitting Calculations 77

5.1 Introduction 77

5.2 Details of the Calculations 78

5.3 Constrained Wavefunction Fitting of DAN 79

5.3.1 Properties of DAN 83

5.4 Constrained Wavefunction Fitting of MBANP 86

5.4.1 Properties of MBANP 89

5.5 Constrained Wavefunction Fitting of PNP 93

5.5.1 Properties of PNP 96

5.6 Hyperpolarisabilities: Comparison with Experiment 100

5.7 Conclusions 101

6 Wavefunction-Fitting Calculations and Charge Density: A Detailed Comparison 103

6.1 Introduction 103

6.2 Comparison of DAN 104

6.2.1 Results 106

6.3 Comparison of MBANP 110

6.3.1 Results 111

6.4 Comparison of PNP 116

6.4.1 Results 116

6.5 Conclusions 121

7 Charge-Density Study of NNDPNA 124

7.1 Introduction 124

7.2 Experimental 125

7.2.1 Data Reduction 126

7.2.2 Multipole Refinement 128

7.2.3 Results 129

7.3 Conclusions 136

8 Summary and Future Work **137**

8.1 Summary 137

8.2 Future Work 138

Appendix **140**

A Estimation of the Accuracies of the Calculated Properties **140**

B Hirshfeld Surfaces and Fingerprint Plots **144**

C Neutron Diffraction Study of NNDPNA **152**

D Programming Projects **159**

D.1 XtalCommander 159

D.2 HKL Tools 161

D.2.1 Framework: Crystallographic Objects and Associated Methods 161

D.2.2 Tools: Programs for Processing Datasets 164

D.3 Tontoprepare 164

D.4 xd2shelx 166

E DZP Basis Set Description **167**

F Synthesis of AANP and COANP **169**

F.1 AANP 170

F.2 COANP 173

G Personal Development **174**

G.1 Courses and Schools 174

G.2 Departmental Seminars 175

G.3 External Meetings and Conferences 176

G.4 Time Spent Away from Durham University 177

Bibliography **179**

List of Figures

1.1 Schematic of a four circle diffractometer 4
1.2 Plot of the scattering factor f against θ for a carbon atom 9
1.3 Schematic representations of the real spherical harmonic functions . . 12

3.1 Schematics of (a) prototypical organic NLO system (b) para-Nitroaniline 44
3.2 Schematics of (a) DAN (b) PNP (c) MBANP and (d) NNDPNA . . . 46

4.1 Schematic of (a) benzene (b) urea and (c) MNA 63

5.1 DAN: Details of the wavefunction fitting 82
5.2 Principal axes of the polarisability with respect to the orientation of a DAN molecule 84
5.3 MBANP: Details of the wavefunction fitting 88
5.4 Principal axes of the polarisability with respect to the orientation of a MBANP molecule 90
5.5 PNP: Details of the wavefunction fitting 95
5.6 Principal axes of the polarisability with respect to the orientation of a PNP molecule 96

6.1 Deformation density and negative Laplacian of the electron density of DAN 107
6.2 Electron localisation function and electrostatic potential of DAN . . . 108
6.3 Deformation density and negative Laplacian of the density of MBANP 112
6.4 Electron localisation function and electrostatic potential of MBANP . 114
6.5 Deformation density and negative Laplacian of the density of PNP . . 118
6.6 Electron localisation function and electrostatic potential of PNP . . . 119

7.1 The NNDPNA crystal mounted on the goniometer 126
7.2 Structure of NNDPNA with thermal ellipsoids at 50% probability level131
7.3 Packing diagram of NNDPNA 131
7.4 NNDPNA: Residual fourier density map for (a) κ refinement (b) κ' refinement 132
7.5 Deformation density and negative Laplacian of the density of NNDPNA133

B.1 Hirshfeld surface of DAN with the property d_e mapped onto the surface148
B.2 Fingerprint plot of DAN 148
B.3 Hirshfeld surface of MBANP with the property d_e mapped onto the surface 149
B.4 Fingerprint plot of MBANP 149
B.5 Hirshfeld surface of PNP with the property d_e mapped onto the surface150
B.6 Fingerprint plot of PNP 150
B.7 Hirshfeld surface of NNDPNA with the property d_e mapped onto the surface 151
B.8 Fingerprint plot of NNDPNA 151

C.1 Laue diffraction patterns of (a) Large Crystal (b) Small Crystal . . . 153
C.2 Neutron Structure of NNDPNA with thermal ellipsoids at the 50% probability level 154

D.1 Pseudocode for (a) Blocking Calculation (b) Non-blocking Calculation 160

F.1 Schematic of (a) AANP and (b) COANP 169
F.2 Structure of AANP with thermal ellipsoids at 50% probability level . 171
F.3 Packing diagram of AANP 171

List of Tables

1.1 Critical Points of the Electron Density 16

2.1 Basis sets utilised 24

3.1 Efficiency of Powder SHG activity relative to Urea. 46

4.1 Fitting statistics for the constrained wavefunctions performed on benzene, urea and MNA 65
4.2 Comparison and verification of SOS polarisabilities 66
4.3 Comparison and verification of CPHF polarisabilities 66
4.4 Comparison and verification of CPHF hyperpolarisabilities 67
4.5 Benzene: Dipole polarisabilities 68
4.6 Benzene: Dipole polarisability tensor 69
4.7 Benzene: Refractive indices 70
4.8 Urea: Dipole polarisabilities 71
4.9 Urea: Dipole polarisability tensor 71
4.10 Urea: Refractive indices 72
4.11 Urea: Dipole hyperpolarisability tensor 72
4.12 Urea: Vector dipole hyperpolarisability 72
4.13 MNA: Dipole polarisabilities 73
4.14 MNA: Dipole polarisability tensor 73
4.15 MNA: Refractive indices 74
4.16 MNA: Dipole hyperpolarisability tensor 74
4.17 MNA: Vector dipole hyperpolarisability 75

5.1 Fitting statistics for DAN 79

5.2 DAN: Dipole polarisabilities 83
5.3 DAN: Dipole polarisability tensor 83
5.4 DAN: Molecular orbital pair contributions to the polarisability 84
5.5 DAN: Refractive indices 85
5.6 DAN: Dipole hyperpolarisability tensor 86
5.7 DAN: Vector dipole hyperpolarisability 86
5.8 Fitting statistics for MBANP 87
5.9 MBANP: Dipole polarisabilities 89
5.10 MBANP: Dipole polarisability tensor 89
5.11 MBANP: Molecular-orbital-pair contributions to the polarisability . . 90
5.12 MBANP: Refractive indices 91
5.13 MBANP: Dipole hyperpolarisability tensor 92
5.14 MBANP: Vector dipole hyperpolarisability 92
5.15 Fitting statistics for PNP 93
5.16 PNP: Dipole polarisabilities 96
5.17 PNP: Dipole polarisability tensor 97
5.18 PNP: Molecular-orbital-pair contributions to the polarisability 97
5.19 PNP: Refractive indices 98
5.20 PNP: Dipole hyperpolarisability tensor 98
5.21 PNP: Vector dipole hyperpolarisability 99
5.22 Comparison of hyperpolarisabilities from experiment and wavefunction fitting 100

6.1 Details of the Charge-Density Experiment on DAN 105
6.2 Partial atomic charges for DAN 109
6.3 Comparison of the molecular dipole moments for DAN 110
6.4 Details of the Charge-Density Experiment on MBANP 111
6.5 Partial atomic charges for MBANP 115
6.6 Comparison of the molecular dipole Moment for MBANP 116
6.7 Details of the Charge-Density Experiment on PNP 117
6.8 Partial Atomic Charges for PNP 120
6.9 Comparison of the molecular dipole moment for PNP 121

7.1 Data-collection strategy for NNDPNA 127
7.2 Details of the charge-density experiment on NNDPNA 130
7.3 Fractional atomic coordinates of NNDPNA 132
7.4 Atomic displacement parameters of NNDPNA 133
7.5 Atomic partial charges of NNDPNA 134
7.6 Dipole moment of NNDPNA 135

A.1 MNA: Estimated errors in the dipole polarisabilities 142
A.2 MNA: Estimated errors in the dipole polarisability tensor 142
A.3 MNA: Estimated errors in the refractive indices 142
A.4 MNA: Estimated errors in the dipole hyperpolarisability tensor 143
A.5 MNA: Estimated errors in the vector dipole hyperpolarisability 143

B.1 Selected H$\cdots$O intermolecular contacts for NNDPNA and DAN . . . 147

C.1 Crystallographic details of the neutron-diffraction study on NNDPNA 155
C.2 Neutron fractional atomic coordinates of NNDPNA 156
C.3 Neutron atomic displacement parameters of NNDPNA 157
C.4 Neutron bond lengths for NNDPNA 158
C.5 Neutron bond angles for NNDPNA 158

D.1 Command-line options available in Tontoprepare 165
D.2 Default values for reflection omission in XD 166

F.1 Crystallographic details of the X-ray diffraction study on AANP . . . 172

Chapter 1

Introduction

This chapter provides an introduction to the themes, techniques and principles that are discussed later in subsequent chapters. The first section introduces the field of crystallography and in particular covers how crystallographers routinely determine the structures of crystalline materials. In addition, the more specialised areas of charge-density determination and neutron diffraction are discussed. In the second section, the main concepts behind quantum mechanics are introduced, focussing on their application to single-point energy calculations. The final section covers the area of organic non-linear optical materials which is the main focus of this thesis. No attempt has been made to cover these fields in the detail they truly deserve but where possible references to more comprehensive and thorough sources of information have been highlighted.

1.1 Crystallography

1.1.1 X-ray Diffraction

The interaction between electromagnetic radiation and matter is a considerable subject and of tantamount importance to our understanding of the world around us. One of the most useful aspects is the phenomenon of scattering of X-rays by crystalline materials. Crystals exhibit this behaviour because of their inherent symmetry; they are composed of a single structural motif which is repeated by translation

operations only to completely describe the material. Consequently the information contained in the X-ray diffaction pattern can be used to determine the three-dimensional arrangement of the atoms in this structural motif.

Due to their periodic nature, a simplified way to treat crystalline materials is to imagine them composed of planes of atoms with a fixed interplanar distance, d. The relationship between the scattering angle θ, of a scattered X-ray and the interplanar distance is described by the Bragg equation [1] (1.1).

$$n\lambda = 2d\sin\theta \tag{1.1}$$

Where λ is the wavelength of the radiation and n is an integer describing the condition of constructive interference of the scattered waves. It is by no accident that X-rays are chosen for the job of structure eulicidation given that its wavelength is of the order of interatomic bond distances. It is important to point out that X-rays are not scattered by 'atoms' themselves but by their electrons, a fact which has significant implications for charge-density determinations.

Typically three pieces of information are associated with each scattered X-ray (commonly called a reflection) namely, the scattering vector, the intensity of the reflection $I(hkl)$ and the relative phase angle of the reflection, $\alpha(hkl)$.

Equation 1.2 shows the relationship between the intensity of a reflection and its corresponding structure factor $F(hkl)$.

$$I(hkl) \propto |F(hkl)|^2 \tag{1.2}$$

The Miller indices (hkl), define the scattering vector, a quantity which specifies the direction of the scattered X-ray relative to the incident beam. These indices in effect provide a unique identifier for each reflection in a convenient and compact notation.

In order to be able to determine the crystal structure, it is necessary to have a set of structure factors, $F(hkl)$. From Equation 1.3, we can see that this requires knowing both the magnitude of the structure factor and its relative phase. With current diffractometer technology however, there is no known way of obtaining the phase information directly which results in what is known as the *phase problem.*

The phase information must therefore be derived by other means, forming the basis of the various structure solution methods, which are described briefly later.

$$F(hkl) = |F(hkl)|e^{i\alpha(hkl)} \tag{1.3}$$

The structure factors are related to the electron density $\rho(xyz)$ by a Fourier transform (1.4), a mathematical method of simulating the recombination of waves normally performed by a lens.

$$F(hkl) = \int \rho(xyz) \exp[2\pi i(hx + ky + lz)] \tag{1.4}$$

The inverse Fourier transform shows how the electron density and hence the arrangement of atoms in the crystal can be derived from a sum over the structure factors (1.5).

$$\rho(xyz) = \frac{1}{V_c} \sum_{hkl} F(hkl) \exp[-2\pi i(hx + ky + lz)] \tag{1.5}$$

Where V_c is the unit cell volume. It is interesting to note that each structure factor contains information about every point in the electron density and as such each point in the electron density requires a summation over *all* possible reflections. In order to reproduce perfectly every detail of the electron density, we would be required to measure a data set to an infinite resolution which is clearly not possible. Data with a limited resolution force a truncation of the summation in the Fourier transform resulting in series-termination errors with the effect of producing undesirable Fourier ripples in the Fourier map.

The following sections describe a typical procedure for routine structure determinations highlighting the sequence of steps carried out, along with discussions of the hardware and additional theory on which they depend.

Data Collection

Figure 1.1 shows a schematic of a four-circle X-ray diffractometer based on an Eulerian cradle, the archetypal machine used to collect X-ray diffraction data.

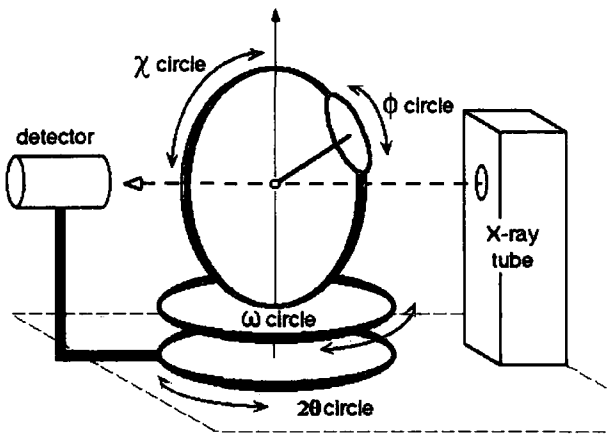

Figure 1.1: Schematic of a four circle diffractometer

The orientation of the crystal with respect to the incident beam is described by three angles, ω, χ and ϕ. In addition, the angle between the detector and the incident beam is specified by 2θ.

Reflections are measured by changing the orientation of the crystal until a reflection condition is met and then scanning through the reflection to record the peak profile. Integration of the peak profile gives the intensity for that reflection.

On modern diffractometers the point detector is often replaced by a position-sensitive detector, e.g. a Charged Coupled Device (CCD), which greatly increases the speed at which data can be collected since many reflections can be recorded simultaneously. As such, data collections differ with area detectors because the data are no longer collected on a per reflection basis but collected instead using a series of runs with the aim of scanning through as much of reciprocal space as the physical limitations of the machine allow.

Another important innovation is the use of low-temperature devices to cool the crystal. There are many benefits of collecting data at temperatures below ambient conditions including:

1. Reduction of crystal decay.

2. Boost in intensities.

3. Reduction of Thermal Diffuse Scattering(TDS).

4. Reduction of thermal motion and hence a reduction of libration effects.

5. Ability to investigate phase transitions.

For a thorough review of the use and benefits of low-temperature devices in X-ray diffraction experiments see Goeta et al [2]. The Crystallography Group at Durham University is at the forefront of low-temperature X-ray crystallographic research. The following two devices are routinely used: Oxford Cryosystems N_2 Cryostream [3] with a minimum temperature of 90K, and the HeliX, an open-flow He-based cryostat with a base temperature of 25K [4].

Determination of the Orientation Matrix

The orientation matrix **UB** [5], relates the orientation of the crystal, which is dependent on how the crystal is oriented on the mount, to a fixed reference coordinate system. Knowledge of the **UB** matrix is a necessary prerequisite if we want to determine the angles which brings a particular reflection **h** in a reflecting position or if we want to determine the Miller indices of a reflection which is in a reflecting position at some setting of the diffractometer circles. The matrix **B** relates the coordinate system of the reciprocal lattice[1] defined by the vectors $\mathbf{a}^*$, $\mathbf{b}^*$ and $\mathbf{c}^*$ to a set of orthonormal crystal axes. In turn, the matrix **U** relates this crystal coordinate system to a coordinate system fixed with respect to the ϕ-axis (i.e. the goniometer head of the diffractometer) and as such serves as our fixed reference.

Another important relationship is between the ϕ-axis coordinate system and that of a fixed laboratory axes system. The laboratory axes are typically fixed with respect to the incident beam. Therefore this relationship is defined by a rotation matrix **R** dependent upon the setting angles (1.6).

$$\mathbf{R} = \begin{pmatrix} \cos\phi\cos\omega - \sin\phi\sin\omega\cos\chi & \cos\phi\sin\omega + \sin\phi\cos\omega\cos\chi & \sin\phi\sin\chi \\ -\sin\phi\cos\omega - \cos\phi\sin\omega\cos\chi & -\sin\phi\sin\omega + \cos\phi\cos\omega\cos\chi & \cos\phi\sin\chi \\ \sin\chi\sin\omega & -\sin\chi\cos\omega & cos\chi \end{pmatrix} \tag{1.6}$$

[1]The reciprocal lattice of the real-space lattice is a set of reciprocal space vectors **K** such that $e^{i\mathbf{K}.\mathbf{R}} = 1$ for direct lattice-position vectors **R**

The unit cell is typically given in terms of six parameters, three lengths a, b and c and three related angles α, β and γ. These parameters can be extracted from the **UB** matrix using the following scheme:

$$(\mathbf{UB})^T\mathbf{UB} = \mathbf{B}^T\mathbf{U}^T\mathbf{UB} = \mathbf{B}^T\mathbf{B} = \mathbf{G}^{-1} \tag{1.7}$$

Where $\mathbf{G}^{-1}$ is the reciprocal space metric tensor. The corresponding real space metric tensor, $\mathbf{G}$ is defined in (1.8) from which it is trivial to calculate the unit cell parameters.

$$\mathbf{G} = \begin{pmatrix} a^2 & ab\cos\gamma & ac\cos\beta \\ ab\cos\gamma & b^2 & bc\cos\alpha \\ ac\cos\beta & bc\cos\alpha & c^2 \end{pmatrix} \tag{1.8}$$

Data Reduction and Correction

In order to extract intensities from area detector data, it is necessary to integrate the peaks found in the diffraction data. This is commonly done by fitted peak profiles usually divided into two classes, strong and weak, and then performing a subtraction of an averaged background. The raw intensities obtained must then be corrected for a number of factors shown by equation (1.9).

$$I_{hkl}^{corr} = \left(\frac{e^2}{mc^2}\right)^2 \frac{\lambda^3\Omega}{V^2} I_0 LPTE|F_{hkl}|^2 \tag{1.9}$$

Where L, the Lorentz factor, accounts for the fact that some reflections spend longer in positions which meet reflection conditions. P, the polarisation factor, accounts for the partial polarisation of scattered X-rays as a result of the interaction with the crystal. The transmission factor, T, accounts for absorption of X-rays by the crystal. The extinction factor, E, corrects for possible extinction effects. Furthermore, Ω is the volume of the crystal and V, the unit cell volume.

It has been shown experimentally that the counting statistics for scattered X-rays follows a Poisson distribution. This fact allows us to determine estimated standard deviations for each reflection which are then adjusted by machine-specific factors.

Space Group Determination

A crystallographic space group fully describes the symmetry of a periodic 3-dimensional object, of which there are 230 unique space groups [6]. The cell centering (P, A, B, C, F, I, R) and the presence of certain symmetry elements (e.g. screw axes and glide planes) result in certains classes of reflections having zero intensity. The presence of systematic absences can therefore be used to obtain valuable information about the crystal symmetry and as such can be used to narrow down to which space group a particular crystal belongs.

Having used the information contained in the systematic absences, we are often left with a choice between a centrosymmetric (centric) and a non-centrosymmetric (acentric) space group. Fortunately, centrosymmetric and non-centrosymmetric structures typically have characteristic distributions of normalised structure factors, E_H, which can be used to identify them. The relationship between the structure factors, F_H and E_H is given in Equation 1.10.

$$E_H = \frac{|F_H|}{\sqrt{\varepsilon \sum_{i=1}^{N} f_i^2}} \tag{1.10}$$

The normalisation procedure removes the angular dependance of scattering factors and results in what are effectively 'point' atoms.

Structure Solution

Due to the phase problem described earlier, the phase information is lost during the X-ray diffraction experiment and must be acquired by other means. Methods have been developed to circumvent the phase problem and obtain a structure solution, that is a set of initial phases and a resultant starting model. The two most commonly employed methods are the Patterson [7,8] and direct methods [9].

The Patterson method makes use of the Patterson synthesis (1.11), where peaks in the Patterson map correspond to vectors between pairs of atoms allowing information about the structure to be discerned. This technique is most suitable when the material contains a few heavy atoms, e.g. an organometallic material, or when the molecular structure is expected to have a well-defined rigid geometry, e.g. an

adamantyl cage.

$$P(uvw) = \frac{1}{V_c}\sum_{hkl}|F(hkl)|^2 \cos 2\pi(hu + kv + lw) \tag{1.11}$$

The technique of direct methods is more flexible and is the most common method used for structure solutions. It is based on the principles of positivity and atomicity, i.e. that the electron density is everywhere positive and that it is a superposition of discrete and isolated atoms. The phase information is obtained by making informed assumptions about the phase relationships between classes of reflections and by the use of the Tangent formula to allow the development of additional phases. It is important to realise that the structure solution only provides an crude initial model, very often with much of the structure missing.

A discussion of the additional problems of phase determination for non-centrosymmetric structures compared to centrosymmetric structures is included in Section 1.1.2.

Refinement

The final stage of a structure determination is the refinement of the model. In standard crystallographic software the model is treated using a spherical-atom approximation known as the Independent Atom Model (IAM) (1.12).

$$F(hkl) = \sum_j f_j(hkl)T_j(hkl)\exp[2\pi i(hx_j + ky_j + lz_j)] \tag{1.12}$$

In this approximation the contribution by each atom j, in the model is represented by a scattering factor $f_j(r)$, which for X-ray diffraction experiments is calculated by a Fourier-Bessel transformation of the atomic electron density (1.13).

$$f_j(r^*) = \int_0^\infty U_j(r)\frac{\sin(2\pi r r^*)}{2\pi r r^*}\mathrm{d}r \tag{1.13}$$

Where $r^* = 2\sin\theta/\lambda$ and $U_j(r) = 4\pi r^2\rho_j(r)$, which represents the radial distribution function for atom j. One important aspect of scattering factors is their angular dependance which is shown in Figure (1.2). It is the high-angle data which contain the information about the atomic positions since the core density is compact

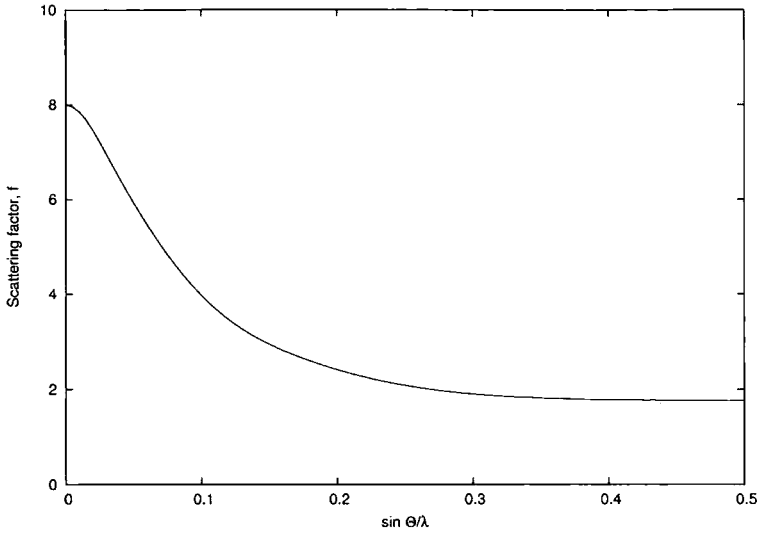

Figure 1.2: Plot of the scattering factor f against θ for a carbon atom

in real space and is therefore diffuse in reciprocal space. A converse argument holds for the bonding density, the information for which is consequently mostly contained in the low-angle data.

In Equation (1.12), a correction $T_j(hkl)$, to account for the motion of the atoms in the crystal is also included and explains why an increase in intensities is observed when the temperature of the crystal is lowered. This temperature factor (1.14), is dependent upon a third-rank tensor U, which describes the anisotropy of the thermal motion and is commonly represented as "thermal ellipsoids" in diagrams of crystal structures.

$$T_j(\mathbf{h}) = e^{-2\pi^2 \mathbf{h}^t \mathbf{U}_j \mathbf{h}} \tag{1.14}$$

The refinement process is in fact composed of two distinct steps, namely least squares refinement and updating the model from the Fourier difference map. In the former step, the parameters of the model are adjusted with the aim of minimising some function, typically of the form given in Equation 1.15.

$$\Delta = \sum w(F_o^2 - F_c^2)^2 \tag{1.15}$$

Where w is a weighting factor, usually a function of the estimated standard deviation and thus reflecting our confidence in the measurement. F_o are the observed

data and F_c are the structure factors calculated from the model.

After each round of refinement a Fourier difference map is created $|F_o - F_c|$. The peaks in this map should correspond mainly to parts of the molecular model that are missing, which are then incorporated as new atoms into the model, before the next round of least squares. The above sequence is repeated until a complete structural model is obtained without any significant electron density unaccounted for.

1.1.2 Charge-Density Analysis

The IAM approach, though eminently suitable for routine X-ray structure determinations, has a number of shortcomings which stem from the fact that atoms are treated as isolated and neutral species in which the electron density is described by a spherical charge density. Clearly then this model does not take into consideration bonding in any of its varied forms which would manifest itself as an *aspherical* charge distribution around an atom, due to the implicit directionality of chemical bonding.

This has some important consequences including:

- The IAM approximation is better suited to heavier elements in which a significant core density is well described by a spherical density function. Conversely, it is much less suitable for lighter atoms.
- Atoms are constrained to be neutral allowing no possibility for charge transfer. Thus the effects of differing electronegativities on the electron distribution are absent and therefore all atomic electrostatic moments are forced to be zero.
- Asphericity shifts in atomic positions can be observed. E.g. Oxygen atoms displaced towards positions where lone pairs are expected to be [10].

In order to use X-ray diffraction to probe the topological details of the electron distribution, the IAM approximation must be replaced by a more sophisticated model, in which the IAM's limitations are addressed.

The Spherical Atom κ-formalism

One of the first approaches developed was to divide the atomic density into separate contributions from the core and valence shells. This allows the valence shell to be varied independently of the core. To achieve this the κ-formalism (1.16) was developed in which two new parameters have been introduced allowing modification of the valence shell.

$$\rho_{at}(\mathbf{r}) = \rho_{core}(r) + P_v \kappa^3 \rho_{valence}(\kappa r) \tag{1.16}$$

P_v, the valence shell population parameter, facilitates charge transfer between different atoms and results in net atomic charges. In addition, it can be seen that $\rho_{valence}$ depends upon another new parameter κ, which allows for the expansion or contraction of the shell.

The Fourier Transform of (1.16) gives the corresponding κ-formalism atomic scattering factor (1.17), which is used in place of the IAM scattering factors when calculating the model structure factors.

$$f_{j,\kappa}(r^*) = P_{j,c} f_{j,core}(r^*) + P_{j,v} f_{j,valence}(r^*/\kappa) \tag{1.17}$$

Now that charge transfer has been made possible, it is important to ensure that during a refinement there is no overall charge attributed to the unit cell. This necessitates the introduction of an electroneutrality constraint in the least-squares refinement which was not required in IAM refinements.

The κ-formalism, though an improvement on the IAM approximation, still does not allow for a description of aspherical atomic charge distributions. This limitation is addressed by the *Multipole Density Formalism*, which is discussed in the following section.

Multipole Density Formalism

In this formalism the total aspherical atomic density, that is the atomic deformation density resulting from bonding, is described by a summation over a number of aspherical atomic density functions, known as multipoles. These multipoles are

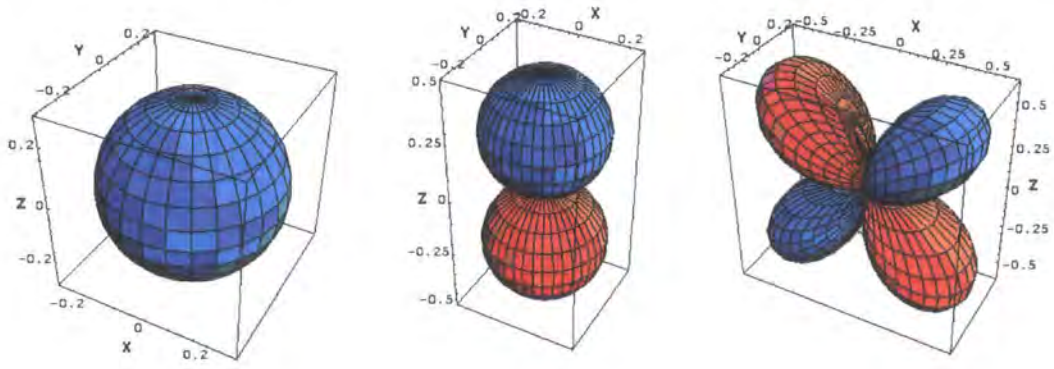

(a) (b) (c)

Figure 1.3: Schematic representations of the real spherical-harmonic functions (a) Monopole [$l = 0$] (b) Dipole [$l = 1$] (c) Quadrupole [$l = 2$]

expressed as a product of a radial function, dependent upon r, and an angular function dependent upon θ and ϕ. The angular functions are typically chosen to be real spherical-harmonic functions, which is a logical choice since these functions are also used for the angular description of atomic orbitals in, for example, Hartree-Fock theory. In the multipole formalism, the normalised real spherical-harmonic functions are denoted by d_{lmp}. The l index determines the type of multipole e.g. monopoles for $l = 0$. Furthermore there are $2l + 1$ unique multipoles of each type, which are specified by the indices m and p such that $-l \leq mp \leq l$ and $p = \pm 1$.

The radial functions are based on Slater-type radial functions given by Clementi [11, 12]. The actual form is based on the one-electron hydrogenic radial functions. These functions, denoted $R_l(\kappa' r)$ are normalised to one electron and have an associated expansion-contraction parameter κ', which behaves in a similar to fashion to the valence shell κ parameter.

In 1969 Stewart [13] introduced a generalised multipole model in which the deformation density was expressed in terms of a finite expansion of nucleus-centered real spherical-harmonic multipoles and subsequently extended to the higher-order multipoles [14]. This was later refined by Hansen and Coppens [15].

$$\rho_{at}(\mathbf{r}) = P_c \rho_{core}(r) + P_v \kappa^3 \rho_{valence}(\kappa r) + \sum_{l=0}^{l_{max}} \kappa'^3 R_l(\kappa' r) \sum_{m=0}^{l} P_{lmp} d_{lmp}(\theta, \phi) \quad (1.18)$$

The Hansen-Coppens multipole formalism (1.18) is an extension of the κ-formalism

and if the expression is in fact truncated after the first two terms, the expression for the κ-formalism is obtained. Therefore Equation 1.17, the expression for the κ-formalism scattering factor, can simply be extended to a total scattering factor by writing in terms of contributions from individual core, valence and aspherical scattering factors (1.19).

$$f_j(\mathbf{h}) = P_{j,c} f_{j,core}(r^*) + P_{j,v} f_{j,valence}(r^*/\kappa) + \sum_{l=0}^{l_{max}} \sum_{m=0}^{l} \sum_{p} P_{lmp} f_{lmp}(\mathbf{h}/\kappa') \quad (1.19)$$

The multipolar contributions $f_{lmp}(\mathbf{h}/\kappa')$, are calculated by a Fourier transform of the aspherical atomic density given by Equation 1.20, where $\langle j_l(r^*/\kappa')\rangle$ are spherical Bessel functions and $d_{lmp}(\beta, \gamma)$ are the transformed spherical-harmonic functions in reciprocal space.

$$f_{lmp}(\mathbf{h}/\kappa') = 4\pi i^l \langle j_l(r^*/\kappa')\rangle d_{lmp}(\beta, \gamma) \quad (1.20)$$

The importance of the κ and κ' parameters can be understood when one considers that these multipole descriptions have only been formulated in terms of nucleus-centered aspherical functions with no consideration of two-center terms, required in quantum mechanics to represent the overlap density. These expansion-contraction κ parameters allow for a good description of the bonding density without the need for inclusion of two-center terms.

The Deformation Density

A convenient way to visualise just the aspherical density features associated with non-bonding and bonding features is the deformation density map. These maps are calculated by taking the difference between the electron density calculated from the multipole model and that of a reference state. The most common choice for the reference state is that of the promolecule, a superposition of atomic densities taken from the IAM approximation (1.21).

$$\delta\rho(\mathbf{r}) = \rho_{mol}(\mathbf{r}) - \sum_j \rho_j(\mathbf{r} - \mathbf{r_j}) \quad (1.21)$$

However great care must be taken in the interpretation of such maps because of the ease of drawing false conclusions from misleading features. These can often be attributed to the following issues:

- Poor scaling applied between the two density states.
- Mis-calculation of the atomic positions in the reference state.
- Inappropriate choice of reference state. The reason why the promolecule may not be best suited to the calculation of deformation densities is summarised succinctly by Coppens: "For atoms with a degenerate ground state, ρ_j is obtained by sharing the valence electrons among orbitals of different angular dependence regardless of their 'ability' to form a bond in the actual arrangement of the atoms" [16].

An alternative scheme for the calculation of deformation densities has been proposed in which the configuration and orientation of the ground state of each constituent atom is determined by a fitting procedure [17].

Charge-Density Analysis of Non-centrosymmetric Systems

Equation 1.12, the expression for the IAM structure factor can also be written in the alternative form, $A + iB$ (1.22).

$$F(hkl) = \sum_{1}^{J} f_j[\cos 2\pi(hx_j + ky_j + lz_j) + i \sin 2\pi(hx_j + ky_j + lz_j)] \qquad (1.22)$$

In centrosymmetric structures, for every atom at position (x, y, z) there is a symmetrically related atom at $(-x, -y, -z)$. It can shown from this observation that (1.22) can be simplified to (1.23).

$$F(hkl) = 2\sum_{1}^{J/2} f_j \cos 2\pi(hx_j + ky_j + lz_j) \qquad (1.23)$$

The phase of a reflection is given by $\tan\alpha = \frac{B}{A}$ and since $B = 0$ then α can only take on the values of 0 or π. This phase restriction does not apply to non-centrosymmetric cases, where α is continuous. The outcome is that accurate charge

density refinements of non-centrosymmetric structures are much more challenging because the problem of determining the phase information is compounded. This is especially important when one considers that the phases have been shown to contain more information about the crystal structure than the measured intensities [18]. There is even evidence to suggest that changes in the populations of odd-order multipoles only results in changes of the structure factor phases and not their magnitudes [19].

Quantum Theory of Atoms in Molecules

Quantum Theory of Atoms in Molecules (QTAIM) relates topological features of the charge density to chemical concepts like chemical bonds and "atoms" as they are found in molecules and provide a means for the calculation of properties of bonds and atoms. QTAIM was developed by Richard Bader and is discussed at length in his book [20].

The electron density ρ is a scalar quantity that varies throughout three-dimensional space. The topology of the electron density can be conveniently described by its gradient vector field, which is obtained by taking the derivative of the density $\nabla\rho$. The gradient vector field describes how the gradient of the electron density (described by a vector) varies over all the points in space. These gradient vectors define gradient paths, which are lines that trace the fastest change in the electron density, perpendicularly crossing the contours in the electron density.

Points in the gradient vector field where $\nabla\rho = \mathbf{0}$ have special significance and define the critical points of the electron density. Each critical point is characterised by three eigenvalues or local intrinsic curvatures λ, which are defined such that $\lambda_1 < \lambda_2 < \lambda_3$. The rank of a critical point r, is equal to the number of non-zero eigenvalues. The signature s is equal to the sum of the signs of the eigenvalues. Together the rank and signature provide a convenient means to classify each critical point. In three dimensions, there are four possible critical points each describing an important feature in the electron density, which are described in Table 1.1.

Thus the presence of a bond critical point between two atoms indicates that an interaction is present between them. Additionally, nuclear attractors are found at

Type	Feature	λ_1	λ_2	λ_3	(r, s)
Maximum	Nuclear Attractor	$-$	$-$	$-$	$(3, -3)$
Saddle Point	Bond Critical Point	$-$	$-$	$+$	$(3, -1)$
Saddle Point	Ring Critical Point	$-$	$+$	$+$	$(3, +1)$
Minimum	Cage Critical Point	$+$	$+$	$+$	$(3, +3)$

Table 1.1: Critical Points of the Electron Density

the positions of every nuclei in the molecule. From the definitions of the critical points we can now classify the different gradient paths observed in $\nabla\rho$. In general, gradient paths trace paths from infinity to the nuclear attractors. A gradient path originating from a bond critical point and finishing at a nuclear attractor defines part of a "bond path", which represents the highest ridge of electron density between two bonded atoms. Another kind of gradient path originates from infinity but terminates at a bond critical point instead of a nuclear attractive. A set of gradient paths of this kind defines an Interatomic Surface (IAS), which defines the boundary between two bonded atoms in the region of space occupied by bonding density. A boundary can also be defined for the open side of atom, that is where the gradient paths extend to infinity from the nuclear attractor. This boundary is typically given by a isosurface of density ~ 0.001au which corresponds approximately to the Van der Waals surface. The combination of the IAS and isosurface completely defines an atomic basin enclosing one nucleus and thus provides a definition of an atom in a molecule in the QTAIM framework.

Determining atomic properties involves integrating the appropriate property density over the atomic basin. Due to the complex shape of the atomic basin any integrations of the atomic basin are non-trivial and also computationally demanding. Examples of atomic properties include the atomic volume, atomic charges and atomic dipole moments. Due to the definition of atoms in the QTAIM framework, all atomic properties are additive and therefore can be used to calculate the corresponding molecular property.

The definition of bonds from QTAIM also provides a means of calculating characteristic bond properties. The bond critical density ρ_b, gives a measure of the

"covalency" of the bond. The ellipticity ε characterises the shape of the electron density in a plane through the bond critical point perpendicular to the bond path and gives a measure of the degree of double bond character. It is calculated from the eigenvalues by $\varepsilon = (\lambda_1/\lambda_2) - 1$. The bonding radius r_b, is the distance between the nucleus and the bond critical point and gives a measure of the size of the atom. Together the bond critical density, ellipticity and bonding radius give a quantitative description of the bonds in molecules.

One of the most important and increasingly popular uses of topological analysis is in the calculation of the curvature of the electron density $\nabla^2\rho$ also known as the Laplacian of the electron density. This shows regions of space where electronic charge is accumulated or depleted. If we define L as the negative of the Laplacian, then where $L > 0$ corresponds to regions of charge accumulation and where $L < 0$ to charge depletion. In the region of space corresponding to the valence shell, maxima in L indicate regions of charge concentration that can be ascribed to either bonding or non-bonding interactions, the latter indicate the presence of lone pairs.

1.1.3 Neutron Diffraction

As was discussed in the last section the fact that X-rays are scattered by the electrons gives us a convenient means to study the charge density. However in neutron diffraction it is not the electrons but the nuclei which act as scatterers. This fact has two important consequences,

1. In X-ray diffraction each chemical element has a different scattering length which is related to its atomic number. Heavy elements have many electrons and as such are easy to 'see' with X-rays. Hydrogen, however, has only one electron and is consequently a poor scatterer of X-rays making it difficult to determine its position accurately. Since hydrogen has no core electrons even a high-resolution X-ray data set is unable to accurately determine its position. In neutron diffraction the scattering length is dependent upon the properties of the nucleus and as such does not vary monotonically as the atomic number increases. Large differences in scattering powers are even seen between isotopes

of the same element. ^{2}H has a scattering length of 6.67fm whereas ^{1}H actually has a *negative* scattering length of -3.74fm [21].

2. Neutron diffraction experiments yield subtly different information about the crystal structure than X-ray diffraction experiments. Typically neutron diffraction studies are favoured in circumstances where very accurate positional and thermal parameters especially for the lighter element like hydrogen, are required. This makes neutron diffraction very popular for performing studies of hydrogen bonding as a complement to X-ray and charge density studies.

The wavelength of neutron radiation is related to the linear momentum, p, by the de Broglie relationship.

$$\lambda = \frac{h}{p} = \frac{h}{mv} \tag{1.24}$$

where m is the mass of the neutron and v is its velocity. Therefore the neutron wavelength is connected to the kinetic energy of the neutron E_k by the following relationship:

$$E_k = \frac{h^2}{2m\lambda^2} \tag{1.25}$$

Also of interest is the fact that unlike X-rays, there is no falloff of intensity with scattering angle because nuclei acting like 'point' scatterers. Consequently neutron diffraction data does not suffer from aspherical effects and as such it is often easier to collect neutron data to high angles than with conventional X-ray studies.

One major disadvantage of neutrons compared with X-rays is the relatively low flux obtainable. Crystals must therefore be larger (typically 1mm^3) in order to avoid data that are too weak. Due to the challenges associated with neutron production with a sufficient flux, neutron diffraction studies can only be currently carried out at central facilities. There are two main ways of producing neutrons for diffraction, spallation sources like ISIS at the Rutherford Appleton Laboratories, and nuclear reactor sources, for example, ILL in Grenoble, France.

Despite the ability to determine the structural parameters for hydrogen accurately, its presence particularly with organic species can have detrimental impact

on the quality of the data obtained from neutron diffraction experiments due to the considerable incoherent scattering of hydrogen. The incoherent scattering lengths, b_{inc}, for hydrogen and deuterium are 25.274 fm and 4.04 fm respectively. The incoherent scatter essentially adds to the background of the diffraction pattern thus compounding the problem of extracting accurate integrated intensities. One method to overcome this problem is achieved by replacing all the hydrogen atoms with deuterium.

This section was only intended to introduce the key concepts involved in diffraction experiments. For a comprehensive and detailed discussion of the theory and practice of X-ray scattering see Giacovazzo et al [22]. Consult Coppens et al [23] for further information on charge densities derived from diffraction experiments and consult Wilson [24] and the Hercules course notes [25] for information regarding neutron single-crystal diffraction.

Chapter 2

Introduction to Quantum-Chemistry Calculations

Quantum-chemistry calculations are increasingly popular and are used extensively in predictive simulations, which aim to calculate accurate properties of new materials, or in modelling experiments, where a model chemistry taken from experiment is used as the basis of a calculation to determine theoretical properties complementary to those taken from the experiment. This chapter covers the theory behind the Hartree-Fock method, applicable to atomic and molecular systems, and how it can be extended to higher periodicities, for example, the solid state. Finally a novel approach called *constrained wavefunction fitting* is introduced, which bridges the gap between quantum-chemistry calculations and scattering experiments, focussing in particular on single-crystal X-ray diffraction.

2.1 Hartree-Fock Theory

The following section discusses the main principles behind Hartree-Fock (HF) theory, laying the necessary groundwork for a discussion in later chapters of perturbation theory and the calculation of polarisabilities and hyperpolarisabilities. While the Hartree-Fock method is applicable to both the open- and closed-shell systems, only the latter case will be considered here. For a more comprehensive treatment of Hartree-Fock theory and other methods of molecular quantum-mechanics calcula-

tions, please consult McWeeny [26] and Atkins [27].

2.1.1 Restricted Hartree-Fock Wavefunction

The fundamental quantity in quantum mechanics is the wavefunction Ψ, which provides a complete description of a system's state. The wavefunction is typically represented by a linear combination of basis functions (2.1), where $\{\Phi\}$ is a set of orthonormal N-particle basis functions, which are dependent on the coordinates and spin states of all N_e electrons in the system.

$$\Psi = \sum_{\mu} \Phi_{\mu} C_{\mu} \tag{2.1}$$

The true wavefunction can only be expressed if a complete N-particle basis is used, which would require a summation of μ to infinity. In practical terms a truncation is required, the simplest being to express the wavefunction as a *single* N-electron basis function. This single-configuration approach is one of the fundamental approximations made in Hartree-Fock theory. One way to represent the N-particle basis is in terms of a product of N one-particle basis functions, also called a Slater determinant[1] (2.2).

$$\Phi_{\mu} = \widehat{A} \prod_{i}^{N_e} \phi_{\mu i}(x_i) \tag{2.2}$$

The antisymmetrisation operator $\widehat{A}$ ensures the Pauli principle is enforced, that is, the total wavefunction is antisymmetric with respect to fermion exchange. In the above equation, each N-particle basis function is expressed as a product of one-electron orbitals $\phi_{\mu i}$, which are dependent on both the position and spin state, x_i, of each electron i. An alternative way of representing these orbitals, is in terms of separate spatial orbitals φ and spin functions (2.3), where the two possible spin states are denoted by α and β, and r_i are the spatial coordinates of electron i.

[1]Hence the Hartree-Fock method is said to have a single determinant wavefunction

$$\begin{aligned} \phi_{\mu i} &= \varphi_{\mu i}(r_i).\alpha_{\mu i} \\ &= \varphi_{\mu i}(r_i).\beta_{\mu i} \end{aligned} \tag{2.3}$$

In a *restricted* wavefunction there are $N_e/2$ spatial orbitals, each doubly occupied with one electron in the α spin state and one electron in the β spin state. Thus restricted wavefunctions are only suitable for descriptions of the ground states of closed-shell systems.

2.1.2 Electronic Energy of the HF Wavefunction

The total Hartree-Fock electronic energy E_{HF}, can be considered to be composed of three separate contributions (2.4), the kinetic energy of the electrons T, the electron-nuclear potential N, and the electron-electron potential V.

$$E_{HF} = T + N + V \tag{2.4}$$

Expressions can be derived for each of these contributions in terms of the spatial orbitals. Thus once these orbitals are known for a particular system, the total electronic energy can be calculated. The kinetic-energy contribution T, is given by Equation (2.5), where ∇^2 is the Laplacian operator.

$$\begin{aligned} T &= 2\sum_{i}^{N_e/2} \int \varphi_i^* - \frac{1}{2}\nabla^2\varphi_i dr \\ &\equiv 2T_{ii} \end{aligned} \tag{2.5}$$

An expression for the potential energy associated with the electron-nuclear interaction is given by Equation (2.6), where Z_I is the number of protons in the nucleus I and $|r_I - r_i|$ is the distance between nucleus I and electron i.

$$\begin{aligned} N &= -2\sum_{I}^{N_n}\sum_{i}^{N_e} \int \frac{\varphi_i^*\varphi_i Z_I}{|r_I - r_i|} dr \\ &\equiv 2N_{ii} \end{aligned} \tag{2.6}$$

This interaction results in a negative contribution to the electronic energy due to the electrostatic attraction between the nuclei and electrons. The electron-nuclear potential term can also be expressed directly in terms of the electron density (2.7).

$$N = -\sum_{I}^{N_n}\sum_{i}^{N_e}\int \frac{\rho(r)Z_I}{|r_I - r_i|}dr \tag{2.7}$$

It is common practice to group the kinetic energy and the electron-nuclear attraction terms together to form a single term representing the core integrals (2.8).

$$h_{ii} = T_{ii} + N_{ii} \tag{2.8}$$

The potential energy resulting from electron-electron repulsion is by definition dependent on the simultaneous positions of two electrons r and r' and is composed of two terms involving bi-electronic integrals (2.9).

$$\begin{aligned} V &= \sum_{i}^{N_e/2}\sum_{j}^{N_e/2} 2\int \varphi_i^*(r)\varphi_i(r)|r-r'|^{-1}\varphi_j(r')\varphi_j^*(r')drdr' \\ &- \sum_{i}^{N_e/2}\sum_{j}^{N_e/2} \int \varphi_i^*(r)\varphi_j(r)|r-r'|^{-1}\varphi_i(r')\varphi_j^*(r')drdr' \\ &\equiv \sum_{i,j} 2(ii|jj) - (ij|ij) \end{aligned} \tag{2.9}$$

The Coulomb term $(ii|jj)$, often denoted by J, accounts for the electrostatic interaction between two electrons. The so-called exchange term $(ij|ij)$, often denoted by K, has no classical interpretation and should be regarded as a quantum-mechanical correction to the Coulomb integral. From Equations (2.8) and (2.9), the total Hartree-Fock electronic energy can be recast[2] in terms of the core, Coulomb and exchange integrals (2.10).

$$E_{HF} = 2h_{ii} + 2(ii|jj) - (ij|ij) \tag{2.10}$$

[2]Summations over i and j implied but not explicitly stated.

2.1.3 Expansion of Orbitals in Terms of a Basis set

Each one-electron spatial orbital φ_i, is typically expanded as a linear combination of one-electron basis functions (2.11).

$$\varphi_i = \sum_a c_{ai}\chi_a \tag{2.11}$$

Where c_{ai} are the unknown coefficients that need to be determined during the calculation. $\{\chi_a\}$ are a set of known basis functions that make up the *basis set*, given as an input to a quantum-chemistry calculation, and which are most commonly expressed as a linear combination of a limited number of Gaussian functions.

The quantum-chemistry calculations in this work make use of a number of basis sets which are listed in Table 2.1 along with the relevant references.

Basis set	Reference	Chapter
D95	Dunning [28]	4
DZP	See Appendix E	4
cc-pVDZ	Dunning [29]	5
6-31G**	Ditchfield et al [30]	7

Table 2.1: Basis sets utilised

2.1.4 Solving the Schrödinger Equation

The Schrödinger equation (2.12), is fundamental to quantum-chemistry calculations, since it relates the wavefunction Ψ, to the total energy of the system E. The total energy operator $\widehat{H}$, is often refered to as the Hamiltonian. This equation belongs to a special class of mathematical problems, known as the *Eigenvalue* problem.

$$\widehat{H}\Psi = E\Psi \tag{2.12}$$

Unfortunately the Schrödinger equation can only be solved analytically for all but the simplest cases. The obstacles involved in solving the Schrödinger equation for more complicated systems are reduced by finding solutions for only the electrons and hence obtaining an *electronic* wavefunction. This is the Born-Oppenheimer

approximation and stems from the fact that the nuclei and electrons have very different masses, which allows the electrons to respond almost instantaneously to any displacement of the nuclei. Within this approximation, the nuclei occupy fixed positions in space. The Schrödinger equation is then solved for the electrons in the static electric potential arising from the fixed nuclei.

The lack of an analytical method for solving the Schrödinger equation means we have to turn instead to variation theory in order to approximate the wavefunction. In this approach, a trial wavefunction $\widetilde{\Psi}$ is constructed, which is optimised by minimising the Raleigh ratio:

$$\widetilde{E} = \frac{\langle \widetilde{\Psi}^* | \widehat{H} | \widetilde{\Psi} \rangle}{\langle \widetilde{\Psi}^* | \widetilde{\Psi} \rangle} \tag{2.13}$$

The variation theorem states that $\widetilde{E} \geq E_0$ is always true. In other words, the energy of the trial wavefunction $\widetilde{E}$ can never be less than E_0, the true ground-state energy. Since the Hartree-Fock wavefunction is expressed in terms of one-electron orbitals, then the energy of the system must therefore be minimised with respect to these orbitals (2.14).

$$\frac{\partial E_{HF}}{\partial \varphi_i} = \frac{\partial E_{HF}}{\partial \varphi_i *} = 0 \tag{2.14}$$

The minimisation procedure must also be subject to a constraint (2.15), which ensures that the wavefunction is normalised, in order to prevent the system from falling into a non-physical state.

$$\int \Psi^* \Psi d\tau = 1 \tag{2.15}$$

In effect, normalising the wavefunction ensures that the probability of finding all the electrons over all of space is one and is equivalent to normalising all the individual orbitals φ_i:

$$\int \varphi_i^* \varphi_i dr = 1 \tag{2.16}$$

The constraint can be applied to (2.14) using the Lagrange method and the resultant condition for optimising the wavefunction is given by (2.17), where ε_i are

the Lagrangian multipliers.

$$\frac{\partial[E_{HF} - \varepsilon_i(\int \varphi_i^* \varphi_i - 1)]}{\partial \varphi_i} = 0 \tag{2.17}$$

In order to derive the Hartree-Fock equations, it is necesssary to expand (2.17) and derive separate conditions for each contribution to the Hartree-Fock Energy. These are given by Equations (2.18), (2.19) and (2.20) for the core, Coulomb and exchange terms respectively, with the normalisation condition given by (2.21).

$$\frac{\partial \sum h_{ii}}{\partial \varphi_k^*} = (T + N)\varphi_k \tag{2.18}$$

$$\begin{aligned} \frac{\partial \sum_{i,j}(ii|jj)}{\partial \varphi_k^*(r'')} &= \sum_k^{N_e/2} \int \varphi_k(r'')|r'' - r'|\varphi_j(r')\varphi_j^*(r')dr' \\ &+ \sum_i^{N_e/2} \int \varphi_i^*(r)\varphi_i(r)|r - r''|\varphi_k(r'')dr \\ &= 2\sum_j \int \varphi_k(r')|r'' - r'|\varphi_j(r')\varphi_j(r')dr' \\ &\equiv J[\varphi_k] \end{aligned} \tag{2.19}$$

$$\begin{aligned} \frac{\partial \sum_{i,j}(ij|ij)}{\partial \varphi_k^*(r'')} &= 2\sum_j \int \varphi_j(r'')|r'' - r'|\varphi_k(r')\varphi_j^*(r')dr' \\ &\equiv K[\varphi_k] \end{aligned} \tag{2.20}$$

$$\frac{\partial \sum_i \varepsilon_i(\int \varphi_i^* \varphi_i dr - 1)}{\partial \varphi_k(r'')} = \varepsilon_k \varphi_k(r'') \tag{2.21}$$

By combining the separate contributions, we arrive at the Hartree-Fock equations (2.22), a set of simultaneous equations from which the Hartree-Fock wavefunction can be obtained as a solution.

$$\underbrace{(T + N)}_{h}\varphi_k + 2J[\varphi_k] - K[\varphi_k] - \varepsilon_k \varphi_k = 0 \tag{2.22}$$

The more familiar form of these equations is achieved by grouping T, N, $J[\varphi_k]$, and $K[\varphi_k]$ together into a single term f:

$$f\varphi_k - \varepsilon_k\varphi_k = 0 \tag{2.23}$$

where f, the Fock operator is given by:

$$f = h + 2J[\varphi_k] - K[\varphi_k] \tag{2.24}$$

It has already been mentioned that each spatial orbital φ_i is expressed in terms of a linear combination of known basis functions χ_a. Making use of this fact, a substitution can be made for the spatial orbitals in (2.23) to derive the Roothan equations (2.25), which are expressed in a compact matrix notation form. Solving these equations, allows us to determine the coefficients of the linear expansion c_{ai} and hence the Hartree-Fock wavefunction.

$$\boldsymbol{Fc} = \boldsymbol{Sc\varepsilon} \tag{2.25}$$

The elements of the Fock matrix $\boldsymbol{F}$, are given by (2.26) and depend on the corresponding Fock operator f.

$$F_{ij} = \int \chi_i^* f \chi_j dr \tag{2.26}$$

$\boldsymbol{S}$ is the overlap matrix, the elements of which are given by (2.27).

$$S_{ij} = \int \chi_i^* \chi_j dr \tag{2.27}$$

The matrix $\boldsymbol{c}$ contains all the coefficients of the linear expansion, which represent the extent that each basis function contributes to the orbitals. The matrix $\boldsymbol{\varepsilon}$ is a diagonal matrix, with the orbital energies ε as elements. In order to determine the Hartree-Fock wavefunction, one must solve the following secular equations:

$$det|\boldsymbol{F} - \boldsymbol{\varepsilon S}| = 0 \tag{2.28}$$

However, these equations cannot be solved directly, because there is the problem of how to calculate the Fock matrix. Looking at the definition of the Fock matrix, one can see that it depends on the Coulomb and exchange integrals, which in turn are dependent on the orbitals. But it is the orbitals themselves that we are trying to

obtain as a solution to the secular equations. It appears that in order to determine the wavefunction, one already has to know it. This issue can be side-stepped by using an iterative scheme called the Self-Consistent-Field (SCF) approach. In this approach, the secular equations are first solved for a trial set of coefficients. The coefficients from the solution are then put back into the secular equations in order to determine a new set of coefficients. This last step is repeated until a convergence criteria is met, usually that the difference in energy between two iterations is less than some desired tolerance.

2.1.5 Interpretation and Analysis of the Wavefunction

Though the wavefunction is a complete mathematical description of a system's state, it does not provide much chemical insight. However, a quantity called the probability density $P(\tau)$ (2.29), which is closely related to the electron density, provides a physical interpretation of the wavefunction in terms of the probability of finding an electron in an infinitesimal volume $d\tau$, at a point τ, in space.

$$P(\tau)d\tau = |\Psi(\tau)|^2 d\tau \tag{2.29}$$

Most importantly the properties of the system can be determined from analysis of the wavefunction. These arise from the expectation values $\langle \widehat{O} \rangle$, which are obtained by application of the corresponding operator $\widehat{O}$ to the wavefunction (2.30).

$$\langle \widehat{O} \rangle = \int \Psi^*(\tau) \widehat{O} \Psi(\tau) d\tau \tag{2.30}$$

Although in principle the operators can be of any mathematical form, only a limited set of operators correspond to observable quantities.

2.1.6 Deficiencies of Hartree-Fock Theory

A major limitation of the Hartree-Fock approach is the absence of electron correlation considerations, which results from representing the wavefunction with only a single Slater determinant. It is known that the spatial and spin coordinates of

two electrons are not independent of one another but are in fact correlated. However in the Hartree-Fock method each electron only experiences an average field of all the other electrons. The difference between the exact energy E_{exact}, and the Hartree-Fock energy E_{HF}, can be attributed to the absence of electron correlation,

$$E_{correlation} = E_{exact} - E_{HF} \tag{2.31}$$

More advanced techniques, for example, Configurational Interaction (CI) and Coupled-Cluster calculations, try to include the effects of electron correlation by an explicit inclusion of more configurational states by using more N-particle basis functions. However the additional complexity of these techniques, results in unfavorable scaling of the time taken to perform these calculations with the size of the system.

A second limitation of the Hartree-Fock method is the introduction of the Basis-set Superposition Error (BSSE). In Equation (2.11), it was shown that the one-electron orbitals are expressed as a linear combination of basis functions. If a complete basis is used, then no error is introduced due to basis-set superposition, but for practical reasons only a limited number of basis functions can be used. The effect of BSSE can be estimated and corrected for, by using a counterpoise correction [31].

2.2 Periodic Hartree-Fock Calculations

The Hartree-Fock equations discussed in Section 2.1 are only suitable for calculations involving atomic and molecular systems, or those based on clusters. In the case of polymeric, slab or crystalline systems, whose defining characteristic is their periodicity, we have to turn to periodic calculations. Conceptually, periodic Hartree-Fock calculations are based on exactly the same approach as used in molecular calculations. That is, a single secular determinant is used to represent the wavefunction, which is dependent on a set of orbital coefficients, which are optimised using the variation principle.

There are a number of issues that come from treating the periodicity and which account for the main differences between periodic and aperiodic Hartree-Fock calculations. These include, the definition of the basis-set, k-space sampling and integral

series trunction,which are addressed in the following sections. Though a number of packages exist for performing periodic quantum-chemistry calculations, the discussion below is limited to the case of Crystal03 [32], a widely available program with which the author is most familiar. For a more in-depth treatment of Hartree-Fock ab-initio calculations on crystalline systems, see reference [33].

2.2.1 Definition of the Basis-set

In molecular systems, the one-electron orbitals, also known as molecular orbitals, are expressed as a linear combination of basis functions, χ_a (Equation 2.11). Typically, these functions are expressed as a linear combination of Gaussian-Type Functions (GTF), which in turn are expressed as a known linear combination of known Gaussian primitives. In the case of 3-dimensional periodic materials, normalised Bloch functions (2.32), are instead used for the basis-functions χ_a and the one-electron orbitals no longer represent molecular orbitals but crystalline orbitals.

$$\chi_{i\mathbf{k}}(\mathbf{r}) = \frac{1}{\sqrt{N}} \sum_{\mathbf{t}} \chi_a^{\mathbf{t}}(\mathbf{r} - \mathbf{r_a} - \mathbf{t}) \exp(i\mathbf{kt}) \tag{2.32}$$

From Equation (2.32), it can be seen that each Bloch function comprises a localised function χ_a, modulated by a phase factor dependent on the wave-vector $\mathbf{k}$, and then summed over all the lattice points in the crystal. Each localised atomic function is located at a position $\mathbf{r_a}$ in the unit cell and related by the lattice translation vector $\mathbf{t}$ to all the translationally-equivalent positions in the crystal.

In an identical way to the basis functions used in molecular calculations, the localised functions are generally expressed as a linear combination of GTFs, denoted G in Equation (2.33), which are in turn expressed in terms of Gaussian primitives.

$$\chi_a(\mathbf{r} - \mathbf{r_a} - \mathbf{t}) = \sum_{j}^{n_G} d_j G(\alpha_j; \mathbf{r} - \mathbf{r_a} - \mathbf{t}) \tag{2.33}$$

Despite the similarity in construction of the localised functions in periodic calculations and the basis functions in molecular calculations, the coefficients of the Gaussian primitives of the latter are in general inappropritate for use in periodic calculations. There are however, a limited number of circumstances in which a

"molecular" basis set is suitable for use in periodic calculations. One such example, is calculations involving molecular crystals, where the basis set is able to provide a suitable description of both the basis functions in molecular calculations and the localised orbitals used to construct the Bloch functions.

2.2.2 k-point Sampling

It is important to realise that the wavevector $\mathbf{k}$, in Equation (2.32) is a continuous variable and consequently would require us to use an infinite number of Bloch functions to describe the wavefunction. In practice, the Schrödinger equation is solved for a finite set of k points and the results interpolated – a procedure known as *k-point sampling.*

The number of k points that should be sampled in order to determine an accurate wavefunction, is related to the size of the first Brillouin Zone (BZ), which in turn is related to the size of the crystallographic unit cell. A large unit cell implies a small first BZ, which requires only a few k points to be sampled. In reality, not all the k points in the first BZ need to be considered, since symmetry considerations can reduce this number considerably.

2.2.3 Integral Series Truncation

It has been shown that in order to evaluate the Coulomb and exchange terms, a number of bi-electronic integral operations must be performed. These are generally the main speed bottlenecks in carrying out quantum-chemistry calculations. In 3-dimensional periodic systems, this problem is compounded because both the Coulomb and exchange terms must be extended to include three separate infinite summations over all direct-lattice vectors. In the case of Crystal03, this is handled by defining a set of five tolerances (two for the exchange series and three for the Coulomb series), which set criteria not only for the truncation of the summations, but also for defining limits beyond which the summations are approximated.

2.3 Experimental Wavefunctions

There is a great interest in the development of methods to obtain "experimental" wavefunctions from experimental data. The motivation for this work is that in doing so all of the experimental data is condensed into a quantity of fundamental significance, from which all of the properties of the system could be calculated, including such quantities as kinetic-energy densities, that are unobtainable from the ground-state electron density alone.

Much of the interest in experimental wavefunctions has focussed on using elastic X-ray scattering data since, as we have already seen, careful X-ray diffraction studies can yield the charge-density distribution. The importance of this might not be apparent until one considers the Hohenberg-Kohn theorem [34], which states that within non-relativistic quantum theory, there is a one-to-one mapping between the ground-state electron density and the wavefunction. An important consequence of this theorem is that it should be possible therefore to calculate all of the ground-state properties from just the ground-state electron density.

Although it is a trivial procedure to obtain the ground-state electron density from the wavefunction, a prescribed approach for obtaining a unique wavefunction from a given electron-density distribution is unfortunately not known. This is called the Hohenberg-Kohn mapping problem. Though the forms of the functionals required to perform the mapping are currently not known, semi-quantitative results have been achieved for kinetic-energy densities [35].

Despite not being able to obtain wavefunctions directly from electron-density distributions, alternative techniques have been developed to obtain experimental wavefunctions consistent with charge densities derived from X-ray diffraction data. One such method, known as constrained wavefunction fitting is discussed in the following section.

2.3.1 Constrained Wavefunction Fitting

Constrained Wavefunction Fitting (CWF) is a general method for obtaining experimental wavefunctions by combining traditional ab-initio quantum calculations

with data obtained from some experiment. One such method, developed by Jayatilaka [36] and implement in the Tonto package [37], uses elastic X-ray scattering data as the constraint on the wavefunction. This approach was initially applied to Be metal [38] and then later applied to a number of molecular crystals, including oxalic acid [39], urea, ammonia and alloxan [40].

The following section discusses this approach in some detail, in particular addressing considerations such as choosing an appropriate starting model or *Ansatz*, quantifying the agreement between the experimental data and the wavefunction and how to fit the wavefunction to the experimental data.

Choose an Appropriate Model Ansatz

Before any fitting can begin, we require an appropriate starting model wavefunction or Ansatz. The obvious choice is to determine the wavefunction of a fragment comprising one formula unit[3] using some ab-initio method like Hartree-Fock.

Agreement Statistic

From the Ansatz, we can evaluate some property of the wavefunction to be used to judge the agreement between the model and experimental data. Since we are concerned with X-ray diffraction data, the obvious choice for the property is set of the X-ray structure factors, $F(\mathbf{h})$. The agreement can then be calculated using a suitable agreement statistic (2.34).

$$\chi^2 = \frac{1}{N_r - N_p} \sum_{\mathbf{h}}^{N_r} \frac{[F_o(\mathbf{h}) - kF_c(\mathbf{h})]^2}{\sigma^2(\mathbf{h})} \tag{2.34}$$

Where N_r is the number of reflections, N_p is the number of parameters in the fitting procedure, $F_o(\mathbf{h})$ are the experimental structure factors with associated estimated standard deviations $\sigma(\mathbf{h})$, $F_c(\mathbf{h})$ are the structure factors calculated from the model and k is a factor required to bring the calculated and experimental structure factors onto the same scale.

[3] In the crystallgraphic sense of the word.

Because the model wavefunction was derived from a fragment only, a method must be found to calculate the electron density of the whole crystal, from which the X-ray structure factors $F_c(\mathbf{h})$, can be obtained. This problem is solved by using a non-interacting fragment model, in which the electron density associated with the unit cell is calculated by summing the electron density of all the symmetry related fragments that make up the unit cell. The structure factors are then simply calculated by a Fourier transform of the unit-cell electron density. An added complication is that a number of systematic effects intrinsic to the experimental data will be absent from structure factors calculated in this way. Consequently, a thermal-smearing correction is also applied to the electron density of the fragment before the structure factors are calculated, in order to account for thermal-motion effects found in the experimental data. In addition, an optional secondary-extinction correction can also be applied to the calculated structure factors to model further real experimental data.

Fitting Procedure

The method of Lagrangian multipliers is employed to constrain the wavefunction to the experimental data:

$$L(\mathbf{c}) = E(\mathbf{c}) - \lambda\chi^2(\mathbf{c}) \tag{2.35}$$

The total energy of the system $E(\mathbf{c})$ is modified by a constraint involving the χ^2 agreement statistic. The Lagrangian multiplier λ, controls how strongly the constraint is applied, that is to what extent the experimental data have influence over the wavefunction. A variational procedure similar to one discussed for the Hartree-Fock method (2.17), is used to minimise $L(\mathbf{c})$, for the orbital coefficients $\mathbf{c}$ (2.36). As λ is increased, the constraint is applied more strongly with the result that χ^2 decreases.

$$\frac{\partial L}{\partial \mathbf{c}} = \frac{\partial E - \lambda\chi^2}{\partial \mathbf{c}} = 0 \tag{2.36}$$

This approach is said to be systematically improvable since the model Ansatz can be replaced by a superior model and the procedure repeated. In practice this

means systematically increasing the λ parameter by small increments and using the resultant wavefunction as the ansatz for the next round of fitting until some desired level of fit has been achieved.

One issue with this approach is identifying the point at which to stop the fitting procedure, since the λ parameter can be in theory increased indefinitely, though in practice convergence problems are observed as the constraint is applied more and more strongly. If the experimental data are of high quality (no systematic errors and realistic estimated standard deviatons), then $\chi^2 = 1$ represents a reasonable level at which to stop fitting. This corresponds to a mean agreement between the model and experimental data of one standard deviation.

Chapter 3

Organic Non-linear Optical Materials: Stucture and Properties

3.1 Introduction

Non-linear Optical (NLO) materials are technologically important with applications in areas such as optical communications, signal processing, and optical data storage [41], which is the direct result of their unique properties, for example second-harmonic generation (SHG) and linear electro-optical effects.

Traditionally inorganic materials like $LiNbO_3$ and $KTiOPO_4$ (KTP) have been used for NLO applications but in recent years focus has turned to organic NLO materials since they have a number of advantages, namely that they are expected to have faster and substantially larger NLO responses and also better damage thresholds. In addition, the molecular nature of these materials lends itself to systematic structural changes of the NLO chromaphore leading to a greater ability to optimise the NLO properties. One drawback of molecular crystals is that they are typically held by together by much weaker forces than inorganic compounds which tends to result in a lack of mechanical stability.

This chapter begins with a definition of the linear and non-linear optical properties, focussing on the microscopic dipole polarisability and hyperpolarisability, along

with a discussion of their relationships to the bulk optical properties, namely the electric susceptibilities and refractive indices. Also presented is one method for the determination of static dipole polarisabilities based on the work of Sylvain and Csizmadia [42] and later improved by Whitten et al [43]. Next follows a discussion of the main crystal-engineering principles behind the design of organic NLO systems and finally, four organic NLO systems are introduced which are the main focus of the work carried out in this thesis.

3.2 Definition of Dipole (Hyper)polarisabilities and Related Bulk Susceptibilities

The introduction of a static electric field F acts as a perturbation on a system, modifying the Hamiltonian $\widehat{H}$, according to (3.1).[1]

$$\widehat{H} = \widehat{H}^0 - \sum_i \widehat{\mu}_i F_i \tag{3.1}$$

Where $\widehat{H}^0$ is the Hamiltonian in the absence of the field and $\widehat{\mu}$ is the dipole moment operator. An equivalent expression in terms of the total energy is given in Equation (3.2).

$$E = E^0 - \sum_i \mu_i F_i \tag{3.2}$$

Where μ_i are the expectation values of the dipole moment operator. By expanding (3.2) as a Taylor series expansion, (3.3) is obtained, which provides a definition for the dipole moment μ^0, the dipole polarisability α and high-order hyperpolarisabilities, for example the first-order hyperpolarisability β.

$$E = E^0 - \mu_i^0 F_i - \frac{1}{2}\alpha_{ij} F_i F_j - \frac{1}{6}\beta_{ijk} F_i F_j F_k + \ldots \tag{3.3}$$

[1] In the following equations the subscripts i, j and k represent any cartesian vector or tensor component. A summation over any one of these subscripts implies a summation over all three cartesian components.

The dipole moment is a measure of the redistribution of the electron density due to the presence of the electric field, whereas the (hyper)polarisabilities are measures of the ease with which the electron density can be redistributed. Alternatively the effect of a static electric field on the total energy of the system can be expressed in term of derivatives of the total energy with respect to the field (3.4).

$$E = E^0 + \sum_i \frac{\partial E}{\partial F_i} F_i + \frac{1}{2} \sum_{i,j} \frac{\partial^2 E}{\partial F_i \partial F_j} F_i F_j + \frac{1}{6} \sum_{i,j,k} \frac{\partial^3 E}{\partial F_i \partial F_j \partial F_k} F_i F_j F_k + \ldots \quad (3.4)$$

By equating corresponding terms in Equations (3.3) and (3.4), expressions can be obtained for the dipole moment, polarisability and higher-order hyperpolarisabilities in terms of energy derivatives with respect to the field:

$$\mu_i = -\frac{\partial E}{\partial F_i} \quad (3.5)$$

$$\alpha_{ij} = -\frac{\partial^2 E}{\partial F_i \partial F_j} \quad (3.6)$$

$$\beta_{ijk} = -\frac{\partial^3 E}{\partial F_i \partial F_j \partial F_k} \quad (3.7)$$

The energy derivatives can be calculated in straightforward manner by the application of perturbation theory, an example of which is given in Section 3.3.1 for the case of approximate static polarisabilities based on the work of Sylvain and Csizmadia [42]. A more detailed discussion is provided in Chapter 4 for the calculation of rigorous polarisabilities and first-order hyperpolarisabilities.

In order to see the link between the microscopic and macroscopic optical properties it is useful to recast (3.3) to give (3.8), an expression for $\Delta\mu$, the dipole moment enhancement due to the electric field in terms of the (hyper)polarisabilities.

$$\Delta\mu_i = \sum_j \alpha_{ij} F_j + \sum_{jk} \beta_{ijk} F_j F_k + \sum_{jkl} \gamma_{ijkl} F_j F_k F_l + \ldots \quad (3.8)$$

The bulk response to an electric field is a polarisation P, which is dependent upon the macroscopic electric susceptibilities $\chi^{(n)}$ and given by Equation (3.9), where ε_0

is the vacuum permittivity. These susceptibilities characterise the linear and non-linear response to the electric field at the macroscopic level in similar way that α, β and γ do at the molecular level.

$$\frac{P_i}{\varepsilon_0} = \sum_j \chi_{ij}^{(1)} F_j + \sum_{jk} \chi_{ijk}^{(2)} F_j F_k + \sum_{jkl} \chi_{ijkl}^{(3)} F_j F_k F_l + \ldots \tag{3.9}$$

The first-order electric susceptibility $\chi^{(1)}$ is related to two other bulk properties, the refractive index n and the relative permittivity ε_r:

$$\chi^{(1)} = n^2 - 1 = \varepsilon_r - 1 \tag{3.10}$$

In optically anisotropic media, the relative permittivity is a third-rank tensor property $\boldsymbol{\varepsilon}$, the principal components of which characterise the optical indicatrix and are in turn related to the refractive indices n_i by (3.11). The relative permittivities and refractive indices both show dispersion, that is, they are dependent upon the wavelength.

$$\varepsilon_i = n_i^2 \tag{3.11}$$

The similar forms of Equations (3.8) and (3.9) suggest a connection between the microscopic (hyper)polarisabilities and the macroscopic susceptibilities (and related refractive indices) and in fact one can be calculated from the other. The relationship between refractive indices and the molecular polarisability for a gas is described by the Lorentz-Lorenz equation [44] (3.12).

$$\frac{n^2 - 1}{n^2 + 2} = \frac{N\bar{\alpha}}{3\varepsilon_0 V} \tag{3.12}$$

where N/V is the number density and ε_0 is the vacuum permittivity. In general the rapid tumbling of molecules in a gas only permits the measurement of an average polarisability $\bar{\alpha}$, defined as:

$$\bar{\alpha} = \frac{1}{3}\{\alpha_{xx} + \alpha_{yy} + \alpha_{zz}\} \tag{3.13}$$

In the case of the solid state, the accurate determination of the electric susceptibilities from the microscopic (hyper)polarisabilities is dependent on a rigorous

treatment of the local field which each molecule in the crystal 'feels'. This treatment is much more complicated than might seem at first because each molecule is not only subject to the external applied electric field, but also the electric fields of neighbouring molecules. Thus a polarisation of a molecule in the system will perturb the electron distribution of its neighbours, changing the local field experienced by that molecule and thus its polarisation must change again accordingly. As such, any rigorous treatment of the local field is non-trivial and is beyond the scope of this discussion but is addressed at length by Rohleder and Munn [45] and also by Whitten et al [43]. The weaker nature of the intermolecular interactions in many molecular crystals often justifies the use of the *oriented-gas* approximation in which interactions between molecules are ignored and consequently the local field is deemed negligible. Bulk properties can then be calculated by a simple additive scheme of the corresponding molecular properties. One such scheme is described in Section 4.4 for the calculation of approximate refractive indices from microscopic polarisabilities.

In the field of optics, we normally consider the case of an oscillating electric field at a frequency ω, since light is an electromagnetic wave. Although it has not been stated, all the linear and non-linear optical properties are themselves dependent on the frequency of the applied electric field. One should be clear that this work only addresses the simpler case of *static* electric fields and as such, all (hyper)polarisabilities are therefore calculated at the zero-frequency limit and should be understood to be *static.*

3.3 Calculation of Dipole Polarisabilities and Hyperpolarisabilities

At first it was thought to be possible to determine (hyper)polarisabilities directly from the one-electron density such as is obtained from a charge-density experiment. Two studies on *N*-(4-nitrophenyl)-(*L*)-prolinol NPP [46,47] and 3-methyl-4-nitroaniline-1-oxide POM [48,49] showed that polarisabilities calculated from charge-density data, when compared to low-level calculations, gave relatively poor agree-

ment. The situation for calculated hyperpolarisabilities was even worse with some elements of the tensor in both compounds differing by more than two orders of magnitude. The poor performance of these (hyper)polarisability calculations can be attributed to the severe approximations made in deriving the expressions for these quantities. It has been highlighted by Whitten et al [43] that the polarisabilities are in fact dependent on 2-electron terms, that is, terms requiring the knowledge of the positions of two electrons simultaneously. Similarly the hyperpolarisabilities are dependent upon three-electron terms. Bearing this in mind, it comes as no surprise that it is not possible to calculate accurate and meaningful (hyper)polarisabilities from charge-density data alone. As a result, we turn our attention now to the electronic wavefunction, since it provides all of the information required to calculate (hyper)polarisabilities. The following section discusses one such method to calculate approximate polarisabilities based on the approximations of Sylvain and Csizmadia [42].

3.3.1 Approximate Polarisabilities (Sylvain and Csizmadia)

Using time-independent, second-order perturbation theory [50] an expression for the sum-over-states (SOS) dipole polarisability can be obtained (3.14).[2]

$$\alpha_{ij} = 2\sum_{n\neq 0} \frac{\langle 0|\widehat{\mu}_i|n\rangle\langle n|\widehat{\mu}_j|0\rangle}{E(n) - E(0)} \tag{3.14}$$

Where $|0\rangle$ is the ground-state wavefunction, $|n\rangle$ is the wavefunction of an excited state and $\widehat{\mu}$ is the dipole moment operator. This rigorous solution can be simplified by replacing the state energy differences $E(n) - E(0)$ by orbital energy differences $(\varepsilon_i - \varepsilon_j)$, which are less computationally demanding to calculate and which results in an expression equivalent to that of uncoupled perturbation theory. A further approximation was introduced by Huiszoon [51] and is discussed in more detail by Sylvain and Csizmadia [42] in which the Unsöld approximation [52] was applied, replacing these excitation energies by some mean energy Δ (3.15).

[2]See Section 4.2 for a more detailed discussion of perturbation theory and Section 4.3.2 for more information on the SOS approximation.

$$\alpha_{ij} = \frac{2}{\Delta} \sum_{n \neq 0} \langle 0|\widehat{\mu}_i|n\rangle\langle n|\widehat{\mu}_j|0\rangle \tag{3.15}$$

This expression still requires a sum over all the excited states which is tedious to calculate, but the introduction of Δ and an application of the closure approximation, allows the reduction of (3.15) to (3.16), which now only includes terms involving the ground state but still clearly depends on both one- and two-electron expectation values.

$$\alpha_{ij} = \frac{2}{\Delta}\left\{ \langle 0|\widehat{\mu}_i\widehat{\mu}_j|0\rangle - \langle 0|\widehat{\mu}_i|0\rangle\langle 0|\widehat{\mu}_j|0\rangle \right\} \tag{3.16}$$

Expressing (3.16) in terms of an atomic basis results in Equation (3.17), as implemented in the Tonto package.

$$\alpha_{ij} = \frac{4}{\Delta}\left\{ Tr\{\mathbf{PQ_{ij}}\} - Tr\{\mathbf{PD_iPD_j}\} \right\} \tag{3.17}$$

P is the half-closed density matrix and **D** and **Q** are the dipole and quadrupole moment integral matrices respectively. The calculation of the polarisability is now trivial except the value for the unknown Δ term must be determined by some means. Sylvain and Csizmadia assumed a certain functional form for Δ and fitted a series of calculations based on a modest 4-31G basis-set to experimental values for a series of molecules to determine an expression for Δ, (3.18).

$$\frac{1}{\Delta} = -\frac{1}{N_{occ}} \sum_{n=1}^{N_{occ}} \frac{1}{\varepsilon_k} \tag{3.18}$$

Where N_{occ} is the number of doubly occupied molecular orbitals and ε_k is the energy of the occupied orbital k. A major drawback to this approach is that both core and valence terms are given equal weighting to the polarisability which is counter-intuitive since one would expect the valence orbitals to have the largest contribution. Spackman et al [43] improved (3.18) by breaking the polarisability into separate orbital contributions (3.19), with the aim of weighting each contribution by the inverse of the energy of that orbital (3.20).

$$\alpha_{ij} = \sum_{p} \left\{ \alpha_{ij}^{p} + \sum_{q<p} \alpha_{ij}^{pq} \right\} \tag{3.19}$$

However it can be seen from (3.19) that the polarisability cannot be broken down into just single orbital contributions, since it also depends on cross terms α_{ij}^{pq}, which have to be weighted differently (3.21).

$$\alpha_{ij}^{p} = \frac{4}{\varepsilon_p}\Big\{ Tr\{\mathbf{P}^p\mathbf{Q}_{ij}\} - Tr\{\mathbf{P}^p\mathbf{D}_i\mathbf{P}^p\mathbf{D}_j\} \Big\} \tag{3.20}$$

$$\alpha_{ij}^{pq} = -2\left\{\frac{1}{\varepsilon_p} + \frac{1}{\varepsilon_q}\right\}\Big\{ Tr\{\mathbf{P}^p\mathbf{D}_i\mathbf{P}^q\mathbf{D}_j\} + Tr\{\mathbf{P}^q\mathbf{D}_i\mathbf{P}^p\mathbf{D}_j\} \Big\} \tag{3.21}$$

From equations (3.19), (3.20) and (3.21) approximate polarisabilities can be calculated based on the scheme of Sylvain and Csizmadia and also with the improved means of calculating the Δ parameters based on the scheme of Whitten et al.

However this approach does not lead to the calculation of accurate polarisabilities. For Sylvain and Csizmadia this was solved by application of empirical correction factors based on experimental polarisabilities measured at a range of wavelengths. Spackman et al [43] avoided the use of this inconsistent reference and instead devised a scheme to obtain approximate pseudo-CPHF polarisabilities, by using a scale factor dependent upon the CPHF and Sylvain-Csizmadia polarisabilities, obtained from ab-initio unfitted calculations:

$$\widetilde{\alpha}_{CPHF}^{f} = \alpha_{SC}^{f} \times \frac{\alpha_{CPHF}^{u}}{\alpha_{SC}^{u}} \tag{3.22}$$

where the superscript 'f' denotes a wavefunction fitted value and 'u' an ab-initio unfitted value and where the subscript 'SC' denotes a Sylvain-Csizmadia polarisability and 'CPHF' the corresponding CPHF value. In principle this approach could be used to scale the whole polarisability tensor, but in practice separate scalings were performed on each of the principle components and the mean polarisability. The unfitted CPHF results were calculated at the MP2/DZP+ level of theory. This approach has been refered to as a boot-strapping procedure and is the biggest drawback of this approach.

3.4 Organic Molecular Crystals as NLO Prototypes

In designing materials for NLO applications, the aim is to maximise the NLO response, that is to create materials with large microscopic (hyper)polarisabilities and correspondingly large bulk susceptibilities. In order for a material to have realisable NLO properties, it must crystallise in a non-centrosymmetric space group, which prevents the even-order bulk susceptibilites from vanishing. Furthermore the molecule itself should also be acentric.

Unfortunately the definitions of the (hyper)polarisabilities obtained from quantum mechanical considerations, gives little insight into requirements needed for the successful engineering of new NLO materials other than the symmetry restrictions already mentioned.

Work in this field however has revealed certain structural features that are particularly important for obtaining large first-order hyperpolarisabilities [41]. Materials based on highly conjugated π-systems are favoured since the π-electrons are much more mobile and polarisable than electrons involved in σ bonds. The π-systems are typically based on benzene and pyridine units though larger, more extended π-systems based on stilbenes are also observed [24].

In addition to the π-system, organic NLO materials also contain strong electron donor and acceptor groups, positioned at opposite ends of the molecule which help in creating and enhancing a charge asymmetry. Typical donor groups include (substituted) amines, while nitro and nitrile groups are commonly used acceptor groups.

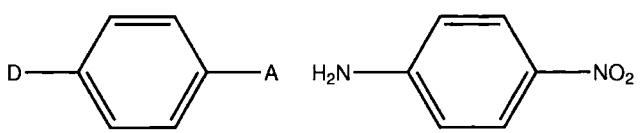

(a) (b)

Figure 3.1: Schematics of (a) prototypical organic NLO system (b) para-Nitroaniline (pNA)

Figure (3.1) shows a schematic representation of a prototypical organic NLO

material with an acceptor group A and a donor group D, along with the canonical organic NLO material para-nitroaniline (pNA). Unfortunately the introduction of strong electron donating and accepting groups, particularly in a para arrangement, to create a strongly dipolar molecule, often encourages crystallisation in a centrosymmetric head-to-tail arrangement. This problem can often be solved by the introduction of one or more substituents which enforces a different packing arrangement of the molecules. In the case of pNA, which is centrosymmetric, the addition of a methyl group to give 2-methyl-4-nitroaniline (MNA) results in an acentric structure.

3.5 Compounds of Interest

This study focuses on four organic molecular crystals selected from the literature, due to their importance in the field of non-linear optics, namely 4-(*N*,*N*-dimethylamino)-3-acetamidonitrobenzene (DAN) [13], 2-(*N*-L-prolinol)-5-nitropyridine (PNP) [15], (S)-2-(α-methylbenzylamino)-5-nitropyridine (MBANP) [14] and *N*,*N*-dimethyl-4-nitroaniline (NNDPNA) [16,17]. Even though these materials have been known for some time and in general their experimental optical properties have been well established, to our knowledge no charge-density studies have been performed on any of these systems. This fact motivated the collection of high resolution X-ray diffraction datasets, to be used for charge-density analysis and constrained wavefunction calculations. In the case of DAN, MBANP and PNP, the data collection, data reduction and multipole refinements were performed by Dr D.S. Yufit at the University of Durham. Each compound has a significant second-harmonic generation activity as evidenced by their powder SHG activity relative to urea (Table 3.1).

Figure 3.2 shows the chemical structures of DAN, MBANP, PNP and NNDPNA, which are all based on the NLO prototype material, pNA. All the materials make use of a nitro acceptor group, which is the most common one found in organic NLO materials. More variety is seen however in the choice of donor group. In the case of DAN and NNDPNA the basic aniline group has been replaced by a *N*,*N*-dimethyl

	Effic. × Urea
DAN	115
PNP	140
MBANP	25
NNDPNA	-

Table 3.1: Efficiency of Powder SHG activity relative to Urea.

substituted aniline, since it is a better electron donor. The donor group has also been used as a source of chirality for the molecules PNP and MBANP, which is used to ensure that these materials crystallise in a non-centrosymmetric spacegroup. In addition the bulky nature of the donor group in MBANP also has a strong influence over the packing of the molecules in the crystal, as does the amide side-chain in DAN.

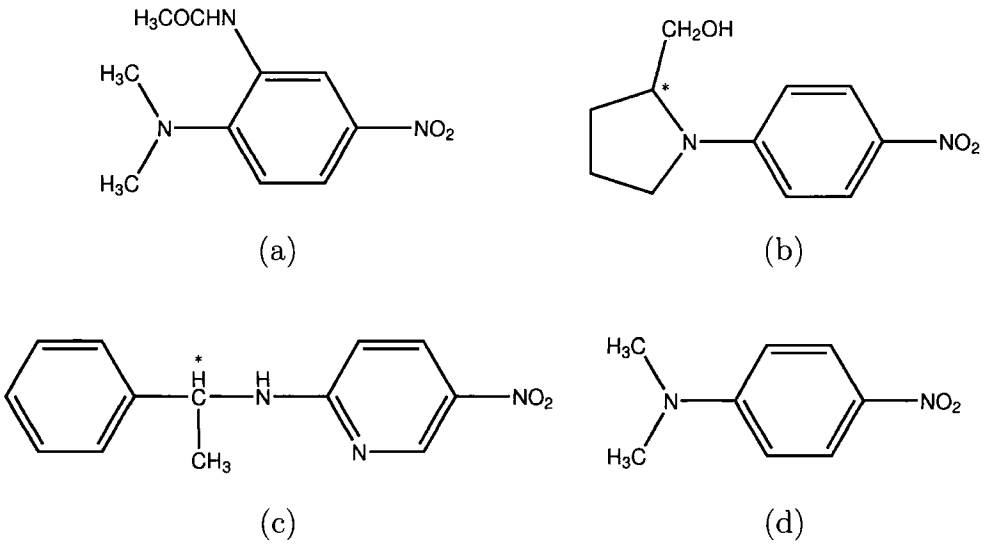

Figure 3.2: Schematics of (a) DAN (b) PNP (c) MBANP and (d) NNDPNA

3.6 Outline of the Work

Chapter 4 presents the first examples of using constrained-wavefunction calculations of X-ray diffraction data to obtain CPHF polarisabilities. Experimental wavefunctions were determined on three model compounds, benzene, urea and 2-methyl-

4-nitroaniline with dipole polarisabilities and refractive indices compared with a previous study by Whitten et al. [43] in which these quantities were determined from the less rigorous scheme of Sylvain and Csizmadia [42] using their own scaling method to obtain pseudo CPHF polarisabilities and the related refractive indices.

In Chapter 5 constrained wavefunction calculations are performed on DAN, MBANP and PNP using charge-density data collected by Dr D.S. Yufit, and employing the constrained wavefunction scheme discussed in detail in Section 2.3.1. The quality of the fitting calculations is discussed, in addition to reporting CPHF polarisabilities, CPHF hyperpolarisabilities and refractive indices for each of the three compounds.

Chapter 6 provides a detailed comparison of the constrained wavefunction calculations and multipole refinements of the materials, DAN, MBANP and PNP, looking at a range of properties including electrostatic moments, deformation densities and negative Laplacians, in order to understand better the nature of the 'experimental' wavefunctions obtained using the constrained wavefunction approach.

In Chapter 7 the non-linear optical prototype NNDPNA is studied using a multipole refinement of high-resolution single-crystal X-ray diffraction data, from which various properties of the charge density are reported.

The final chapter provides an overall summary of the work presented and indications of the direction of possible future work.

In Appendix A, an attempt has been made to estimate the errors of the linear and non-linear optical properties calculated by the wavefunction-fitting procedure. Percentage errors have been calculated for the dipole polarisability, hyperpolarisability and refractive indices of MNA by means of wavefunction-fitting calculation using a random-error data set. In Appendix B, a thorough look at the intermolecular interactions of DAN, MBANP, PNP and NNDPNA is made, using Hirshfeld surfaces and fingerprint plots, which are a novel way of summarising all the intermolecular interactions present in molecular crystals. Appendix C details the neutron structure determination of NNDPNA at 100K on the hot-source four-circle instrument D9 at the Institut Laue-Langevin in Grenoble, France. Appendix D describes a number of programming tools which were written during the course of this Ph.D. Appendix

E details a DZP basis-set which was used extensively during this research project. And finally, Appendix F describes the synthesis of two further known NLO materials, AANP and COANP, along with the characterisation of the former material.

Chapter 4

Solid-state Linear and Non-linear Optical Properties

4.1 Introduction

In order to understand fully the structure-property relationship of NLO materials and aid us in the design of new and better materials for NLO applications, we must be able to determine consistently accurate non-linear optical properties. Although not directly relevant to NLO behaviour, there is a clear link between the linear and non-linear properties. Evidently if we are unable to obtain accurate values for the linear properties there seems little point in looking beyond to the non-linear ones; hence this chapter also addresses the calculation of the linear optical properties.

The calculation of dipole (hyper)polarisabilities of isolated molecules is well developed but the calculation of the in-crystal dipole (hyper)polarisabilities and the related macroscopic susceptibilities i.e. the bulk properties of molecular crystals, is not so advanced.

As was discussed in Section 3.3, it is impossible to obtain accurate (hyper)polarisabilities from charge-density data alone because the detail of the electron correlation is lost. Despite this, there is a continued interest in trying to obtain microscopic (hyper)polarisabilities with the help of charge-density data especially considering that the resultant quantities will include the effects of intermolecular interactions, which are of course absent from isolated molecule calculations. An alternative approach

is the so-called constrained wavefunction fitting method (Section 2.3.1) in which an experimental wavefunction is obtained that is consistent with the X-ray diffraction data. Consequently access to the wavefunction permits access to two-electron terms which should permit the determination of accurate (hyper)polarisabilities.

This work is an extension of the work carried out by Dr A.E. Whitten at UNE [53] in collaboration with Prof. M. A. Spackman (UNE) and Assoc. Prof. Dylan Jayatilaka (UWA). Whitten calculated approximate dipole polarisabilities and related refractive indices for benzene, urea and 2-methyl-4-nitroaniline (MNA), using the Sylvain-Csizmadia [42] approach discussed in Section 3.3.1 from experimental wavefunctions obtained from constrained wavefunction fitting calculations performed using the Tonto program [37].

This work goes beyond that by calculating exact Coupled Perturbed Hartree-Fock (CPHF) dipole polarisabilities based on my implementation in the Tonto package of the Equations (4.28),(4.34) and (4.35), as discussed in Section 4.3.2. The advantage of this approach, is that the dipole polarisabilities no longer depend on a calibration procedure required to determine the unknown Unsöld parameter, Δ (See Eq. 3.15). In addition, Equations (4.40) and (4.9) have also been implemented which allows the calculation of the hyperpolarisabilities, which are particularly important for our understanding of NLO materials.

This chapter presents the basic theory behind CPHF theory and then addresses the equations for *static* dipole polarisabilities and hyperpolarisibilities. These quantities are calculated for benzene, urea and MNA for both SCF and constrained wavefunction fitting. The SCF results were compared with the Gaussian program as check against errors in implementation. The results from the constrained wavefunction calculations were compared with the experimental results and those of the previous study by Whitten et al [43].

In addition, the relationship between dipole polarisabilites and refractive indices is discussed and equations for calculating refractive indices were implemented in Tonto according to the scheme of Rohleder and Munn [45]. Refractive indices were calculated for each of the three compounds and again compared with experimental refractive indices and those obtained from Whitten's calculations.

4.2 Coupled Perturbed Hartree-Fock Theory

Coupled Perturbed Hartree-Fock (CPHF) theory is an application of time independant perturbation theory, in which the Hartree-Fock equations are modified to account for the effects of one or more perturbations on a system. Examples of perturbations include, the displacement of nuclei, an applied magnetic field or an applied electric field. In other words, the Hartree-Fock energy is a function not only of the orbitals, but also of some perturbation λ, μ, ν etc. (4.1).

$$E_{HF} = E_{HF}[\{\phi_p\}, \lambda, \mu, \nu \ldots] \tag{4.1}$$

4.2.1 Derivatives of the Molecular Orbitals

To understand how the energy of a perturbed system changes, it is necessary to understand how the molecular orbitals ϕ_p vary with the perturbation, which in turn requires a knowledge of the first derivatives with respect to that perturbation.

$$\varphi_p = \sum_\alpha c_{\alpha p}\chi_\alpha \tag{4.2}$$

If the Hartree-Fock orbitals are given by a linear combination of atomic orbitals (4.2), the derivative with respect to the perturbation λ is given by (4.3).

$$\frac{\partial \varphi_p}{\partial \lambda} = \sum_\alpha \left\{ \frac{\partial c_{\alpha p}}{\partial \lambda}\chi_\alpha + c_{\alpha p}\frac{\partial \chi_\alpha}{\partial \lambda} \right\} \tag{4.3}$$

In some situations, the last term of (4.3) vanishes because the basis functions $\{\chi_\alpha\}$ do not depend on the perturbation i.e. the derivative with respect to the perturbation is zero. This is true in the case of an applied electric field F_λ:

$$\frac{\partial \varphi_p}{\partial F_\lambda} = \sum_\alpha \frac{\partial c_{\alpha p}}{\partial F_\lambda}\chi_\alpha \tag{4.4}$$

The introduction of $\boldsymbol{U}^\lambda$ matrices greatly simplifies the CPHF equations, since they contain all of the information on the derivatives of the orbital coefficients (4.5). In effect, calculation of the $\boldsymbol{U}^\lambda$ matrices is equivalent to finding the derivatives of all the orbitals with respect to the perturbation.

$$\frac{\partial c_{\alpha p}}{\partial \lambda} = \sum_p c_{\alpha q} U_{qp}^{\lambda} \tag{4.5}$$

It is also useful to define the second derivatives of the molecular orbitals, $\boldsymbol{U}^{\lambda\mu}$, for later use:

$$\frac{\partial^2 c_{\alpha p}}{\partial \lambda \partial \mu} = \sum_p c_{\alpha q} U_{qp}^{\lambda\mu} \tag{4.6}$$

Because the orbitals are required to be orthogonal, this has implications for both $\boldsymbol{U}^{\lambda}$ and $\boldsymbol{U}^{\lambda\mu}$. Starting at the orbital orthogonality condition, $\langle \phi_p | \phi_q \rangle = \delta_{pq}$, the following expression for the first-order orthogonality relation can be derived (4.7).

$$U_{qp}^{\lambda} + U_{pq}^{\lambda} = 0 \tag{4.7}$$

This relation therefore implies that $\boldsymbol{U}^{\lambda}$ is antisymmetric. By differentiating the first-order orthogonality relation we obtain an expression for the second-order orthogonality relation (4.8),

$$\begin{aligned} U_{qp}^{\lambda\mu} + U_{pq}^{\lambda\mu} + U_{pr}^{\lambda} U_{qr}^{\mu} + U_{pr}^{\mu} U_{qr}^{\lambda} &= 0 \\ U_{qp}^{\lambda\mu} + U_{pq}^{\lambda\mu} + \xi_{pq}^{\lambda\mu} &= 0 \end{aligned} \tag{4.8}$$

where $\xi_{pq}^{\lambda\mu}$ is symmetric in both the super and subscript sets of indices and is defined in (4.9).

$$\xi_{pq}^{\lambda\mu} = U_{pr}^{\lambda} U_{qr}^{\mu} + U_{pr}^{\mu} U_{qr}^{\lambda} \tag{4.9}$$

Extensive use of these two orthogonality relations is made in simplifying the expressions for CPHF (hyper)polarisabilities derived from the CPHF equations.

4.2.2 Hartree-Fock Energy (Electric-Field Case)

The exact form of the expression for the Hartree-Fock energy depends on the type of perturbation being considered. We now turn our attention to the case of an applied electric field, since we are interested in obtaining analytical expressions

for polarisability and hyperpolarisability, which characterise a system's response to the field. Only time-independent perturbation theory has been considered, which means the following equations can only describe the effects of *static* electric fields on a system. The Hartree-Fock energy in the presence of an electric field F_k is given by (4.10)[1].

$$E = 2h_{ii} + 2(ii|jj) - (ij|ij) - 2(i|\hat{\mu}^k F_k|i) \tag{4.10}$$

Comparing this with the standard Hartree-Fock equation (2.10), we can see that the presence of an electric field introduces a new term that depends on the expectation value of the dipole-moment operator $\hat{\mu}$ for a field F, applied in the direction k. Solutions of the Hartree-Fock method are found using the variation principle, which requires finding a set of orbitals that minimises the energy with respect to the perturbation. Therefore this imposes the condition that the derivative of the energy E with respect to λ must be zero, where the parameter λ represents $c_{\mu p}$ (4.11).

$$E^{\lambda} = 4U^{\lambda}_{pi}\Big[h_{pi} + 2(pi|jj) - (pj|ij) - (p|\hat{\mu}^k F_k|i)\Big] = 0 \tag{4.11}$$

Equation (4.11) involves a summation over all molecular orbitals p, which can be split into two separate summations, firstly over occupied orbitals j and secondly over the virtual orbitals a. This reduces the derivative to a summation over only the virtual orbitals (4.12) because the second summation over the occupied orbitals vanishes as a consequence of having a contraction between an antisymmetric term (the $\boldsymbol{U}^{\lambda}$ matrix) and a symmetric term (the term in square brackets only involving occupied orbitals).

$$E^{\lambda} = 2U^{\lambda}_{ai}\Big[h_{ai} + 2(ai|jj) - (aj|ij) - (a|\hat{\mu}^k F_k|i)\Big] = 0 \tag{4.12}$$

Since the U^{λ}_{ai} terms are not necessarily zero, then by definition (4.13) must be true. We now have an expression for the Hartree-Fock condition in terms of the

[1]The indices i, j and k are reserved for occupied orbitals, a, b and c for unoccupied or virtual orbitals and p, q and r for any or all orbitals.

virtual-occupied block of the Fock matrix f_{ai}, i.e. the criteria for finding a solution to the Hartree-Fock equations in the presence of an electric field.

$$f_{ai} \equiv h_{ai} + 2(ai|jj) - (aj|ij) - (a|\hat{\mu}^k F_k|i) = 0 \tag{4.13}$$

However we need some way to determine the orbital derivative matrices $\boldsymbol{U}^\lambda$ and $\boldsymbol{U}^{\mu\nu}$. In the next section we turn to Coupled Perturbed Hartree-Fock theory from which we derive the CPHF equations, which are concerned with the determination of these quantities.

4.2.3 First-order CPHF Equations for Electric Fields

By differentiating the Hartree-Fock condition and evaluating the result at zero field strength, an expression for the first-order CPHF equation is obtained (4.14),

$$\frac{\partial f_{ai}}{\partial F_\lambda} = U^\lambda_{pa} f_{pi} + U^\lambda_{pi} f_{ap} + A_{ai,pj} U^\lambda_{pj} - (a|\hat{\mu}^\lambda|i) = 0 \tag{4.14}$$

where $A_{ai,pj}$ is given by:

$$A_{ai,pj} = 4(ai|pj) - (ap|ij) - (aj|ip) \tag{4.15}$$

This equation can be simplified to give (4.16), when we consider that at convergence the diagonal elements of the Fock matrix are the orbital eigenvalues ε_p and all off-diagonal elements are zero.

$$\frac{\partial f_{ai}}{\partial F_\lambda} = U^\lambda_{ia} \varepsilon_i + U^\lambda_{ai} \varepsilon_a + A_{ai,pj} U^\lambda_{pj} - \mu^\lambda_{ai} = 0 \tag{4.16}$$

As before, the summation over all orbitals p, can be split into a summation over the occupied set of orbitals and one over the virtual set of orbitals. Only the summation over the virtual orbitals is non-zero and by application of the antisymmetry of $\boldsymbol{U}^\lambda$, we obtain the first-order CPHF equations in their final form:

$$(\varepsilon_a - \varepsilon_i) U^\lambda_{ai} + A_{ai,bj} U^\lambda_{bj} = \mu^\lambda_{ai} \tag{4.17}$$

The CPHF equations represent a set of linear equations, which are defined by the matrix elements $H_{ai,bj}$, given in (4.18).

$$H_{ai,bj} = \delta_{ab}\delta_{ij}(\varepsilon_a - \varepsilon_i) + A_{ai,bj} \tag{4.18}$$

The first-order CPHF equations only determine the virtual-occupied block of $\boldsymbol{U}^\lambda$ and as a result the occupied-occupied and virtual-virtual blocks are ill-determined. A similar set of CPHF equations (4.19) can be obtained by making use of an alternative Hartree-Fock condition based on "canonical" Hartree-Fock orbitals i.e. $f_{pq} = 0$ for $p \neq q$. An important consequence of these equations is that all of the elements of $\boldsymbol{U}^\lambda$ are determined from just the virtual-occupied block.

$$(\varepsilon_p - \varepsilon_q)U^\lambda_{pq} + A_{pq,bj}U^\lambda_{bj} = \mu^\lambda_{pq} \tag{4.19}$$

4.2.4 Second-order CPHF Equations for Electric Fields

The second-order CPHF equations can be derived by differentiating the Hartree-Fock condition twice to give:

$$\begin{aligned}
\frac{\partial^2 f_{ai}}{\partial\mu\partial\nu} &= H_{ai,bj}U^{\mu\nu}_{bj} - \frac{1}{2}A_{ai,kj}\xi^{\mu\nu}_{kj} \\
&+ U^\mu_{pa}U^\nu_{qi}f_{pq} + U^\mu_{pi}U^\nu_{qa}f_{qp} \\
&+ U^\mu_{pa}A_{pi,qj}U^\nu_{qj} + U^\mu_{pi}A_{ap,qj}U^\nu_{qj} + U^\nu_{pa}A_{pi,qj}U^\mu_{qj} + U^\nu_{pi}A_{ap,qj}U^\mu_{qj} \\
&+ A_{ai,pq}U^\mu_{pj}U^\nu_{qj} \\
&- U^\nu_{pa}\mu^\mu_{pi} - U^\nu_{pi}\mu^\mu_{ap} - U^\mu_{pa}\mu^\nu_{pi} - U^\mu_{pi}\mu^\nu_{ap} = 0
\end{aligned} \tag{4.20}$$

By expanding the terms involving summations over all orbitals p, and using the orthogonality of $\boldsymbol{U}^\lambda$ to cancel terms, it can be shown that the second-order CPHF equations can be reduced to:

$$\begin{aligned}
H_{ai,bj}U^{\mu\nu}_{bj} &= \frac{1}{2}A_{ai,kj}\xi^{\mu\nu}_{kj} - \frac{1}{2}A_{ai,bc}\xi^{\mu\nu}_{bc} \\
&- U^\mu_{ka}f^\nu_{ki} - U^\nu_{ka}f^\mu_{ki} - U^\mu_{bi}f^\nu_{ab} - U^\nu_{bi}f^\mu_{ab}
\end{aligned} \tag{4.21}$$

where f^ν_{pq} is defined as:

$$f^\nu_{pq} = -\mu^\nu_{pq} + A_{pq,bj}U^\nu_{bj} \tag{4.22}$$

4.3 Analytical Derivatives of the Hartree-Fock Energy

In Section 3.2 it was shown that the definitions of the dipole moment, polarisability and first-order hyperpolarisability were related to the derivatives of the Hartre-Fock energy with respect to a component of the electric field. The exact forms of these derivatives depends on the molecular orbitals, obtained by finding orbitals that satisfy the Hartree-Fock condition, and also on derivatives of the molecular orbitals, obtained from the first- and second-order CPHF equations. The following sections derive analytical expressions for the dipole moment, the sum-over-states polarisability, the CPHF polarisability and the CPHF hyperpolarisability. It is important to realise that since the Hartree-Fock energy is an approximation to the true energy, these quantities are also approximations to the true values.

4.3.1 Dipole Moment

The derivative of the Hartree-Fock energy with respect to the electric field F_λ is trivially given by:

$$\frac{\partial E}{\partial F_\lambda} = -2(i|\hat{\mu}^\lambda|i) = -2\mu_{ii}^\lambda \tag{4.23}$$

By equating (4.23) with the definition of the dipole moment (3.5), the following expression is obtained for the dipole moment.

$$\mu_\lambda = 2\mu_{ii}^\lambda \tag{4.24}$$

Unsurprisingly, the dipole moment is simply given by the expectation value of the dipole-moment operator $\hat{\mu}^\lambda$.

4.3.2 CPHF Polarisability

In Section 3.2, it was also shown that the polarisability $\boldsymbol{\alpha}$ depends on the second derivative of the Hartree-Fock energy (4.25), from which the expression for the CPHF polarisability is obtained (4.26).

$$\frac{\partial^2 E}{\partial F_\lambda \partial F_\mu} = -4U_{pi}^{\mu}\mu_{pi}^{\lambda} \tag{4.25}$$

$$\alpha_{\lambda\mu} = 4U_{pi}^{\mu}\mu_{pi}^{\lambda} \tag{4.26}$$

The implied summation over all orbitals p, can be decomposed once again into separate contributions from the occupied and virtual orbitals to give (4.27).

$$\alpha_{\lambda\mu} = 4U_{ai}^{\mu}\mu_{ai}^{\lambda} + 4U_{ji}^{\mu}\mu_{ji}^{\lambda} \tag{4.27}$$

The second term involving only occupied-occupied terms is equal to zero because μ_{ji}^{λ} is symmetric and U_{ji}^{μ} is antisymmetric. Thus, the final expression for the CPHF polarisability is given by (4.28).

$$\alpha_{\lambda\mu} = 4U_{ai}^{\mu}\mu_{ai}^{\lambda} \tag{4.28}$$

The polarisability is comprised of terms involving transitions between occupied and virtual orbitals. One extra piece of information that can ascertained from (4.28), is which of these transitions have the largest contributions to the polarisability. By breaking down the polarisability, or more correctly the mean polarisability, into different contributions for each pair of molecular orbitals involved in the transition, it is possible to see which of the orbital pairs have the greatest contribution to the molecular polarisability. The mean polarisability $\overline{\alpha}$ is defined as:

$$\overline{\alpha} = \frac{1}{3}\alpha_{\lambda\lambda} \tag{4.29}$$

from which the contribution to the mean polarisability by orbitals a and i is given by (4.30). The largest values of the $\overline{\boldsymbol{\alpha}}$ matrix thus correspond to the largest and therefore the most important contributions.

$$\overline{\alpha}_{ai} = \frac{1}{3}\sum_{\lambda} F_{ai}^{\lambda}U_{ai}^{\lambda} \tag{4.30}$$

In order to be able to calculate the CPHF polarisability given by Equation (4.28), we have to be able to determine the derivatives of the molecular-orbital coefficients

$\boldsymbol{U}^\lambda$. The use of the CPHF equations to achieve this, is addressed in the following sections, which discuss not only rigorous CPHF polarisabilities but also the sum-over-states approximation, which avoids the need to calculate the orbital derivatives entirely.

Sum-Over-States Approximation

The Sum-Over-States (SOS) approximation is a useful simplification of the first-order CPHF equations (4.17), in which the coupling of the equations is removed. This is achieved by setting $A_{ai,bj} = 0$, which reduces the CPHF equation (4.17) to (4.31).

$$(\varepsilon_a - \varepsilon_i)U^\lambda_{ai} = \mu^\lambda_{ai} \tag{4.31}$$

By rearranging (4.31) for U^λ and substituting it into (4.28), the expression for the SOS polarisability is obtained (4.32), expressed only in terms of the dipole matrices and orbital energies, and from which the calculation of the polarisability is reduced to a simple sum over states.

$$\alpha_{\lambda\mu} = \frac{4\mu^\lambda_{ai}\mu^\mu_{ai}}{\varepsilon_a - \varepsilon_i} \tag{4.32}$$

Rigorous CPHF Polarisability

By taking the first-order CPHF equations based on the Hartree-Fock condition for the "canonical" Hartree-Fock orbitals (4.19), we are able to calculate the full $\boldsymbol{U}^\lambda$ matrix.

$$U^\lambda_{pq} = \frac{\mu^\lambda_{pq} - A_{pq,bj}U^\lambda_{bj}}{\varepsilon_p - \varepsilon_q} \tag{4.33}$$

By rearranging the CPHF equations for U^λ_{pq}, the resultant equation (4.33), depends on two unknowns in U^λ and as such represents a series of linear equations which need to be solved using an appropriate technique. The following iterative scheme is proposed:

1. Calculate an inital value for U^{λ} using a similar approximation as used for the SOS polarisability i.e. setting $A_{pq,bj} = 0$.

$$U^{\lambda}_{prev,pq} = \frac{\mu^{\lambda}_{pq}}{\varepsilon_p - \varepsilon_q} \tag{4.34}$$

2. Calculate updated values for U^{λ} using equation (4.35):

$$U^{\lambda}_{next,pq} = \frac{\mu^{\lambda}_{pq} - A_{pq,ak}U^{\lambda}_{prev,ak}}{\varepsilon_p - \varepsilon_q} \tag{4.35}$$

3. Repeat procedure from Step 2 until the maximum element of $(|U^{\lambda}_{next,pq} - U^{\lambda}_{prev,pq}|)$ is less than the chosen tolerance[2]. At end of each iteration the U^{λ} matrices are updated i.e. $U^{\lambda}_{next,pq}$ are copied into $U^{\lambda}_{prev,pq}$.

Once a converged value for U^{λ} has been determined by the iterative scheme described above, it is a trivial matter of applying Equation (4.28) to determine the CPHF polarisability.

4.3.3 CPHF First-order Hyperpolarisability

In a similar way to the dipole moment and the polarisability, it was shown in Section 3.2, that the first-order hyperpolarisability $\boldsymbol{\beta}$, is dependent upon the third derivative of the energy. By differentiating the Hartree-Fock energy expression three times with respect to components of the applied electric field, the following expression is obtained:

$$\frac{\partial^3 E}{\partial F_{\lambda}\partial F_{\mu}\partial F_{\nu}} = -4U^{\mu\nu}_{pi}\mu^{\lambda}_{pi} - 4U^{\mu}_{pi}U^{\nu}_{qi}\mu^{\lambda}_{pq} \tag{4.36}$$

Equating the definition of $\boldsymbol{\beta}$ (3.7) with (4.36) gives the expression for the CPHF hyperpolarisability (4.37),

$$\beta_{\lambda\mu\nu} = 4U^{\mu\nu}_{pi}\mu^{\lambda}_{pi} + 4U^{\mu}_{pi}U^{\nu}_{qi}\mu^{\lambda}_{pq} \tag{4.37}$$

[2]The tolerance is chosen to ensure good convergence but not set too low to result in stability problems. A typical tolerance chosen is 1.0×10^{-5}

The derivation of the final expression for the hyperpolarisability contains many steps and the following equations briefly summarise the key stages. Taking the above equation as a starting point and expanding the summations over all orbitals into separate contributions, while making use of the symmetry of the dipole matrices and the second-order orthogonality relation along with the previous definition of $\xi_{pq}^{\mu\nu}$ (4.9), it can be shown that (4.37) reduces to:

$$\beta_{\lambda\mu\nu} = 2\xi_{ab}^{\mu\nu}\mu_{ab}^{\lambda} - 2\xi_{ji}^{\mu\nu}\mu_{ji}^{\lambda} + 4U_{ai}^{\mu\nu}\mu_{ai}^{\lambda} \tag{4.38}$$

By making use of the first- and second-order CPHF equations previously described (4.17,4.21), the final term in (4.38) can be expanded in terms of only first-order quantities, making use of the previous definition of f_{pq}^{μ} (4.22), to give:

$$\begin{aligned}\beta_{\lambda\mu\nu} &= 2\xi_{ab}^{\mu\nu}\mu_{ab}^{\lambda} - 2\xi_{ji}^{\mu\nu}\mu_{ji}^{\lambda} \\ &+ 4\Big\{\frac{1}{2}A_{ai,kj}\xi_{kj}^{\mu\nu} - \frac{1}{2}A_{ai,bc}\xi_{bc}^{\mu\nu} - U_{ka}^{\mu}f_{ki}^{\nu} - U_{ka}^{\nu}f_{ki}^{\mu} - U_{bi}^{\mu}f_{ab}^{\nu} - U_{bi}^{\nu}f_{ab}^{\mu}\Big\}U_{ai}^{\lambda}\end{aligned} \tag{4.39}$$

The final step involves refactoring (4.39) again in terms of $\xi_{pq}^{\mu\nu}$ and f_{pq}^{μ} to give the equation for the CPHF hyperpolarisability $\beta_{\lambda\mu\nu}$, in its final form (4.40).

$$\begin{aligned}\beta_{\lambda\mu\nu} &= 2\xi_{kj}^{\mu\nu}f_{kj}^{\lambda} - 2\xi_{bc}^{\mu\nu}f_{bc}^{\lambda} \\ &+ 2\xi_{ki}^{\nu\lambda}f_{ki}^{\mu} - 2\xi_{ab}^{\nu\lambda}f_{ab}^{\mu} \\ &+ 2\xi_{ki}^{\lambda\mu}f_{ki}^{\nu} - 2\xi_{ab}^{\lambda\mu}f_{ab}^{\nu}\end{aligned} \tag{4.40}$$

This final expression for the CPHF hyperpolarisability comprises two terms which are cyclically permutated and both of which have an interpretation. The first term involves electron "transfer" between an occupied orbital k to an unoccupied orbital a, then a transfer between occupied orbitals j and k, followed by a transfer from orbitals a to k. These terms imply occupied orbital type contributions to the hyperpolarisability, since these transitions involve two occupied orbitals. The second term can be described by a similar transfer process, but one that implies

unoccupied orbital type contributions to the hyperpolarisability since these involve two unoccupied orbitals.

4.4 Calculation of Refractive Indices

In Section 3.2, the possibility of determining bulk electric properties from the corresponding microscopic quantities was introduced. The following section discusses one such method for the calculation of refractive indices from the microscopic polarisability as described by Rohleder and Munn [45]. This method is based on the *oriented gas* approximation, in which a rigorous treatment of the local field is avoided by calculating the refractive indices from the mean polarisability Γ of the unit cell (4.41),

$$\frac{n_i^2 - 1}{n_i^2 + 2} = \frac{\Gamma_i}{3\varepsilon_0 V} \tag{4.41}$$

where V is the volume of the unit cell and ε_0 the vacuum permittivity. The mean polarisability of the unit cell is in turn calculated by a simple additive scheme of the molecular polarisabilities (4.42),

$$\mathbf{\Gamma} = \mathbf{g}\left\{ \sum_{k=1}^{Z} \mathbf{c}^{(k)T} \boldsymbol{\alpha}^{(k)} \mathbf{c}^{(k)} \right\} \mathbf{g}^T \tag{4.42}$$

where $\boldsymbol{\alpha}^{(k)}$ is the polarisability of molecule k, the matrix $\mathbf{c}^{(k)}$ transforms the principal axes of the polarisability of molecule in the unit cell to the axes of unit cell and matrix $\mathbf{g}$ diagonalises the resultant unit cell polarisability.

The motivation for calculating refractive indices stems from the fact that experimentally it is the bulk properties that are measured and it is these quantities that are reported in the literature; the most typical of which are the refractive indices. The conversion of polarisabilities to refractive indices, in theory provides a convenient means to judge the quality of polarisabilities obtained from ab-initio or constrained-wavefunction calculations.

Both microscopic polarisabilities and refractive indices are wavelength dependent, a situation which complicates the comparison of theoretical and experimental

values. Given that the equations previously discussed only yield static polarisabilities, these correspond to the zero-frequency limit, as do the resultant refractive indices calculated with (4.41). By extrapolating the experimental refractive indices to the zero-frequency limit, the comparison with theoretical values is made possible. The extrapolation method is based on an assumed functional form, which is fitted to a series of experimental values measured at a range of wavelengths. Typically, functional forms include the Cauchy equations [54] (4.43) and Sellmeier's formula, a simplified form of which appears in (4.44).

$$n^2 = A + \frac{B}{\lambda^2} + \frac{C}{\lambda^4} + \ldots \tag{4.43}$$

$$n^2 = A + \frac{B\lambda^2}{\lambda^2 - C} \tag{4.44}$$

The constants A, B and C are characteristic of each material and are found by fitting to the experimental data. From these equations it can be seen that the extrapolation to zero frequency depends on the limiting cases of the equations, $n^2 = A$ for the Cauchy equation and $n^2 = A + B$ for the Sellmeier formula.

4.5 Implementation of Routines

Although the ability to calculate CPHF polarisabilities and hyperpolarisabilities has been possible for some time in other widely available quantum-chemistry packages, for example Gaussian [55], these programs lack the ability to perform constrained wavefunction calculations with X-ray diffraction data and in general they do not offer the ability to calculate refractive indices. Since our interest lies in organic NLO materials and getting greater leverage out of high-quality X-ray diffraction data, it seems prudent to implement these routines and make them available in a package that can perform constrained wavefunction calculations. Routines for the calculation of SOS polarisabilities (Equation 4.32), CPHF polarisabilities (Equations 4.28 and 4.35), decomposition of CPHF polarisability into orbital contributions (Equation 4.30), CPHF hyperpolarisabilities (Equation 4.40) and refractive indices (Equations 4.41 and 4.42), were implemented in the Tonto package [37].

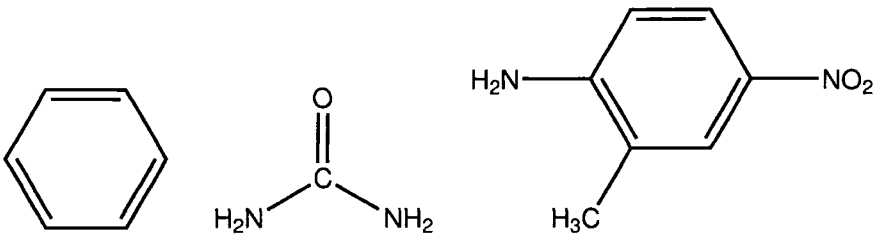

(a) (b) (c)

Figure 4.1: Schematic of (a) benzene (b) urea and (c) MNA

4.6 Compounds of Interest

Benzene, urea and 2-methyl-4-nitroanline (MNA) (Figure 4.1) were chosen because of their suitability for charge-density investigation and because each system has a clear importance in aiding our understanding of linear and non-linear optical properties of molecular crystals. The SHG properties of urea were first reported 1968 [56] and despite its small size, urea possesses a significant gas-phase dipole moment[3] of 3.83(4)D [57], further evidence of considerable charge delocalisation. The NLO material, MNA is one of the simplest NLO systems based on the pNA prototype differing only by a methyl group adjacent to the aniline group, which was successfully introduced to encourage crystallisation in a non-centrosymmetric spacegroup. MNA has also been the subject of much controversy since an early study by S.T. Howard et al [58] suggested that it had an in-crystal dipole moment of 23D corresponding to a considerable dipole moment enhancement of some 15D from that of the isolated molecule. Later theoretical work [59] and the work by Whitten et al [43] suggest a much smaller enhancement. Unlike urea and MNA, benzene cannot be NLO active due to its high symmetry resulting in no net dipole moment and a zero hyperpolarisability, yet this molecule forms the delocalised π-system of many NLO materials and as such warrants much attention.

[3]Unit of measure of dipole moment, Debye(D) $\equiv 3.336 \times 10^{-30}$Cm in SI units

4.7 Fitting Calculations

The contrained wavefunction calculations were based on high-quality charge-density data and performed using the Tonto package [37]. The benzene dataset at 110K was taken from a study by Bürgi et al [60]. Synchrotron data for urea have been collected by Birkedal et al [61] with atomic displacement parameters taken from a neutron study by Swaminathan, McMullan and Craven [62]. The MNA charge-density data was obtained by Whitten et al [63].

Using the same charge-density data and geometry, constrained wavefunction calculations were performed on benzene, urea and MNA, refitting the experimental data to the same levels as reported by Whitten et al [43], in order to provide a good basis for the comparison of the polarisabilities calculated using the approach by Sylvain and Csizmadia discussed in Section 3.3.1 and CPHF polarisabilities discussed in this chapter.

In Section 2.3.1, it was mentioned that one of the drawbacks of the fitting procedure employed in Tonto is the determination of the point at which the fitting should be terminated. A logical end-point to aim for is $\chi^2 = 1$, in which the calculated structure factors are within one standard deviation of the experimental data. However it is reasonable to assume we should be able to achieve similar R-factors in the fit, to those achieved in the multipole refinements, irrespective of the χ^2. It is important to realise though, that both criteria only state the point at which fitting should stop and neither gives any indication of whether those end-points are actually reachable or more importantly meaningful.

The fitting statistics for the refitted calculations along with the original fitting calculation are reported in Table 4.1. In addition to performing constrained wavefunction calculations with the DZP basis set given in Appendix E, it was also decided to try a larger DZP+ basis set with additional diffuse functions to see whether an improved 'experimental' wavefunction could be obtained. In all cases the same levels of fit were achieved irrespective of basis set, though considerable instability in the calculations were observed particularly in the case of MNA. With the larger DZP+ basis set, the same fit is achieved with a much smaller λ value, that is a weaker constraint is applied, which could be expected of a larger, more flexible basis set.

		Energy (au)	λ	χ^2	R(F)	wR(F)
Benzene						
	Orig.	-230.641867	0.590	1.000	0.0185	0.0168
	Refit (DZP)	-230.641909	0.590	1.000	0.0185	0.0168
	Refit (DZP+)	-230.723786	0.222	1.001	0.0185	0.0168
Urea						
	Orig.	-223.947325	0.200	2.362	0.0118	0.0065
	Refit (DZP)	-223.947334	0.200	2.363	0.0118	0.0065
	Refit (DZP+)	-223.995455	0.090	2.354	0.0118	0.0065
MNA						
	Orig.	-528.044199	1.000	2.014	0.0177	0.0159
	Refit (DZP)	-528.044250	1.000	2.014	0.0177	0.0159
	Refit (DZP+)	-528.250749	0.382	1.991	0.0177	0.0159

Table 4.1: Fitting statistics for the constrained wavefunctions performed on benzene, urea and MNA. λ is the Lagrangian multiplier used to constrain the wavefunction.

4.7.1 Verification of the Code

Before determining CPHF polarisabilities and hyperpolarisabilities for compounds involving constrained wavefunctions, it would be prudent to compare the results calculated by these newly implemented routines in Tonto with another widely used quantum-chemistry package. SCF calculations were performed at the D95/RHF level of theory on all three compounds with the molecular geometries taken from the previously mentioned charge-density refinements, and using Gaussian [55] as the benchmark.

Tables 4.2 and 4.3 report SOS polarisabilities and CPHF dipole polarisabilites respectively, both of which show excellent agreement between Tonto and Gaussian, with only negligible differences observed that are most likely down to the numerical precision used by each of the codes. The CPHF hyperpolarisabilities are reported in Table 4.4 and show good agreement especially in the case of urea. Larger discrepancies are however seen for MNA, although there is in general agreement in the relative magnitudes of the tensor components. There are a number of possible sources for

differences between the two codes including, numerical precision and the tolerance used in the iteration scheme, though both the polarisability and hyperpolarisability results clearly indicate that there are no major faults in the implementation of the routines.

	Benzene		Urea		MNA	
	Gaussian	Tonto	Gaussian	Tonto	Gaussian	Tonto
α_{xx}	7.596	7.596	2.539	2.539	16.393	16.393
α_{xy}	-1.224	-1.224	0.728	0.728	-0.366	-0.366
α_{xz}	-3.347	-3.347	0.000	0.000	4.415	4.415
α_{yy}	10.433	10.433	2.539	2.539	16.729	16.729
α_{yz}	-1.217	-1.217	0.000	0.000	-0.712	-0.712
α_{zz}	7.535	7.535	4.466	4.466	8.898	8.898
$\overline{\alpha}$	8.521	8.521	3.175	3.175	14.007	14.007

Table 4.2: Comparison of the components of the SCF SOS polarisability and mean SOS polarisability for TONTO and GAUSSIAN in $\times 10^{-40}$ C m^2 V^{-1}

	Benzene		Urea		MNA	
	Gaussian	Tonto	Gaussian	Tonto	Gaussian	Tonto
E_{tot}	-230.640918	-230.640920	-223.930066	-223.930068	-528.092007	-528.349554
α_{xx}	7.94154	7.94152	3.18488	3.18488	19.17181	19.2468
α_{xy}	-1.27099	-1.27099	1.05531	1.05531	-0.82543	-0.85380
α_{xz}	-3.46908	-3.46907	0.00000	0.00000	5.65227	5.68928
α_{yy}	10.88520	10.88504	3.18488	3.18488	17.03321	17.0416
α_{yz}	-1.26546	-1.26546	0.00000	0.00000	-0.91661	-0.9303
α_{zz}	7.87973	7.87972	5.01975	5.01975	9.70056	9.7177
$\overline{\alpha}$	8.9022	8.9021	3.7965	3.7965	15.3019	15.3354

Table 4.3: Comparison of the components of the SCF CPHF polarisability and mean CPHF polarisability for TONTO and GAUSSIAN in $\times 10^{-40}$ C m^2 V^{-1}

	Urea		MNA	
	Gaussian	Tonto	Gaussian	Tonto
β_{xxx}	0.00000	0.00000	272.944	279.337
β_{xxy}	0.00000	0.00000	-147.667	-150.97
β_{xyy}	0.00000	0.00000	2.53571	3.34713
β_{yyy}	0.00000	0.00001	51.2151	51.3273
β_{xxz}	2.73932	2.73931	135.005	138.06
β_{xyz}	2.96016	2.96015	-67.5584	-68.8262
β_{yyz}	2.73932	2.73931	-2.56790	-2.19429
β_{xzz}	0.00000	0.00000	60.1962	61.6183
β_{yzz}	0.00000	0.00000	-28.3363	-28.9245
β_{zzz}	-9.10438	-9.10441	23.3760	24.0121

Table 4.4: Comparison of the SCF CPHF hyperpolarisability for TONTO and GAUSSIAN in $\times 10^{-52}$ C m^3 V^{-2}

4.8 Results

This chapter is concerned with the characterisation of both the linear and non-linear optical properties of three model compounds, benzene, urea and MNA by means of Coupled Perturbed Hartree-Fock (CPHF) calculations from 'experimental' wavefunctions derived using constrained wavefunction fitting to high-resolution X-ray diffraction data. For each material, the principle components of the dipole polarisability and for completeness, the full polarisability tensors are reported along with the refractive indices and where relevant, the hyperpolarisability. These have been compared with experimental values where possible and with the results of a previous study involving wavefunction fitting and ab-initio calculations by Whitten [43, 53].

4.8.1 Benzene

The principal components of the dipole polarisability along with the mean polarisability for benzene are reported in Table 4.5 for a series of wavefunction fitted

	α_{xx}	α_{yy}	α_{zz}	$\overline{\alpha}$
Fitted CPHF/DZP	4.16	11.65	11.80	9.20
Fitted CPHF/DZP+	6.97	12.68	12.72	10.80
Fitted Sylvain-Csiz.†	6.92	12.97	13.29	11.06
CPHF†	7.18	12.77	12.77	10.91
MP2†	7.25	13.40	13.40	11.25
HF/Sadlej†	7.50	13.10	13.10	11.23
MP4(SDQ)/Sadlej†	7.38	13.19	13.19	11.25
Experiment [64]	7.41(22)	13.64(16)	13.64(16)	11.56(10)

Table 4.5: Benzene: Principal components of the dipole polarisability and mean polarisability in $\times 10^{-40}$ C m^2 V^{-1}, † from Whitten [53].

and ab-initio calculations along with a single experimental result, which is reported for reference only, since the effects of vibrational averaging and of the frequency dependence have not been taken into consideration in the calculations.

However, there is a high degree of consistency between the experimental polarisability and those obtained from theoretical calculations, particularly at the higher levels of theory. In fact, they appear to be better than any of those obtained by constrained wavefunction fitting, though the CPHF/DZP+ and Sylvain-Csizmadia results show fairly good agreement, having similar relative magnitudes and anisotropies. It is interesting to note however, that all three constrained wavefunction calculations show a discrepancy between the two principal components α_{yy} and α_{zz}, which should be identical due to the symmetry of the material as is seen for the purely theoretical results.

Disappointingly, it appears that the fitted Sylvain-Csizmadia dipole polarisabilities are in better agreement with the theorical/experimental polarisabilities than those obtained using the fitted CPHF method. In fact, it appears that a larger DZP+ basis is required in order to get a result comparable with the Sylvain-Csizmadia/DZP dipole polarisability. Furthermore, by comparing the ab-initio CPHF result with the wavefunction-fitted CPHF polarisability, it appears that in this particular case, the ab-initio calculation is much better at reproducing accurate dipole polarisabilities

	Fitted CPHF/DZP	Fitted CPHF/DZP+
α_{xx}	8.324	10.052
α_{xy}	-1.355	-0.980
α_{xz}	-3.549	-2.684
α_{yy}	11.181	12.330
α_{yz}	-1.303	-0.975
α_{zz}	8.109	10.004

Table 4.6: Benzene: Dipole polarisability tensor components and mean polarisability in $\times 10^{-40}$ C m^2 V^{-1}

with the fitted CPHF calculation predicting unexpectedly a smaller overall dipole polarisability. In practice, one would not expect to observe much of a difference between the ab-initio and constrained wavefunction dipole polarisabilities given that the intermolecular interactions between benzene molecules in the crystal are particularly weak.

A closer look at the differences between the two CPHF polarisabilities is given in Table 4.6, which shows similar relative magnitudes for all components but with consistently smaller components of the tensor observed for the CPHF/DZP calculation, suggesting that it may systematically underestimate the dipole polarisability of benzene.

Using Equations 4.41 and 4.42, the corresponding refractive indices (Table 4.7) have been calculated from the dipole polarisabilities reported above. In order to facilitate the comparison with calculated refractive indices, their frequency dependance has to be taken into consideration. This was achieved by applying a correction based on the Cauchy equations for liquid benzene [66] to the experimental refractive indices [45, 67].

From Equation 4.41 it can be seen that the refractive indices are also dependent on the number density, the number of molecules in a volume V. Since the unit-cell volume is temperature dependent, it was important to use the unit-cell volume at which the experimental refractive indices were recorded and not the cell volume at which the X-ray diffraction data were collected. Using the coefficients of thermal

	n_1	n_2	n_3
Exp. [65]	1.544	1.646	1.550
Corr. (zero freq.)	1.514	1.614	1.520
HF†	1.532	1.643	1.497
MP2†	1.556	1.682	1.517
Fitted Sylvain-Csiz.†	1.542	1.663	1.496
Fitted CPHF/DZP	1.422	1.444	1.630
Fitted CPHF/DZP‡	1.379	1.399	1.561
Fitted CPHF/DZP+	1.515	1.533	1.804
Fitted CPHF/DZP+‡	1.461	1.476	1.709

Table 4.7: Benzene: Refractive indices. †From Whitten [53]. ‡Adjusted for unit-cell volume at temperature of experimental values.

expansion at 270K [68], new cell constants were calculated and used to determine CPHF refractive indices denoted ‡. Refractive indices calculated using the unit cell volume at the temperature of the data collection are reported for comparison.

Accounting for the change in unit cell volume has an appreciable effect on the refractive indices, having the effect of reducing each component by a small amount. As expected, based on the previously reported dipole polarisabilities, the CPHF fitted results show the least satisfactory agreement with the ab-initio and experimental values, seeming to underestimate the refractive indices of benzene and curiously exhibiting a different anisotropy with n_2 and n_3 seemingly switched round with respect to the other reported values.

Unlike for both urea and MNA, the presence of an inversion centre in the crystal packing precludes benzene from being NLO active and so the hyperpolarisability is zero and consequently not reported.

4.8.2 Urea

Dipole polarisabilities for Urea are given in Table 4.8, calculated from both wavefunction-fitted and ab-initio calculations. The results obtained from the CPHF/DZP+ fitted approach is in good agreement with both the fitted Sylvain-Csizmadia and theoret-

	α_{xx}	α_{yy}	α_{zz}	$\overline{\alpha}$
Fitted CPHF/DZP+	4.30	6.61	6.73	5.88
Fitted Sylvain-Csiz.†	4.55	6.98	6.94	6.15
CPHF†	3.86	5.69	5.83	5.13
MP2†	4.40	6.79	6.87	6.02
HF/Sadlej†	4.03	5.87	6.14	5.35
MP4(SDQ)/Sadlej†	4.57	6.81	7.10	6.16

Table 4.8: Urea: Principal components of the dipole polarisability and mean polarisability in $\times 10^{-40}$ C m^2 V^{-1}. †From Whitten [53].

ical estimates. As was seen for benzene, the CPHF/DZP+ again predicts a slightly smaller polarisability than the Sylvain-Csizmadia results with a mean polarisability of 5.88 versus 6.15 for the latter. For completeness the full polarisability tensor is reported in Table 4.9.

	Fitted CPHF/DZP+
α_{xx}	5.515
α_{xy}	1.216
α_{xz}	0.000
α_{yy}	5.515
α_{yz}	0.000
α_{zz}	6.612
$\overline{\alpha}$	5.880

Table 4.9: Urea: Dipole polarisability tensor components and mean polarisability in $\times 10^{-40}$ C m^2 V^{-1}

In the same way as for benzene, the experimental refractive indices were corrected to the zero-frequency limit using Sellmeier coefficients [70]. Thermal expansion coefficients [71] were also used to scale the wavefunction-fitted CPHF to account for the differing number density at the temperature of the experimental measurement.

The fitted CPHF refractive indices are in good agreement with both the experimental and MP2 values. Again, the fitted CPHF results predict slightly smaller

	n_1	n_2
Exp. [69]	1.507	1.636
Corr. (zero freq.)	1.477	1.583
HF†	1.395	1.496
MP2†	1.473	1.606
Fitted Sylvain/Csiz.†	1.490	1.614
Fitted CPHF/DZP+	1.481	1.599
Fitted CPHF/DZP+‡	1.463	1.574

Table 4.10: Urea: Refractive indices ($n_1 = n_1'$). †From Whitten [53]. ‡Adjusted for unit-cell volume at temperature of experimental values.

values of the indices when compared to the fitted Sylvain-Csizmadia result.

Fitted CPHF/DZP+			
β_{xxx}	0.000	β_{xyz}	-12.571
β_{xxy}	0.000	β_{yyz}	-3.134
β_{xyy}	0.000	β_{xzz}	0.000
β_{yyy}	0.000	β_{yzz}	0.000
β_{xxz}	-3.134	β_{zzz}	45.848

Table 4.11: Urea: Dipole hyperpolarisability tensor components in $\times 10^{-52}$ C m^3 V^{-2}

	Fitted CPHF/DZP+
β_x	0.000
β_y	0.000
β_z	39.580

Table 4.12: Urea: Vector dipole hyperpolarisability in $\times 10^{-52}$ C m^3 V^{-2}

Urea was one of the first materials to be recognised for its non-linear optical response and as such, we report here for reference, the full tensor of the dipole hyperpolarisability and the vector hyperpolarisability (Tables 4.11 and 4.12 respectively)

4.8.3 MNA

	α_{xx}	α_{yy}	α_{zz}	$\overline{\alpha}$
Fitted CPHF/DZP+	9.93	18.90	27.01	18.63
Fitted Sylvain-Csiz.†	9.59	18.10	25.51	17.73
CPHF†	10.00	18.47	23.19	17.22
MP2†	10.59	20.13	26.79	19.17

Table 4.13: MNA: Principal components of the dipole polarisability and mean polarisability in $\times 10^{-40}$ C m^2 V^{-1}. †From Whitten [53]

The dipole polarisabilites of MNA, the most complex molecule in the series, are reported in Table 4.13. Very good correspondence is observed for all results with the agreement between the fitted CPHF components and the MP2 calculation of particular note. For the first time, the CPHF method seems to estimate principal components with better agreement than the Sylvain-Csizmadia approach, used in the previous work by Whitten et al [43].

	Fitted CPHF/DZP+
α_{xx}	23.592
α_{xy}	-1.517
α_{xz}	6.356
α_{yy}	19.344
α_{yz}	-1.181
α_{zz}	12.906
$\overline{\alpha}$	18.628

Table 4.14: MNA: Dipole polarisability tensor components and mean polarisability in $\times 10^{-40}$ C m^2 V^{-1}

For reference the full dipole polarisability tensor is given in Table 4.14.

Sellmeier coefficients at 300K [72] were used to compute the refractive indices at zero frequency, in addition, the unit cell was adjusted to account for the expansion of the cell at the temperature of the experimental reading using room-temperature cell constants [73, 74].

	n_1	n_2	n_3
Exp. [72]	2.764(2)	1.866(3)	1.464(1)
Corr. (zero freq.)	1.953	1.719	1.436
CPHF†	1.935	1.709	1.339
MP2†	2.162	1.800	1.361
Fitted Sylvain-Csiz.†	2.071	1.699	1.323
Fitted CPHF/DZP+	2.239	1.773	1.384
Fitted CPHF/DZP+‡	2.053	1.677	1.343

Table 4.15: MNA: Refractive indices. †From Whitten [53]. ‡Adjusted for unit-cell volume at temperature of experimental values.

The CPHF results from the constrained-wavefunction calculations show similar relative magnitudes and anisotropies to the experimental and ab-initio values. Surprisingly the best agreement with the experimental refractive indices is with the ab-initio CPHF values, although the consistency exhibited for all the wavefunction-fitted results and the higher-level MP2 calculation may suggest that the experimental value is overcorrected when accounting for the frequency dispersion.

Fitted CPHF/DZP+			
β_{xxx}	-321.695	β_{xyz}	87.936
β_{xxy}	176.651	β_{yyz}	-3.309
β_{xyy}	-9.194	β_{xzz}	-67.599
β_{yyy}	-44.787	β_{yzz}	35.691
β_{xxz}	-170.590	β_{zzz}	-16.992

Table 4.16: MNA: Dipole hyperpolarisability tensor components in $\times 10^{-52}$ C m^3 V^{-2}

In a similar manner to urea, the full hyperpolarisability tensor and vector hyperpolarisability are reported in Tables 4.16 and 4.17 respectively. A comparison of experimental hyperpolarisabilities with those obtained from constrained wavefunction fitting is defered until Section 5.6 in the following chapter.

	Fitted CPHF/DZP+
β_x	-398.488
β_y	167.555
β_z	-190.891

Table 4.17: MNA: Vector dipole hyperpolarisability in $\times 10^{-52}$ C m^3 V^{-2}

4.9 Conclusions

In this chapter, the first examples of calculating CPHF (hyper)polarisabilities from constrained wavefunction-fitting calculations have been presented. The relevant CPHF equations discussed above were implemented in the TONTO package and verified against those reported by Gaussian. Additionally, refractive indices were calculated for benzene, urea and MNA using the Rohleder and Munn method [45] and compared with experimental values extrapolated to zero frequency.

The most striking feature of this study was the lack of consistency in the observed agreements from one compound to the next. In the case of benzene, the fitted dipole polarisabilities/refractive indices were notable different from the ab-initio and experimental results, whereas for urea and MNA these values were much more comparable. Furthermore the fitted CPHF results were expected to have shown a significant improvement over the Sylvain-Csizmadia method used previously, however this was only observed once in the case of the dipole polarisability and refractive indices of MNA.

One would also expect that the constrained wavefunction calculation should be able to reproduce better the experimental refractive indices since extra information on crystal effects is included by way of the X-ray diffraction data. This was not always the case, as shown by the closer agreement between experiment and ab-initio calculations of the dipole polarisabilities of benzene.

Overall it appears that relatively good estimates of the CPHF polarisabilities and hence refractive indices can be obtained from constrained-wavefunction calculations. However it is not entirely clear why, in the case of benzene, the wavefunction-fitted CPHF results faired so poorly compared to the other results, since exactly the same X-ray data were used in the fitted Sylvain-Csizmadia calculation and also given that

the ab-initio CPHF gave a reasonable estimate of the dipole polarisability.

In addition to determining the dipole polarisabilities, we were able for the first time to report CPHF hyperpolarisabilities for fitted calculations. However, given the variability of the dipole polarisabilities and considering the fact that the hyperpolarisability is a much more sensitive quantity to calculate, it is doubtful that the values presented in this chapter can be used for anything other than a qualitative guide at the present time, but an excellent and optimistic foundation for future research.

Chapter 5

A Series of Constrained Wavefunction-Fitting Calculations

5.1 Introduction

Continued interest in molecular crystals as potential NLO materials has resulted in the discovery of many organic NLO materials. Three such materials, 4-(*N*,*N*-dimethylamino)-3-acetamidonitrobenzene (DAN), 2-(*N*-L-prolinol)-5-nitropyridine (PNP) and (S)-2-(α-methylbenzylamino)-5-nitropyridine (MBANP), were selected from the literature due to their substantial NLO behaviour. A discussion of the structural details of these materials can be found in Section 3.5.

Although preliminary investigations aimed at characterising these materials optically have been carried out on DAN [75,76], MBANP [77,78] and PNP [79], there has been to our knowledge no charge-density studies performed on these materials to date. Consequently, high-quality charge-density datasets have been collected for these materials and multipole refinements carried out by Dr D.S. Yufit of the University of Durham [80].

The availability of high-resolution X-ray diffraction data of high quality, provided sufficient motivation to try to obtain "experimental" wavefunctions consistent with the X-ray data. As such, constrained wavefunction calculations were performed on DAN, MBANP and PNP with the aim of yielding quantitative estimates of the solid-state dipole polarisability, refractive indices and first-order hyperpolarisability.

In addition, these calculations also provided the basis for a detailed comparison with the multipole refinements of the same compounds, which is the subject of Chapter 6.

5.2 Details of the Calculations

All constrained wavefunction calculations were performed with the Tonto program [37] using the cc-pVDZ basis set. Attempts were made to fit all the calculations to a level corresponding to the same R-factors as achieved by the multipole refinements and not aiming for $\chi^2 = 1$ (as mentioned in Section 2.3.1). In addition, since the results of these calculations are the basis for a comparison with those obtained from charge-density studies, exactly the same data used in the multipole refinements were also fitted in the constrained-wavefunction calculations. This is an important consideration since typically not all of the available data is used in multipole refinements.[1] For each compound, values calculated from the constrained wavefunction for the CPHF polarisability, CPHF hyperpolarisability and refractive indices are reported, along with a discussion of the effect and quality of the fit of the wavefunction to the experimental data.

Since there is no convenient way to compare wavefunctions directly, differences in some chosen parameter taken before and after wavefunction fitting provides a means of estimating the effect of the fitting procedure. An obvious parameter to choose is the electron density $\rho(\mathbf{r})$, from which we can define the difference density $\Delta\rho(\mathbf{r})$, as given in Equation (5.1). As such $\Delta\rho(\mathbf{r})$ shows the change in the calculated electron density by inclusion of the experimental data and represents in effect a kind of deformation density.

$$\Delta\rho(\mathbf{r}) = \rho_{fit}(\mathbf{r}) - \rho_{ab-initio}(\mathbf{r}) \tag{5.1}$$

There are a number of ways in which the quality of the fit may be judged. The "Crystal Error" map is a Fourier map based on $|F_c - F_o|$, where F_c are the

[1] A discussion of the criteria that may be used for omitting reflections from XD multipole refinements and reasons for such filtering are discussed in Appendix D.3.

(calculated) model structure factors and F_o represents the (observed) experimental structure factors. This map shows the difference between the calculated and observed structure factors in terms of the residual electron density unaccounted for by the model, which in this case is the "experimental" wavefunction.

Although the agreement between F_c and F_o is reflected in the R-factors, a more comprehensive method is to examine the agreement on a per reflection basis. As such the quantity F_z is defined as:

$$F_z = \frac{(F_o - F_c)}{\sigma(F_o)} \tag{5.2}$$

By plotting F_z versus $(\sin\theta/\lambda)$, we can observe the effect of resolution on the agreement. In addition, by plotting F_z versus F_o, we can also observe any effects, that may be a function of the magnitude of the experimental data.

5.3 Constrained Wavefunction Fitting of DAN

The statistics for the constrained wavefunction calculation on DAN are reported in Table 5.1. Also included for reference are the statistics for the multipole refinement and for a calculation in which no fitting was performed ($\lambda = 0.000$). The low value of the initial χ^2 indicates that before fitting there is already good agreement between the model and experimental data, which suggests there is not much more extra information in the data to be included in the model.

	Multipole	$\lambda = 0.000$	$\lambda = 1.020$
Total Energy(au)	-	-774.113142	-774.008384
χ^2	0.6708	1.067417	0.658470
$R(F)$	0.0213	0.026219	0.022072
$R_w(F)$	0.0224	0.029522	0.023187

Table 5.1: Fitting statistics for DAN

We see in Table 5.1, that the total energy of the system increases during fitting, while the χ^2 decreases between the unfitted and fitted calculations, as is expected. Figure 5.1(d) also shows this same trend over the whole fitting procedure. That is,

as λ increases the constraint is applied more strongly, so χ^2 falls. Consequently, the total energy must increase because the unfitted ab-initio result already corresponds to the lowest energy state found by application of the variation principle.

Also reported in Table 5.1 are the standard crystallographic agreement statistics $R(F)$ and $R_w(F)$, which are defined as follows:

$$R(F) = \frac{\sum(|F_o| - |F_c|)}{\sum(|F_o|)} \qquad R_w(F) = \sqrt{\frac{\sum[w(F_o - F_c)^2]}{\sum(wF_o^2)}}$$

As previously mentioned, the end point of the fitting procedure was selected on the basis of achieving the same agreement statistics in the fitted result as was obtained for the multipole refinement. This criteria makes no claims about whether this is achievable. For DAN, the fitting became unstable if λ was increased beyond a value of 1.02, though at this λ, the differences between the agreement statistics are relatively small.

The difference map is shown in Figure 5.1(c), where the plane was defined in terms of atoms C(2), C(3) and C(4)[2], which leaves the N,N-dimethyl and amide side chains out of the plane and the nitro group almost in plane. For those atoms that reside in the plane, we observed significant core deformations in the difference map, implying a loss of charge from the core regions during the fitting procedure.

It is interesting to note, that these conspicuous core deformations are seen to a lesser degree for C(1) and not at all present for atoms C(5) and C(6). Further investigation, revealed that the description of the benzene ring in the constrained wavefunction calculations was not planar but slightly puckered, which probably prevents these features from being observed in the plane defined by C(2), C(3) and C(4). This unexpected and apparently energetically unfavorable geometry of the phenyl ring could be the result of the steric requirements of the bulky N,N-dimethyl and amide substituents, though it could equally be the result of a lack of using a suitable constraint in the multipole refinement. There are also other apparent changes, though less localised, for nearly all the non-hydrogen atoms in

[2]A skeleton diagram showing the structure and labelling of DAN corresponding to the difference and crystal error maps is given in Figure 5.1(a)

the difference map, the most obvious of which occurs at the position of O(1) in the nitro group.

Very little residual electron density remains after the fitting as shown by the crystal-error map, Figure 5.1(b). The lack of significant features confirms the flexibility of the fitting procedure for including all the information from the experimental data. The quality of fitting is further shown by Figures 5.1(e) and 5.1(f). In the plot of F_z against $\sin\theta/\lambda$, it can be seen that the data are evenly distributed about zero with the majority having an F_z of two or less, which means on average the calculated structure factors are within two standard deviations of the experimental structure factors. There is also no apparent angular dependance of the distribution which confirms that the procedure is fitting to the high- and low-angle data equally well. Likewise in the plot of F_z versus F_{exp}, there is essentially an even spread of points with the expected Gaussian distribution.

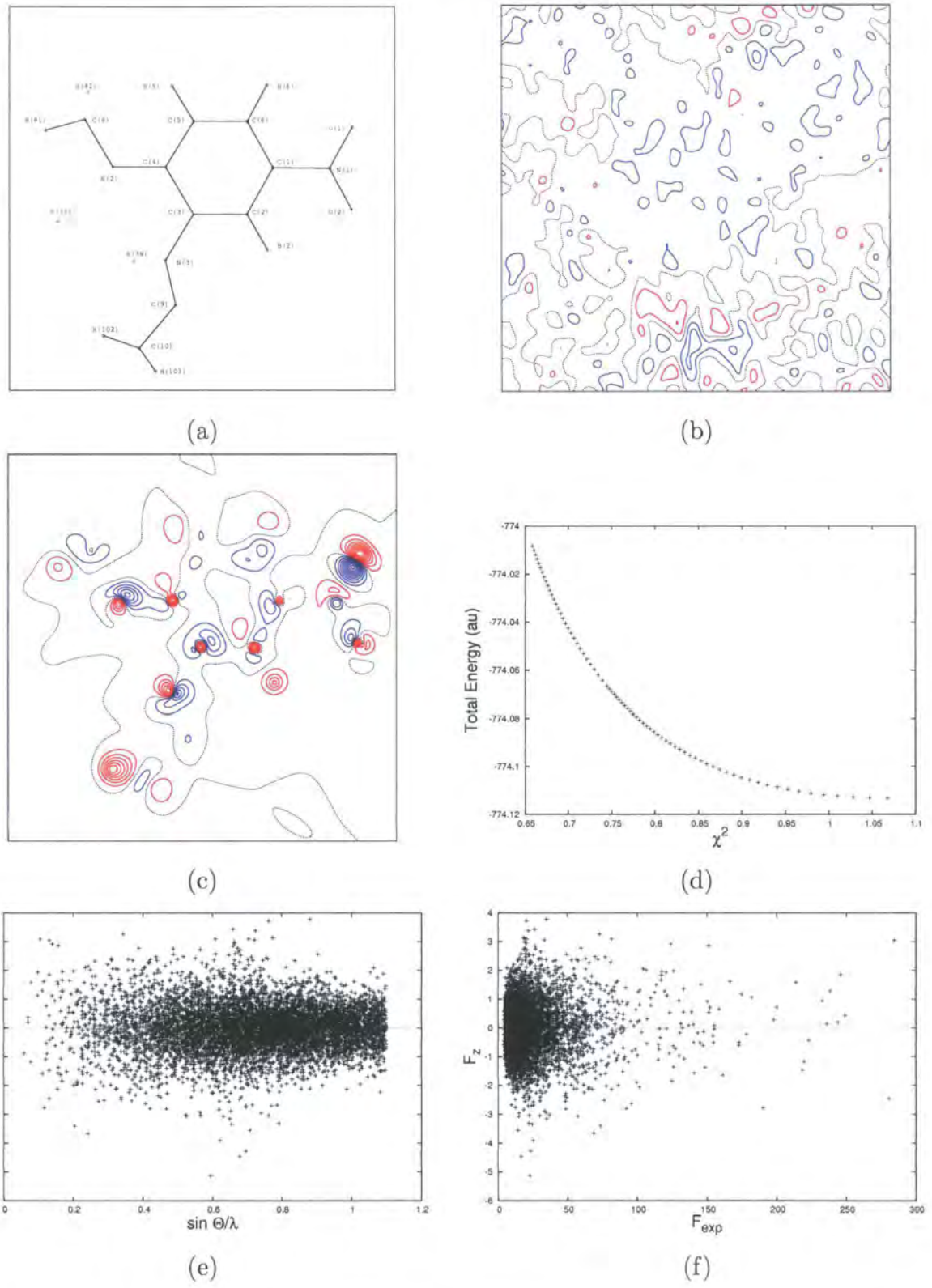

Figure 5.1: DAN: Details of the wavefunction fitting; (a) Atomic Labels (b) Crystal Error Map (c) Difference Density (d) Total Energy vs χ^2 (e) F_z vs $\sin\theta/\lambda$ (f) F_z vs F_o. Contours at intervals of 0.05eÅ^{-3}. Blue contours indicate positive regions and red indicate negative regions.

5.3.1 Properties of DAN

The principal components of the polarisability are given in Table 5.2 and the full polarisability tensor is given in Table 5.3 for both the unfitted and fitted wavefunctions. The directions of the principal axes of the polarisability for the fitted wavefunction are also shown in Figure 5.2. A similar anisotropy is observed for both the unfitted and fitted calculations though an appreciable increase in the principal components is observed, which is expected due to the effects of the crystal field and the intermolecular interactions having been included as part of the fitting process.

	α_{xx}	α_{yy}	α_{zz}	$\overline{\alpha}$
Unfitted (CPHF)	12.003	24.959	28.724	21.895
Fitted (CPHF)	12.354	26.235	30.912	23.167

Table 5.2: DAN: Principle components of the dipole polarisability and mean polarisability in $\times 10^{-40}$ C m^2 V^{-1}

	Unfitted (CPHF)	Fitted (CPHF)
α_{xx}	19.306	20.358
α_{xy}	5.667	6.275
α_{xz}	-5.317	-6.040
α_{yy}	20.795	22.043
α_{yz}	2.408	2.238
α_{zz}	25.584	27.100

Table 5.3: DAN: Dipole polarisability tensor components and mean polarisability in $\times 10^{-40}$ C m^2 V^{-1}

As mentioned in Section 4.3.2, the polarisability can be decomposed into separate contributions of pairs of molecular orbitals. We must consider pairs of orbitals since the polarisability can be considered to be comprised of terms representing transitions between different molecular orbitals. The five largest contributions to the molecular polarisability are reported in Table 5.4 for DAN. Since a molecule of DAN has 118 electrons and each molecular orbital holds two electrons, there must be 59 occupied molecular orbitals (numbered from 1 to 59) and 59 unoccupied (numbered 60-118).

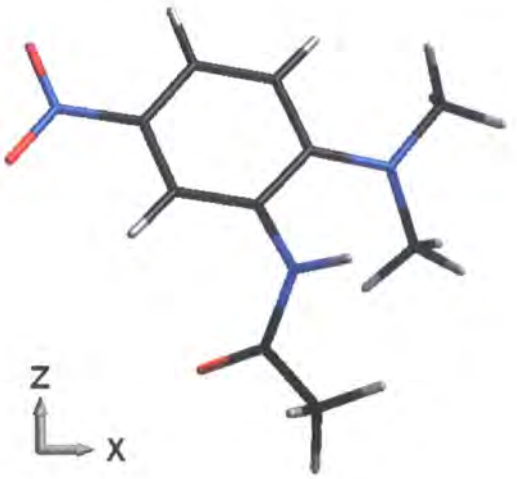

Figure 5.2: Principal axes of the polarisability with respect to the orientation of a DAN molecule; the y-axis is perpendicular to the page, defining a right-handed coordinate system.

The pairs of numbers in the 'Fitted' column indicate that different molecular orbitals have larger contributions than is observed for the unfitted calculation.

The polarisability appears to be completely dominated by a single contribution from the orbitals (1,59). The next signicant contributions are from (2,59), (1,58) and (2,58). It is also interesting to note that the 5^{th} largest contribution comes from a different orbital pair for the unfitted (4,58) and fitted wavefunctions (1,54).

Orbital 1	Orbital 2	Contrib. (Unfitted)	Contrib. (Fitted)
1	59	4.158	5.335
2	59	1.685	1.814
1	58	1.152	0.942
2	58	0.944	0.844
4	58	0.560	0.805 (1,54)

Table 5.4: DAN: Molecular orbital pair contributions to the polarisability

From the dipole polarisabilities reported above we are able to calculated refractive indices for DAN from both the fitted and unfitted wavefunctions (Table 5.5).

Since these calculated refractive indices are frequency independent, the experimental values must be corrected for dispersion.

	n_1	n_2	n_3
Exp. @ 496.5 nm	1.574(7)	1.779(5)	2.243(9)
Exp. @ 1064 nm	1.517(7)	1.636(5)	1.843(9)
Exp. Corrected	1.512	1.624	1.805
Unfitted	1.382	1.507	1.756
Fitted	1.397	1.544	1.829
Unfitted‡	1.368	1.488	1.723
Fitted‡	1.382	1.522	1.792

Table 5.5: DAN: Refractive indices. ‡Adjusted for unit-cell volume at temperature of experimental values.

In the case of DAN, experimental values from Keroc [81] were extrapolated using a one-oscillator model of the form: [82]

$$n^2 - 1 = \frac{q}{\lambda_0^{-2} - \lambda^{-2}} + A \tag{5.3}$$

Where q is related to the oscillator strength p, by $q = p/(2\pi c)^2$. λ_0 is the wavelength of the oscillator and A is a constant contribution from all the other oscillators. The refractive indices from the calculations were also adjusted to account for the differing number density by using room-temperature cell constants taken from an average of the room-temperature cells reported by Baumert et al [76], Clark et al [83] and Norman et al [75].[3]

All the reported refractive indices show a similar anisotropy with the constrained wavefunction predicting marginally larger refractive indices than those obtained from the ab-initio unfitted calculation. Both of which, however seem to underestimate the experimental refractive indices which have been corrected for dispersion.

In addition to the dipole polarisability, the hyperpolarisability and vector hyperpolarisability were also calculated for DAN as shown in Tables 5.6 and 5.7 respec-

[3]Adjusted refractive indices are denoted by the ‡ symbol.

	UnFitted (CPHF)	Fitted (CPHF)
β_{xxx}	42.680	84.953
β_{xxy}	33.073	60.399
β_{xyy}	-2.679	10.228
β_{yyy}	-4.029	-41.616
β_{xxz}	-8.874	-143.688
β_{xyz}	-6.177	-95.328
β_{yyz}	-1.599	-29.007
β_{xzz}	117.672	189.081
β_{yzz}	90.570	133.031
β_{zzz}	-69.382	-142.825

Table 5.6: DAN: Dipole hyperpolarisability tensor components in $\times 10^{-52}$ C m^3 V^{-2}

	Unfitted (CPHF)	Fitted (CPHF)
β_x	157.673	284.261
β_y	83.348	151.814
β_z	-174.111	-315.520

Table 5.7: DAN: Vector dipole hyperpolarisability in $\times 10^{-52}$ C m^3 V^{-2}

tively. A marked change is observed between the unfitted CPHF calculation and the constrained wavefunction calculation, with the latter suggesting a considerable increase which can be attibuted to the effects of crystal field introduced via the fitting procedure. The validation of the hyperpolarisabilities obtained from wavefunction fitting by means of a comparison with experimental results is given later in this chapter in Section 5.6 for all three materials.

5.4 Constrained Wavefunction Fitting of MBANP

A similar constrained wavefunction calculation was performed on MBANP[4], which reached a χ^2 of 0.8362 for a fitting parameter of 0.9. The full fitting statistics are

[4]A labelled diagram of the molecular structure of MBANP is shown in Figure 5.3(a).

reported in Table 5.8 along with the multipole refinement R-factors for reference.

	Multipole	$\lambda = 0.000$	$\lambda = 0.900$
Total Energy(au)	-	-812.879629	-812.711624
χ^2	0.8911	1.774275	0.836207
$R(F)$	0.0216	0.028078	0.022157
$R_w(F)$	0.0193	0.028122	0.019306

Table 5.8: Fitting statistics for MBANP

After the fitting, very little residual electron density was observed (Figure 5.3(b)) and the difference map (Figure 5.3(c)) shows many of the same features found for DAN. Namely, significant core deformations for the aromatic carbon atoms and some more diffuse deformation features around the other non-hydrogen atoms, for example the oxygen atoms of the nitro group.

As expected, there is a smooth increase in the total energy of the system as the constraint is applied more strongly shown by a falling χ^2 (Figure 5.3(d)). The quality of the fit is further highlighted in Figures 5.3(e) and (f), where very few badly fitting reflections are observed and the distributions equally spread on either side of $F_z = 0$, indicating that there is no angular or intensity bias in the fitting of the data.

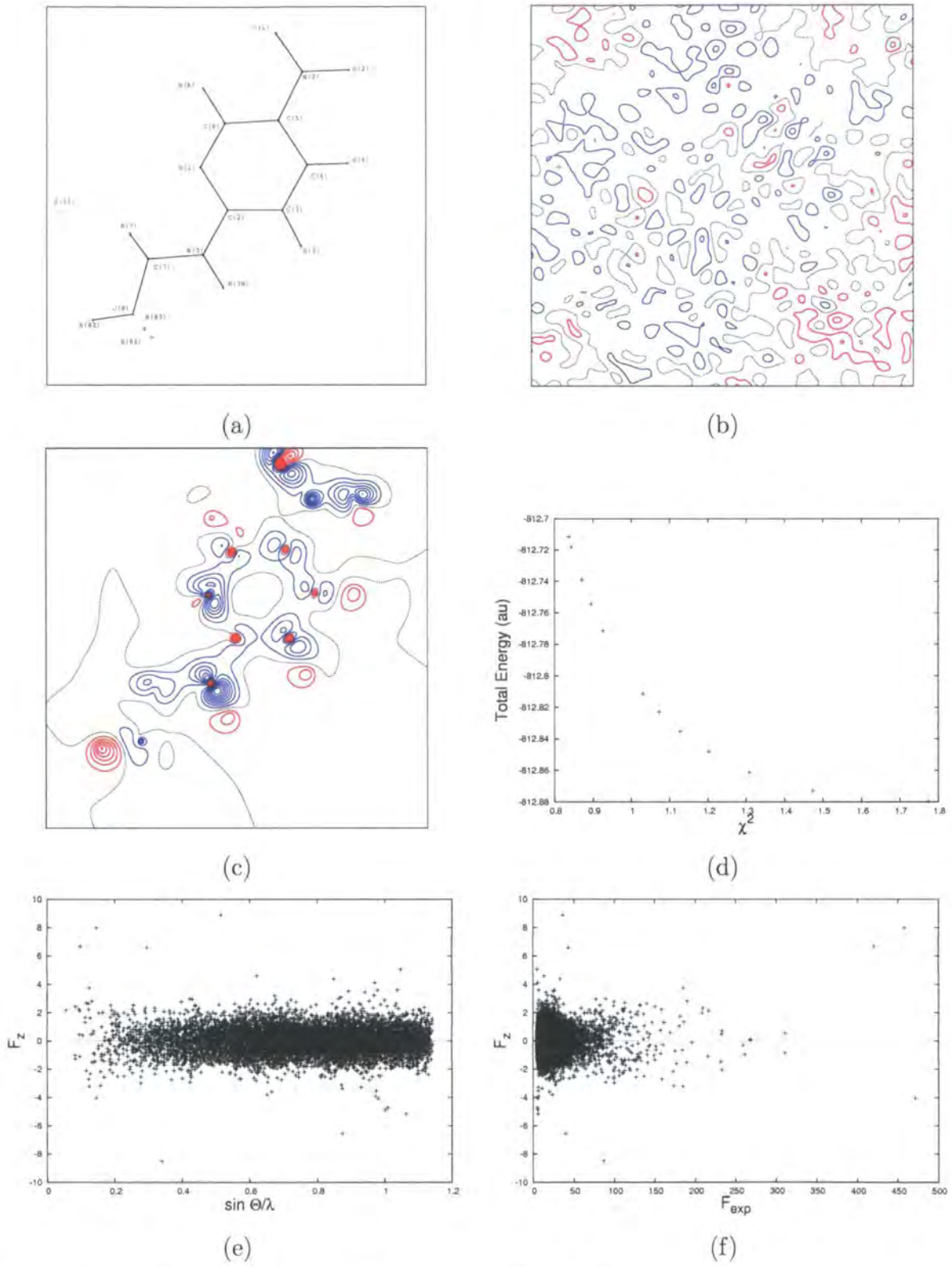

Figure 5.3: MBANP: Details of the wavefunction fitting; (a) Atomic Labels (b) Crystal Error Map (c) Difference Density (d) Total Energy vs χ^2 (e) F_z vs $\sin\theta/\lambda$ (f) F_z vs F_o. Contours at intervals of 0.05eÅ^{-3}. Blue contours indicate positive regions and red indicate negative regions.

5.4.1 Properties of MBANP

The principal components of the polarisability and mean polarisability are reported in Table 5.9, the directions of which correspond to those indicated in Figure 5.4. Smaller increases are seen for each principal component and for the mean polarisability in going from the unfitted to the fitted wavefunction than was observed for DAN, a feature which is also observed in the full polarisability tensor given in Table 5.10.

	α_{xx}	α_{yy}	α_{zz}	$\overline{\alpha}$
Unfitted (CPHF)	20.597	26.242	30.847	25.895
Fitted (CPHF)	20.959	26.570	31.919	26.482

Table 5.9: MBANP: Principle components of the dipole polarisability and mean polarisability in $\times 10^{-40}$ C m^2 V^{-1}

	Unfitted (CPHF)	Fitted (CPHF)
α_{xx}	23.132	23.767
α_{xy}	-1.985	-2.021
α_{xz}	2.011	1.955
α_{yy}	26.558	27.197
α_{yz}	3.482	4.023
α_{zz}	27.997	28.483

Table 5.10: MBANP: Dipole polarisability tensor components and mean polarisability in $\times 10^{-40}$ C m^2 V^{-1}

The molecular-orbital-pair contributions to the polarisability are reported in Table 5.11. MBANP has 129 electrons occupying 64 molecular orbitals (numbered 1-64) and correspondingly 64 unoccupied molecular orbitals (numbered 65-129).

Like in the case of DAN, the decomposition of the dipole polarisability again shows that a single transition, this time involving molecular orbitals 1 and 64 dominates the contributions. Additionally in going from the fitted to the unfitted calculations, we observe that one of the contributions arises from a completely different

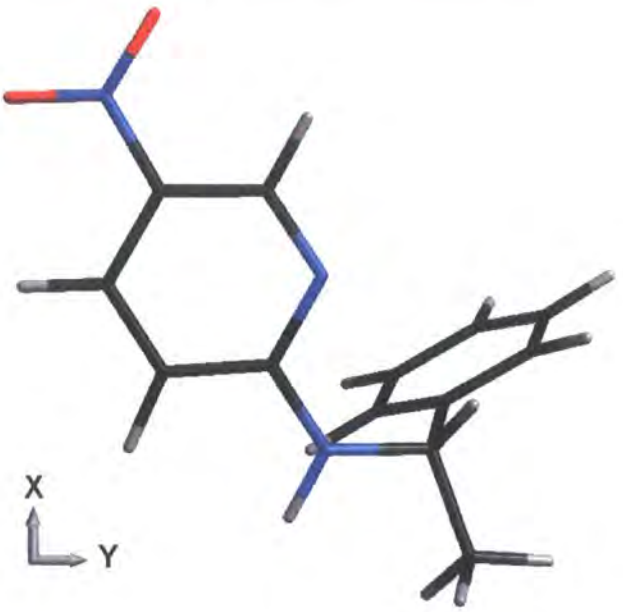

Figure 5.4: Principal axes of the polarisability with respect to the orientation of a MBANP molecule; the z-axis is perpendicular to the page, defining a right-handed coordinate system.

pair of molecular orbitals, while the magnitude of the contributions from two of the pairs, namely (4,63) and (3,63) are switched around.

Orbital 1	Orbital 2	Contrib. (Unfitted)	Contrib. (Fitted)
1	64	3.866	5.342
3	62	1.519	1.590
4	63	1.364	1.374 (3,63)
4	62	1.133	0.954 (2,64)
3	63	1.042	0.953 (4,63)

Table 5.11: MBANP: Molecular-orbital-pair contributions to the polarisability

In order to aid comparison with experimental values, refractive indices were calculated from the aforementioned dipole polarisabilities taken from both the fitted and unfitted calculations. The experimental refractive indices measured at 532nm and 1064nm were taken from Bailey et al [84] and were extrapolated to zero frequency using the Sellmeier equations given by Kondo et al [85]. The room-temperature unit cell was taken from Kondo et al [77] and used to adjust the calcu-

	n_1	n_2	n_3
Exp. @ 532 nm	1.692	1.864	1.764
Exp. @ 1064 nm	1.620	1.725	1.690
Exp. Corrected	1.625	1.712	1.683
Unfitted	1.477	1.585	1.644
Fitted	1.494	1.602	1.658
Unfitted‡	1.461	1.563	1.620
Fitted‡	1.476	1.580	1.633

Table 5.12: MBANP: Refractive indices. ‡Adjusted for unit-cell volume at temperature of experimental values.

lated refractive indices to match the temperature at which the experimental refractive indices were recorded.

The wavefunction fitting does improve the agreement between the calculated and measured refractive indices but it is clear that both the unfitted and fitted results seem to underestimate them. Equally serious is the apparent mismatch in the relative magnitudes of the experimental and calculated indices. From the calculations, it is predicted that n_2 is less than n_3 but from the experimental values we observe that this relationship is reversed.

Both the full hyperpolarisability tensor and vector hyperpolarisability reported in Tables 5.13 and 5.14 respectively, show an increase in going from the ab-initio (unfitted) calculation to the wavefunction-fitted, which provides further support for the importance of including information on crystal effects, that is inherently contained in the X-ray diffraction data.

	Unfitted (CPHF)	Fitted (CPHF)
β_{xxx}	29.487	36.913
β_{xxy}	3.193	9.353
β_{xyy}	-81.851	-99.279
β_{yyy}	166.000	201.880
β_{xxz}	25.596	27.102
β_{xyz}	-82.287	-96.164
β_{yyz}	129.331	156.912
β_{xzz}	-50.674	-63.639
β_{yzz}	56.830	73.017
β_{zzz}	6.437	18.278

Table 5.13: MBANP: Dipole hyperpolarisability tensor components in $\times 10^{-52}$ C m^3 V^{-2}

	Unfitted (CPHF)	Fitted (CPHF)
β_x	-103.038	-126.006
β_y	226.022	284.250
β_z	161.365	202.292

Table 5.14: MBANP: Vector dipole hyperpolarisability in $\times 10^{-52}$ C m^3 V^{-2}

5.5 Constrained Wavefunction Fitting of PNP

Despite a good multipole refinement, significant problems were encountered with the constrained wavefunction calculation on PNP. A fitting calculation using exactly the same data included in the multipole refinement, failed to converge at a low λ value of 0.06. A comparison of the scattering plots showed the initial agreement between the calculation and experimental data was significantly worse than those seen for both DAN and MBANP, with a number of reflections exhibiting an F_z greater than 9, implying an initial difference between the calculated and experimental structure factors of 9 standard deviations.

Looking back at the scatter plots for DAN and MBANP, we see that apart from a limited number of outliers, all data are within $F_z = 5$. Taking this fact into consideration, it is was decided to apply a cut-off at an F_z of 5 to remove the worst-fitting data. The cut-off reduced the number of reflections used in the fitting procedure by only 175 which accounted for less than 2% of the total data and yet this cull was successful in achieving a complete constrained wavefunction calculation on PNP.

	Multipole	$\lambda = 0.000$	$\lambda = 0.435$
Total Energy(au)	-	-774.116873	-774.019202
χ^2	2.1468	2.653881	1.842980
$R(F)$	0.0197	0.023717	0.019790
$R_w(F)$	0.0226	0.027320	0.022767

Table 5.15: Fitting statistics for PNP

The full fitting statistics of the constrained wavefunction calculation for PNP on the reduced X-ray data set are reported in Table 5.15. In addition to the previously mentioned poorly fitting reflections, the plots of F_z vs $\sin\theta/\lambda$ and F_z vs F_{exp} (Figures 5.5(e) and (f)) both show a much greater spread of points about the line $F_z = 0$. This fact and the problems encountered with the fitting procedure perhaps suggest that the X-ray diffraction data obtained on PNP are of lower quality and might be indicative of a systematic anomaly in the data that the constrained wavefunction approach is unable to handle. These scatter plots do show that there is no trend

with resolution or intensity however.

The problems with fitting are further highlighted by the crystal error map (Figure 5.5(b)), which shows clearly numerous peaks of residual density. A careful examination of the map reveals that these peaks are sited on a 2-dimensional grid and are indicative of 2D series termination ripples (mentioned in Section 1.1.1). Such termination errors suggest that some of the low-order data is badly determined and as such seems to explain the poor fitting of PNP's X-ray data. The difference map (Figure 5.5(c)) however resembles very closely the maps obtained for DAN and MBANP with many of the same features also evident.

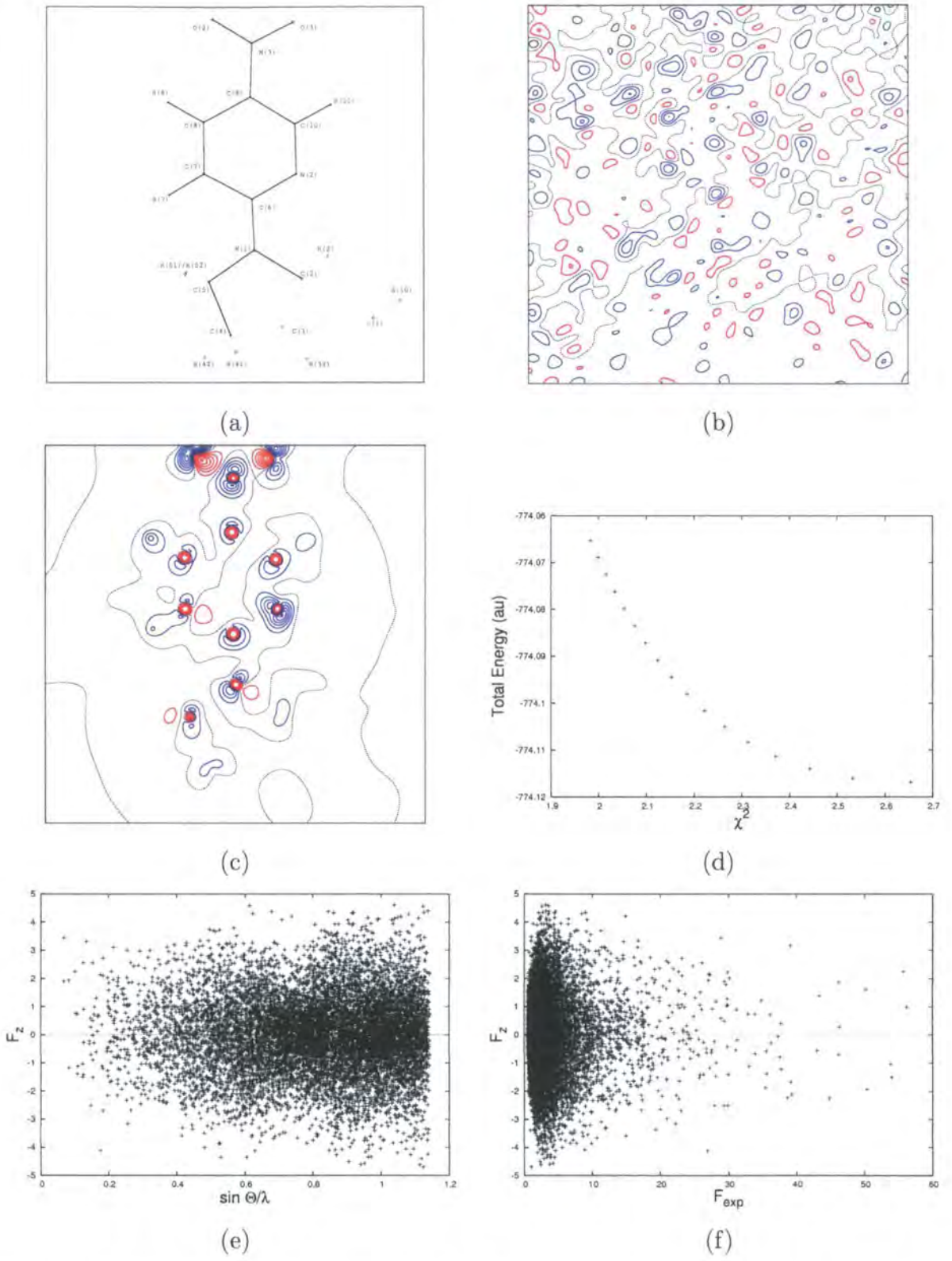

Figure 5.5: PNP: Details of the wavefunction fitting; (a) Atomic Labels (b) Crystal Error Map (c) Difference Density (d) Total Energy vs χ^2 (e) F_z vs $\sin\theta/\lambda$ (f) F_z vs F_o. Contours at intervals of 0.05eÅ^{-3}. Blue contours indicate positive regions and red indicate negative regions.

5.5.1 Properties of PNP

The effect of the constrained-wavefunction fitting on the dipole polarisability is again considered with the principal components reported in Table 5.16 and the full tensor given in Table 5.17. The directions of the principal components corresponds to the axes given relative to a PNP molecule in Figure 5.6. The same trend as for DAN and MBANP is again observed, that is an increase in the dipole polarisability as characterised by an increase of mean dipole polarisability $\overline{\alpha}$, from 22.263 to 23.119 in going from the ab-initio to the constrained-wavefunction description of PNP.

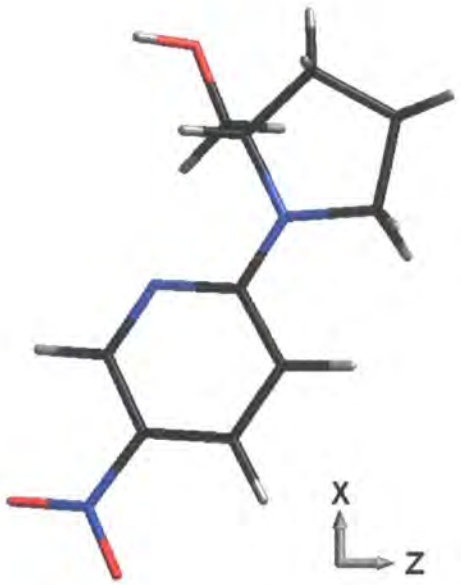

Figure 5.6: Principal axes of the polarisability with respect to the orientation of a PNP molecule; the y-axis is perpendicular to the page, defining a left-handed coordinate system.

	α_{xx}	α_{yy}	α_{zz}	$\overline{\alpha}$
Unfitted (CPHF)	12.713	21.859	32.219	22.263
Fitted (CPHF)	13.021	22.312	34.024	23.119

Table 5.16: PNP: Principle components of the dipole polarisability and mean polarisability in $\times 10^{-40}$ C m^2 V^{-1}

Like DAN, a molecule of PNP has 118 electrons resulting in 59 occupied molec-

	Unfitted (CPHF)	Fitted (CPHF)
α_{xx}	21.283	22.157
α_{xy}	-4.080	-4.533
α_{xz}	-8.103	-8.694
α_{yy}	25.000	25.752
α_{yz}	2.680	3.050
α_{zz}	20.507	21.449

Table 5.17: PNP: Dipole polarisability tensor components and mean polarisability in $\times 10^{-40}$ C m^2 V^{-1}

ular orbitals and 59 unoccupied molecular orbitals. The main contribution comes from the molecular-orbital pair (1,59) which is roughly six times larger than the next largest. In this case, we again observe that the 3rd and 5th largest contributions do not involve the same pairs of molecular orbitals after the fitting procedure has been applied.

Orbital 1	Orbital 2	Contrib. (Unfitted)	Contrib. (Fitted)
1	59	5.612	6.171
2	58	1.097	0.998
1	56	0.916	0.880 (1,55)
2	59	0.848	0.845
2	57	0.333	0.410 (4,59)

Table 5.18: PNP: Molecular-orbital-pair contributions to the polarisability

Experimental refractive indices for PNP were obtained from Sutter et al [86] and fitted to a single oscillator model in order to correct them for dispersion. In addition the calculated refractive indices were adjusted to account for the differing number density using the room-temperature cell constants obtained from Twieg et al [79]. The refractive indices obtained from fitting are closer to those obtained from experiment, however, in a similar way to the case of MBANP, they not only are noticeably smaller but also do not reflect the same relative magnitudes as are observed in all the experimental measurements.

	n_1	n_2	n_3
Exp. @ 488 nm	2.239(6)	1.929(5)	1.477(7)
Exp. @ 1064 nm	1.880(6)	1.732(5)	1.456(7)
Exp. Corrected	1.837	1.715	1.458
Unfitted	1.303	1.661	1.803
Fitted	1.312	1.686	1.861
Unfitted‡	1.295	1.639	1.775
Fitted‡	1.303	1.663	1.830

Table 5.19: PNP: Refractive indices. ‡Adjusted for unit-cell volume at temperature of experimental values.

Tables 5.20 and 5.21 show the full hyperpolarisability tensor and vector hyperpolarisability respectively. Wavefunction fitting has the effect of enhancing the calculated hyperpolarisability as was seen previously for both DAN and PNP.

	UnFitted (CPHF)	Fitted (CPHF)
β_{xxx}	96.492	117.428
β_{xxy}	-129.425	-151.729
β_{xyy}	82.416	99.917
β_{yyy}	-9.599	-25.108
β_{xxz}	-97.779	-118.361
β_{xyz}	120.823	142.328
β_{yyz}	-74.166	-90.438
β_{xzz}	80.778	98.816
β_{yzz}	-111.926	-130.984
β_{zzz}	-38.068	-52.924

Table 5.20: PNP: Dipole hyperpolarisability tensor components in $\times 10^{-52}$ C m^3 V^{-2}

	UnFitted (CPHF)	Fitted (CPHF)
β_x	259.686	316.161
β_y	-250.950	-307.820
β_z	-210.013	-262.723

Table 5.21: PNP: Vector dipole hyperpolarisability in $\times 10^{-52}$ C m^3 V^{-2}

5.6 Hyperpolarisabilities: Comparison with Experiment

The technique known as 'electric field-induced second-harmonic generation' (EFISH) [87] is the standard technique used to obtain experimental dipole hyperpolarisabilities. From EFISH experiments, the scalar quantity β_z is obtained, which is directly related to the components of the hyperpolarisability tensor by:

$$\beta_z = \beta_{zzz} + \beta_{xxz} + \beta_{yyz} \tag{5.4}$$

In a similar way to refractive indices, β_z is dependent on the wavelength of the measurement. A series of experimental measurements can therefore be extrapolated in order to determine a value at zero frequency β_0, a quantity which is commonly reported in the literature because it characterises the strength of the NLO response of molecules in a more reliable way [87].

In Table 5.22, experimental hyperpolarisabilities (β_z,β_0) are reported alongside values obtained from the constrained-wavefunction calculations for DAN, MBANP, PNP and MNA. Since the hyperpolarisabilities obtained from wavefunction fitting are inherently static, they have been denoted $\beta_{0,fit}$.

	DAN	MBANP	PNP	MNA
β_z	55[1]	63[3]	76[5],47[6]	69.9[8],39.8[9]
β_0	45[2]	30[4]	56[7]	33[10]
$\beta_{0,fit}$	31.6	20.2	26.2	19.1

Table 5.22: Comparison of hyperpolarisabilities from experiment (β_z,β_0) and wavefunction fitting ($\beta_{0,fit}$) for DAN, MBANP, PNP and MNA in $\times 10^{-51}$ C m^3 V^{-2}. All experimental values measured in 1,4-dioxane. [1]Measured at 1907nm [88]. [2]Ref. [88]. [3]Measured at 1064nm [78]. [4]Ref. [78]. [5]Measured at 1064nm [89]. [6]Measured at 1907nm [79]. [7]Ref. [89]. [8]Measured at 1064nm [90]. [9]Measured at 1907nm [90]. [10]Ref. [90]

Despite accounting for dispersion, the calculated hyperpolarisabilities are much smaller than the frequency-independent experimental values for all of the compounds

considered. It is important to realise however that both β_z and β_0 are strongly dependent on the solvent used in the EFISH measurements. This may in part explain why the wavefunction-fitted results seem to underestimate the experimental values though there is still the concern that the experimental values suggest that PNP has the largest NLO response while the constrained wavefunction results estimate DAN to have the greater response.

5.7 Conclusions

The results of constrained-wavefunction-fitting calculations were reported on three materials (DAN, MBANP and PNP) and the effects of the fitting on the derived optical properties and electron density were discussed.

From the relatively featureless crystal-error maps, we can be confident that the fitting procedure has accounted for the majority of the experimental electron density. The difference maps offer a striking view of the effect of fitting with the largest changes occuring at the cores of the atoms, indicated by a charge depletion in going from the unfitted to the fitted wavefunctions. Other signifcant deformations between the unfitted and fitted calculations were located around the oxygen atoms of the nitro groups. This is more expected and can be attributed to a deformation of the oxygen lone pairs due to the crystal field. In general, one would expect that features in the difference density should be attributable to perturbations of the electron density by the crystal field. Why there should be changes in the core when one includes experimental crystal data is unclear from the evidence presented thus far, but this issue is addressed in the following chapter in which these constrained-wavefunction calculations are compared with results obtained from multipole refinements of X-ray diffraction data.

In all cases we observe only a relatively small increase in the dipole polarisability calculated from the constrained wavefunction when compared to the unfitted ab-initio calculations. This may be predicted, based on the evidence of the difference maps, which suggests that wavefunction fitting mostly affects the tightly held core electrons that are not the most important contributors to the dipole polarisability.

The refractive indices calculated from the fitted polarisabilities are closer to the experimental values than those from the unfitted calculations but the improvement is neglible when compared with the disparity between any of the calculated and experimental values. In the cases of MBANP and PNP even the relative magnitudes are seemingly not reproduced correctly. Assuming no mistakes have been made in the implementation of the refractive index code, we must consider that inaccurate estimates for the dipole polarisabilities are obtained as the result of some unfavorable feature of the fitting process.

For each of the three compounds, significant increases in the dipole hyperpolarisabilities were observed after wavefunction fitting, which in a similar manner to the dipole polarisabilities, can be attributed to the effects of the crystal field and intermolecular interactions introduced by way of fitting to the X-ray diffraction data. In a comparison with hyperpolarisabilities obtained from EFISH experiments, the values obtained from wavefunction fitting were pleasingly comparable in magnitude. The underestimation of the fitted hyperpolarisabilities was expected since the solvent used in the measurement of the experimental values is known have a large influence. However, until we are confident in our ability to obtain accurate *linear* optical properties, any properties dependent on second-order effects should be treated with a degree of caution.

The use of constrained-wavefunction calculations in order to obtain accurate and reliable estimates of both the linear and non-linear optical properties has met with limited success at the present time. Clearly this technique however shows promise and so in the following chapter we consider further the nature of these 'experimental' wavefunctions by comparing them with multipole refinements of X-ray diffraction data.

Chapter 6

Wavefunction-Fitting Calculations and Charge Density: A Detailed Comparison

6.1 Introduction

The multipole model is a well-established technique for analysing high-resolution X-ray diffraction experiments in order to obtain the one-electron density. An alternative approach is the use of X-ray constrained wavefunctions to obtain the density matrix. Both of these methods therefore provide the means of obtaining the electron distribution in the solid state along with one-electron properties of in-crystal fragments or molecules. However access to the density matrix has advantages over the multipole model because it allows for the calculation of other properties, for example kinetic-energy densities.

Since there is a broad common basis of quantities that can be determined by both methods it seems pertinent to perform a detailed comparison of the two methods especially since only one such comparison has been performed to date on ammonia [91]. This study was rather limited in its scope, looking only at a small number of parameters obtained from a topological analysis of the charge density from constrained-wavefunction fitting and multipole refinement of X-ray diffraction data. The study found that the constrained wavefunction gave densities at the bond

critical points slightly larger, though in general agreement, with those obtained from multipole refinement of X-ray data and similar integrated atomic charges. However it is still not completely clear what insights the constrained wavefunction calculations give and what the limitations of these "experimental" wavefunction are. The comparison will be especially interesting because both methods are based on exactly the same experimental data albeit used in different ways.

In this chapter, the cases of DAN, MBANP and PNP are again considered with the constrained-wavefunction calculations used in the comparison taken from the work discussed in the previous chapter. For each material, further details are reported on the multipole refinements since at this time these have not been published elsewhere.

From the multipole model and experimental wavefunction, the following maps are reported for each of the three compounds: the deformation density, the negative Laplacian of the electron density, the electron localisation function (ELF) and the electrostatic potential. In addition electrostatic properties, namely the partial atomic charges and molecular dipole moments are reported to provide a more quantitative view of these materials. Together these quantities provide a comprehensive characterisation of these materials electronically and provide a sound basis for understanding what is obtained from this constrained-wavefunction fitting approach.

6.2 Comparison of DAN

Table 6.1 summarises the pertinent crystallographic details for the charge-density study of DAN. The multipole refinement was carried out with XD [16] on F^2. The criteria for including reflections in refinement was discussed previously (See Table D.2). The atomic positions and associated ADPs were refined for all atoms except the hydrogen atoms, whose positions and U_{iso} were fixed to the values obtained from the IAM refinement. Constraints were applied to all bonds involving hydrogen atoms (N–H 1.01, C_{aryl}–H 1.08 and C_{alkyl}–H 1.06). Since DAN crystallises in the polar spacegroup $P2_1$, it was necessary to fix the y-coordinate of O(1) in the refinement.

Monopoles were refined for all atoms except O(1). Dipoles, quadrupoles and

Empirical Formula	$C_{10}H_{13}N_3O_3$
Formula Weight (g mol^{-1})	223.23
Crystal System	Monoclinic
Space Group	$P2_1$
Z	2
$F(000)$	118
Crystal Size (mm^3)	$0.34 \times 0.12 \times 0.05$
Crystal form, Colour	prism, yellow
Diffractometer	Bruker SMART 6000
Temperature (K)	120
Wavelength λ (Å)	0.71073
a (Å)	4.7874(1)
b (Å)	12.7960(2)
c (Å)	8.6234(2)
β (°)	95.341(1)
V (Å^{-3})	525.86(3)
μ (mm^{-1})	0.11
$(\sin\theta/\lambda)_{max}$ (Å^{-1})	1.14375
Completeness (%)	100
R_{int}	0.0297
N_{uniq}	10099
N_{ref}	6732
$R_{1,all}(F)$	0.0376
$R_{1,ref}(F)$	0.0213
$R_{w,ref}(F)$	0.0224
N_{ref}/N_v	> 16

Table 6.1: Details of the Charge-Density Experiment on DAN

octupoles were refined for all non-hydrogen atoms, though the aromatic carbons were treated specially. For these the dipole, d_{11+}, the quadrupoles, d_{21-}, d_{21+}, and

the octupoles d_{30}, d_{32-} and d_{32+} were not refined[1]. For the hydrogen atoms, both the bond-directed dipole and the quadrupole d_{20} again, directed along the bond, were refined. κ and κ' parameters were refined for all non-hydrogen atoms (one for each element), but separate parameters were used for the nitrogen atoms in the nitro and amine groups.

6.2.1 Results

Figure 6.2.1 shows the deformation density and negative of the Laplacian calculated from the multipole model (a) and the constrained wavefunction (b). One of the curious features of the deformation density maps obtained from the fitted wavefunction are large 'spikes' centred on the atomic positions. In order to prevent these features dominating the deformation density map, a truncation was applied to the map. Apart from this feature, both maps show clearly the deformations consistent with what is expected for all the functional groups present.

As is typical for Laplacian plots, a logarithmic scale was chosen with contours at intervals of $\pm 2^n$ eÅ^{-5}, where $n \geq 0$. Blue contours indicate regions of charge concentration and red contours indicate regions of charge depletion. Both the charge-density and constrained wavefunction maps show the features one would expect to find in the negative laplacian, whose most obvious feature is the charge concentration in the bonds between atoms. Other features of note include the lone pairs on the oxygen atoms of the nitro substituent and the core structures of the C, N and O atoms.

Figure 6.2.1 shows the electron localisation function (ELF) and the electrostatic potential of DAN from the multipole model (a) and the constrained wavefunction (b). The ELF is a representation of the organisation of chemical bonding in direct space and takes values in the range 0 to 1, with a value of 1 implying perfect localisation. Regions of high electron localisation are called attractors which are typical of bonds, lone pairs and atomic shells. At first, the ELFs determined from the charge density refinement and the constrained wavefunction calculation look

[1]The Z-axis of the multipole is perpendicular to the plane of the ring

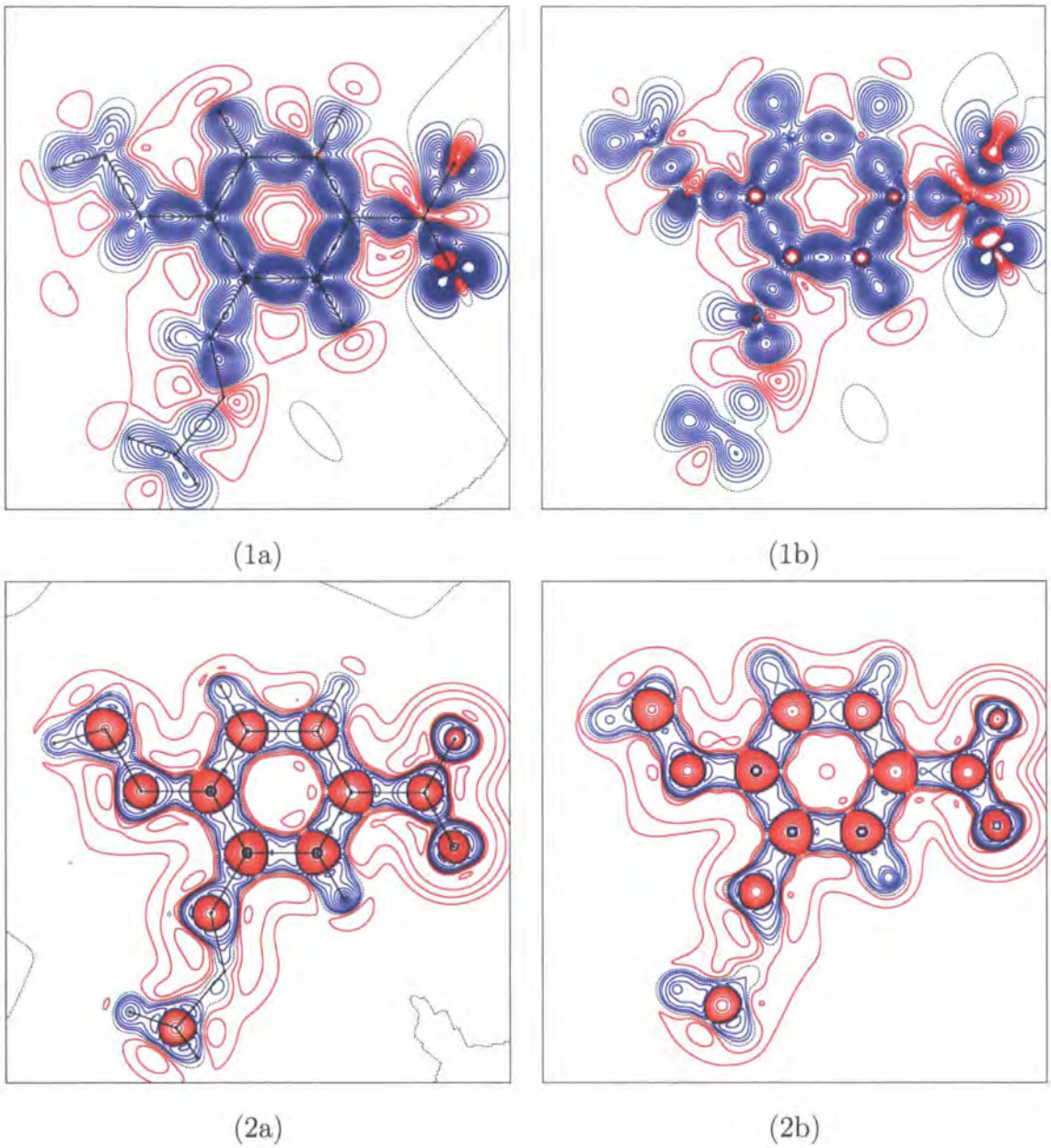

Figure 6.1: Deformation density of DAN from (1a) Multipole (1b) Wavefunction fitting. Contours at intervals of 0.05eÅ^{-3}. Negative Laplacian of the electron density of DAN from (2a) Multipole (2b) Wavefunction fitting. Contours at intervals of $\pm 2^n$ eÅ^{-5}, where $n \geq 0$. Blue contours indicate positive regions and red indicate negative regions.

surprisingly different. However both clearly show features attributable to the atomic shells, bonds and lone pairs and it is only as we get further away from the atoms do the features diverge from their similarity. The electrostatic potential maps on

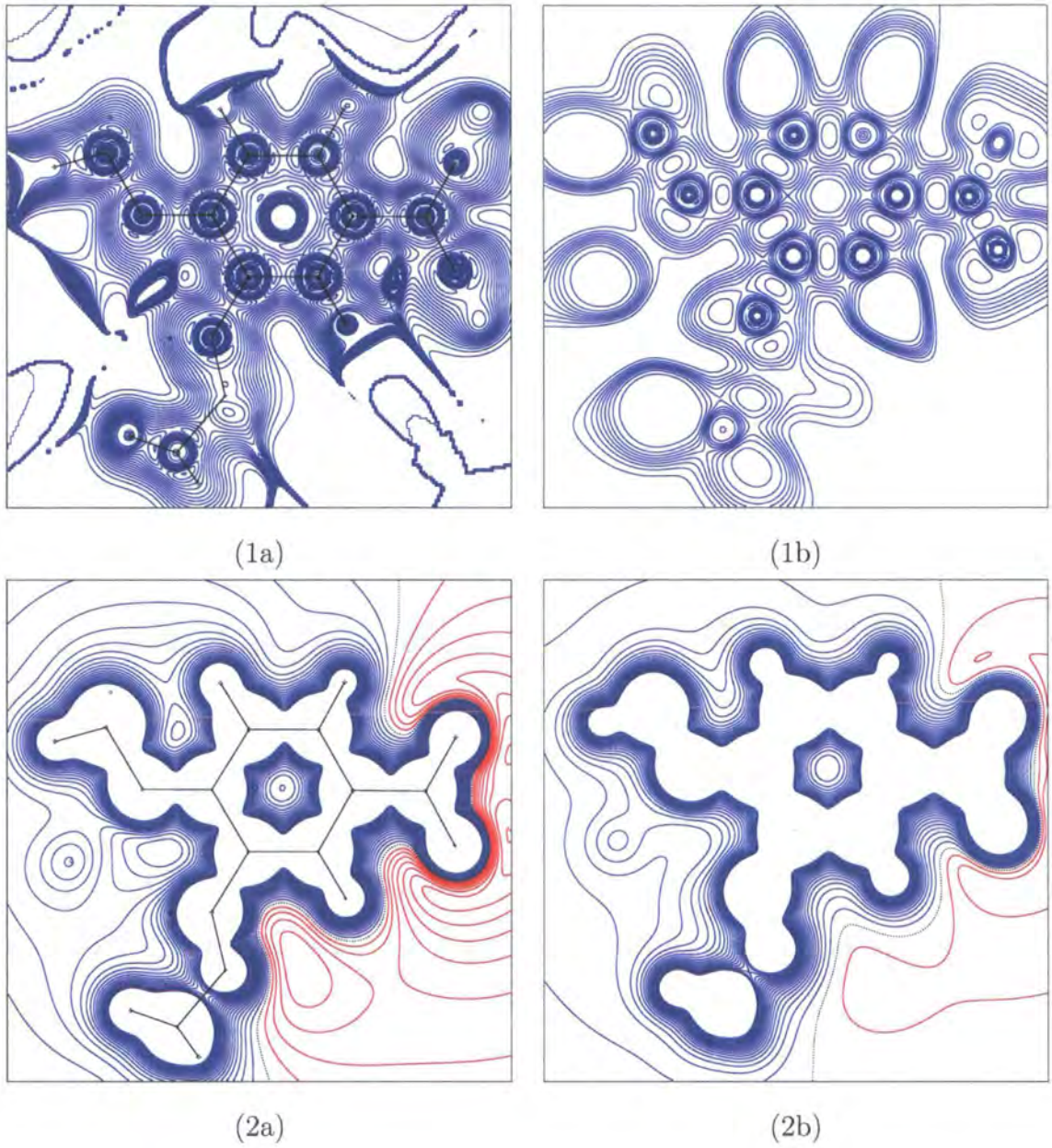

Figure 6.2: Electron localisation function of DAN from (1a) Multipole (1b) Wavefunction fitting. Electrostatic Potential of DAN from (2a) Multipole (2b) Wavefunction fitting. Contours at intervals of 0.05, using the same contour conventions as Figure 6.2.1

the other hand are extremely similar in their gross features, with only the charge density results predicting that the molecule is much more polar (indicated by the greater number of contours surrounding the nitro group).

Other electrostatic properties of interest are the partial atomic charges and the

	Multipole	Fitted		Multipole	Fitted
O(1)	-0.4021	-0.277314	H(3N)	0.2683	0.196157
O(2)	-0.3960	-0.328454	H(2)	0.2775	0.161939
O(3)	-0.4440	-0.405134	H(5)	0.0806	0.079200
N(1)	-0.0878	0.226953	H(6)	0.2933	0.169866
N(2)	-0.3764	-0.368415	H(71)	0.2626	0.183218
N(3)	-0.2280	-0.318989	H(72)	-0.0575	0.044696
C(1)	0.2277	0.138313	H(73)	-0.0972	0.057614
C(2)	-0.0730	0.066462	H(81)	0.1852	0.137880
C(3)	-0.0273	-0.053849	H(82)	0.1903	0.108646
C(4)	-0.0386	0.097037	H(83)	0.0442	0.084970
C(5)	0.0435	-0.066908	H(101)	0.0178	0.153384
C(6)	-0.2606	-0.097421	H(102)	0.3127	0.190210
C(7)	0.1770	-0.089759	H(103)	0.1161	0.142803
C(8)	0.0479	-0.122295			
C(9)	-0.0497	0.333728			
C(10)	-0.0072	-0.444539			

Table 6.2: Partial atomic charges for DAN

molecular dipole moment, which are reported in Table 6.2 and 6.3 respectively. The multipole model in general exhibits slightly more negative charges for non-hydrogen atoms and slightly more positive charges for the hydrogen atoms themselves. In fact the differences between the multipole model and constrained wavefunction are even more apparent when one considers that there are a number of changes of sign of the partial charges for N(1) and a number of carbons atoms. Most disturbingly, the multipole model determines that two methyl hydrogens H(72) and H(73) carry a negative charge which one would not expect to see based on an electronegativity argument for that functional group.

From such large differences in the partial charges, it is perhaps not surprising that there is also a large discrepancy between the predicted dipole moments for

DAN. Given that a dipole moment of 8.1D[2] was reported by Baumert et al [76], this would imply a considerable dipole moment enhancement of 20.5D in going from the solution to the solid state for the case of the multipole refinement, whereas the fitted wavefunction implies a more reasonable enhancement of 2.9D.

	Multipole	Fitted	$\|\Delta\|$
μ_x	21.1(14)	8.790923	12.3
μ_y	9.4(17)	3.012538	6.4
μ_z	-16.9(23)	-5.915849	11.0
$\|\mu\|$	28.6(18)	11.016033	17.6

Table 6.3: Comparison of the molecular dipole moments for DAN (Debyes)

6.3 Comparison of MBANP

Table 6.4 summarises the crystallographic details of the charge-density analysis of MBANP. The multipole refinement was carried out with XD on F^2. The default filtering criteria were used to select reflections for inclusion in refinement. Atomic positions and ADPs were refined for all atoms except the hydrogen atoms, whose positions and U_{iso} were fixed from the IAM refinement. In addition, all X–H bond were constrained to values taken from the neutron structure determination of MBANP [92]. Again, MBANP crystallises in the polar spacegroup $P2_1$ requiring the y coordinate of O(1) to be fixed in the refinement.

Monopoles, dipoles, quadrupoles and octupoles were refined for all non-hydrogen atoms. For hydrogen the monopoles, bond-directed dipole and the quadrupole d_{20} again directed along the bond, were refined. However the aromatic carbons were treated slightly differently to all the other carbon atoms. For these the dipole, d_{11+}, the quadrupoles, d_{21-}, d_{21+}, and the octupoles d_{30}, d_{32-} and d_{32+} were not refined[3]. For the hydrogen atoms, both the bond-directed dipole and the quadrupole d_{20}, again directed along the bond, was refined.

[2]Solution phase measurement with dioxane as the solvent.

[3]The Z-axis of the multipole is perpendicular to the plane of the ring

Empirical Formula	$C_{13}H_{13}N_3O_2$
Formula Weight (g mol^{-1})	243.26
Crystal System	Monoclinic
Space Group	$P2_1$
Z	2
$F(000)$	128
Crystal Size (mm^3)	0.30 × 0.18 × 0.18
Crystal form, Colour	prism, light-yellow
Diffractometer	Bruker SMART 6000
Temperature (K)	120
Wavelength λ (Å)	0.71073
a (Å)	5.3360(2)
b (Å)	6.3191(2)
c (Å)	17.7417(2)
β (°)	93.789(1)
V (Å^{-3})	596.93(5)
μ (mm^{-1})	0.09
$(\sin\theta/\lambda)_{max}$ (Å^{-1})	1.14427
Completeness (%)	99.9
R_{int}	0.0201
N_{uniq}	12900
N_{ref}	8785
$R_{1,all}(F)$	0.0413
$R_{1,ref}(F)$	0.0216
$R_{w,ref}(F)$	0.0193
N_{ref}/N_v	> 19

Table 6.4: Details of the Charge-Density Experiment on MBANP

6.3.1 Results

The deformation density and negative of the Laplacian for the compound MBANP are shown in Figure 6.3.1. The deformation-density maps show a high degree of sim-

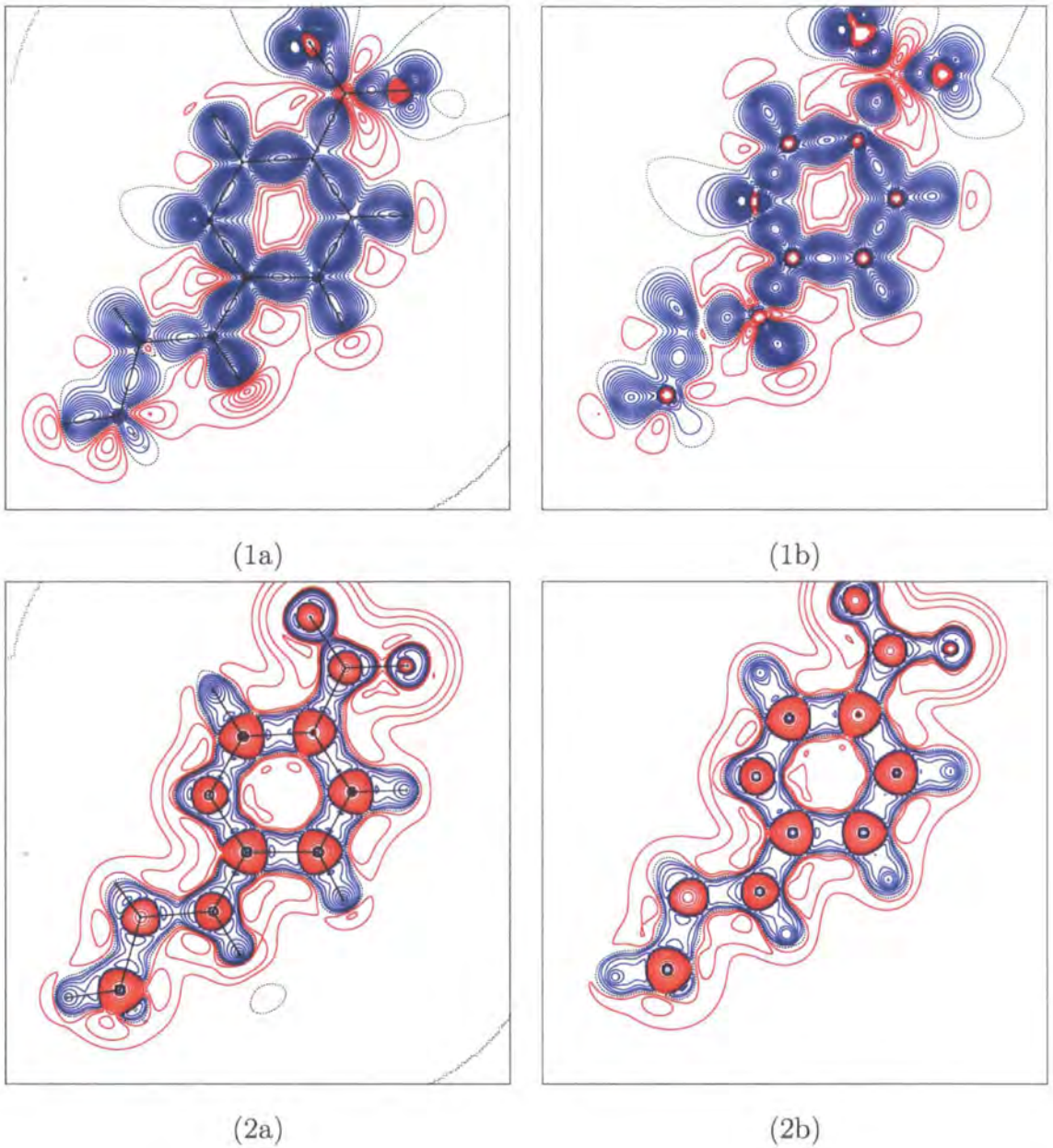

Figure 6.3: Deformation density of MBANP from (1a) Multipole (1b) Wavefunction fitting. Negative Laplacian of MBANP from (2a) Multipole (2b) Wavefunction fitting. Same contour conventions and intervals used as Figure 6.2.1

iliarity with the largest deformations occuring between the bonds as expected. As in the case of DAN, large spikes corresponding to a significant core deformations at the atomic centres was observed with the constrained-wavefunction result. The strong resemblance of the deformation-density maps obtained from the two methods is also reflected in the negative of the Laplacians which show the charge concentrations as-

sociated with the covalent bonds and lone pairs present. A closer examination reveals that the lone pairs of the oxygen atoms in the nitro group are more pronounced in the charge-density result, whereas there appears to be more charge concentrated in the corresponding N–O bonds in the constrained-wavefunction result. This suggests less of a molecular polarisation in the constrained-wavefunction model of MBANP which was also observed in the case of DAN discussed above.

Figure 6.3.1 shows the electron-localisation function and electrostatic-potential maps calculated for MBANP. Interestingly, there appears to be more significant differences observed in the ELF map for the two methods, than is seen for either of the deformation density or Laplacian maps. These are more conspicuous around the periphery of the molecule, particularly in the localisation descriptions of the hydrogen atoms. Also in the constrained-wavefunction ELF, there also appears to be more 'structure' in the interatomic regions and especially in the centre of the phenyl ring when compared to that of the charge-density ELF map. Furthermore, the lone pairs are much less pronounced in the charge-density map than in the corresponding one obtained from the constrained wavefunction.

Both electrostatic-potential maps show that the greatest regions of negative electrostatic potential, lie in the vicinity of the nitro group and around the nitrogen atom of the pyridine group, which is exactly what is expected given the availability of lone pairs on these substituents. Unlike DAN, both the charge-density results and the constrained-wavefunction results, predict electrostatic potentals of a similar magnitude though in the former case the region of electrostatic potential forms a single 'envelope'.

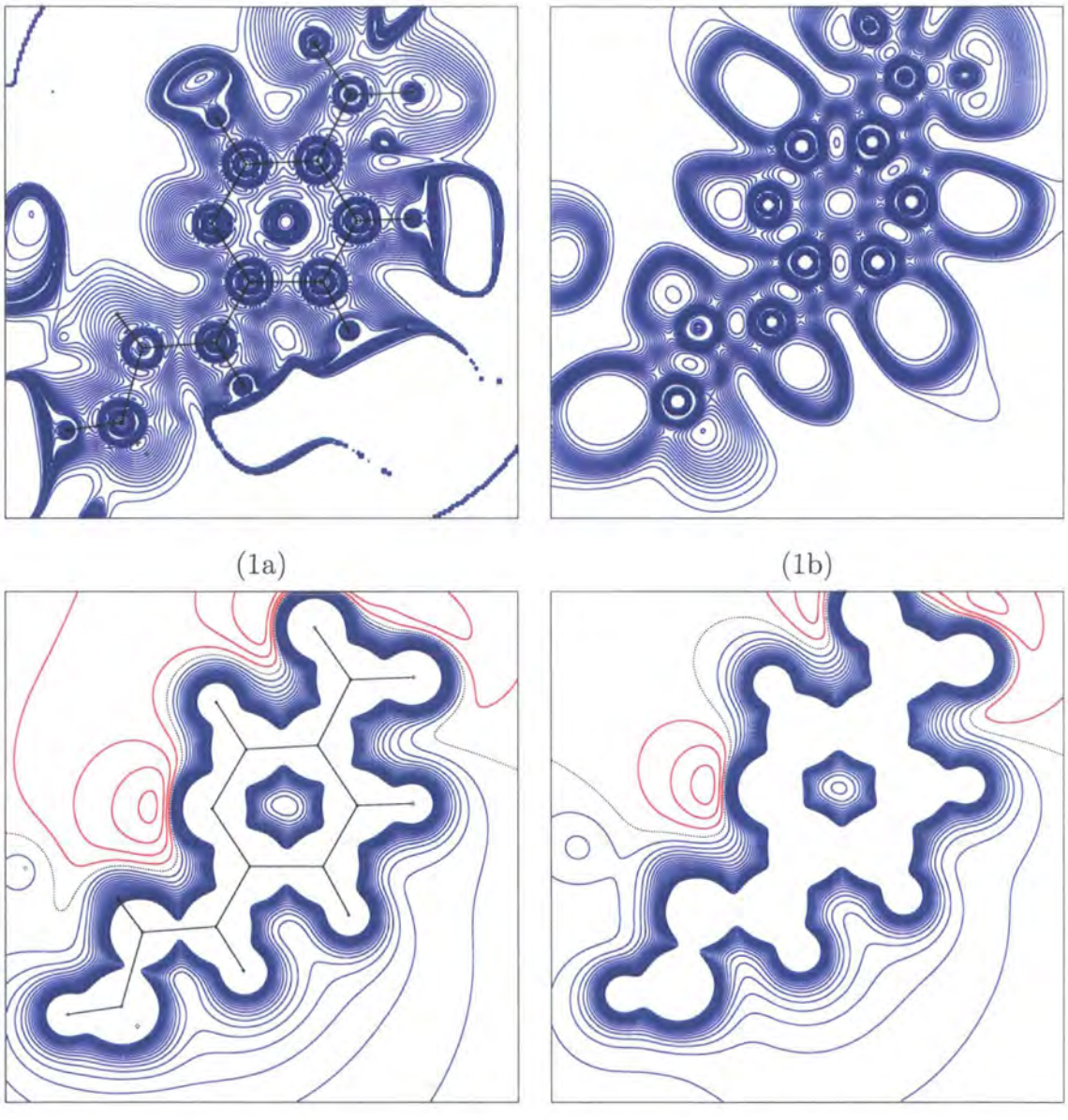

(1a) (1b)

(2a) (2b)

Figure 6.4: Electron Localisation Function (ELF) of MBANP from (1a) Multipole (1b) Wavefunction fitting. Electrostatic Potential of MBANP from (2a) Multipole (2b) Wavefunction fitting. Contours at intervals of 0.05, using the same contour conventions as Figure 6.2.1

	Multipole	Fitted		Multipole	Fitted
O(1)	-0.2489	-0.235914	C(11)	-0.0938	-0.184691
O(2)	-0.1182	-0.265750	C(12)	-0.0754	0.021187
N(1)	-0.0635	-0.249938	C(13)	-0.0938	-0.192819
N(2)	0.0515	0.133142	C(14)	-0.2455	-0.077821
N(3)	-0.1009	-0.263376	H(3N)	0.1616	0.206264
C(2)	0.0491	0.218255	H(3)	0.1429	0.123931
C(3)	-0.1454	-0.136248	H(4)	0.1196	0.137298
C(4)	-0.0601	-0.030164	H(6)	0.1100	0.136823
C(5)	-0.0086	-0.021905	H(7)	0.1612	0.109145
C(6)	-0.0287	0.094677	H(81)	0.2883	0.146897
C(7)	-0.1233	-0.026972	H(82)	0.2059	0.196805
C(8)	-0.2595	-0.332393	H(83)	0.0370	0.093659
C(9)	-0.1542	-0.116807	H(10)	0.1551	0.153189
C(10)	-0.2455	-0.105843	H(11)	0.1770	0.132889
H(12)	0.1099	0.114754			

Table 6.5: Partial atomic charges for MBANP

In Tables 6.5 and 6.6 the partial atomic charges and molecular dipole moments from both methods are reported. Unlike for DAN, the partial atomic charges are much more consistent between the charge-density and constrained-wavefunction results but still display notable disparities, for example N(1) has a charge of -0.0635 from the charge density versus -0.2658 from the experimental wavefunction. Only two atoms C(6) and C(12) show contrary signs of the charges. The overall dipole moments determined are also predicted to be much closer with the multipole model estimating a dipole moment of 12.5D and the constrained wavefunction gives a value of 8.75D, which are both feasible enhancements compared to a reported experimental value of 6.07D in dioxane [78].

	Multipole	Fitted	$\|\Delta\|$
μ_x	-7.8(5)	-5.793291	2.0
μ_y	9.7(14)	6.166806	3.5
μ_z	1.6(18)	2.193530	0.6
$\|\mu\|$	12.5(11)	8.740898	3.8

Table 6.6: Comparison of the molecular dipole Moment for MBANP (Debyes)

6.4 Comparison of PNP

The relevant crystallographic details for the charge-density study of PNP are reported in Table 6.7. A multipole refinement was carried out with XD on F^2 using the default criteria for including reflections in the refinement. The atomic positional parameters and ADPs were refined for all atoms except the hydrogen atoms, whose positions and U_{iso} were fixed from the IAM refinement. Constraints based on the neutron-derived bond lengths, were applied to all bonds involving hydrogen atoms (O–H 0.96, C_{aryl}–H 1.08 and C_{alkyl}–H 1.06 and $C_{tertiary}$–H 1.10). The y coordinate of O(1) was fixed in the refinement because PNP crystallises in the polar spacegroup $P2_1$.

Monopoles, dipoles, quadrupoles and octupoles were refined for all non-hydrogen atoms, however the aromatic carbon atoms and pyridine nitrogen atom were treated specially. For these the dipole, d_{11+}, the quadrupoles, d_{21-}, d_{21+}, and the octupoles d_{30}, d_{32-} and d_{32+} were not refined[4]. For the hydrogen atoms, both the bond-directed dipole and the quadrupole d_{20} again directed along the bond were refined. Kappa parameters were refined for all non-hydrogen atoms for each element.

6.4.1 Results

Figure 6.4.1 shows the calculated deformation-density maps and negative of the Laplacian for PNP, both of which share the same main features consistent with the functional groups present in PNP, for example, the prominent lone pairs on the

[4]The Z-axis of the multipole is perpendicular to the plane of the ring

Empirical Formula	$C_{10}H_{13}N_3O_3$
Formula Weight (g mol^{-1})	223.23
Crystal System	Monoclinic
Space Group	$P2_1$
Z	2
$F(000)$	118
Crystal Size (mm^3)	$0.31 \times 0.20 \times 0.16$
Crystal form, Colour	prism, light-yello
Diffractometer	Bruker SMART 6000
Temperature (K)	120
Wavelength λ (Å)	0.71073
a (Å)	5.1130(1)
b (Å)	14.8961(3)
c (Å)	7.0185(1)
β (°)	107.646(1)
V (Å^{-3})	509.41(2)
μ (mm^{-1})	0.10
$(\sin\theta/\lambda)_{max}$ (Å^{-1})	1.14245
Completeness (%)	100
R_{int}	0.0143
N_{uniq}	10739
N_{ref}	8770
$R_{1,all}(F)$	0.0241
$R_{1,ref}(F)$	0.0197
$R_{w,ref}(F)$	0.0226
N_{ref}/N_v	> 21

Table 6.7: Details of the Charge-Density Experiment on PNP

oxygens atoms and the nitrogen of the pyridine group. The same core features as for DAN and MBANP are also observed in the deformation density obtained from the constrained wavefunction for PNP.

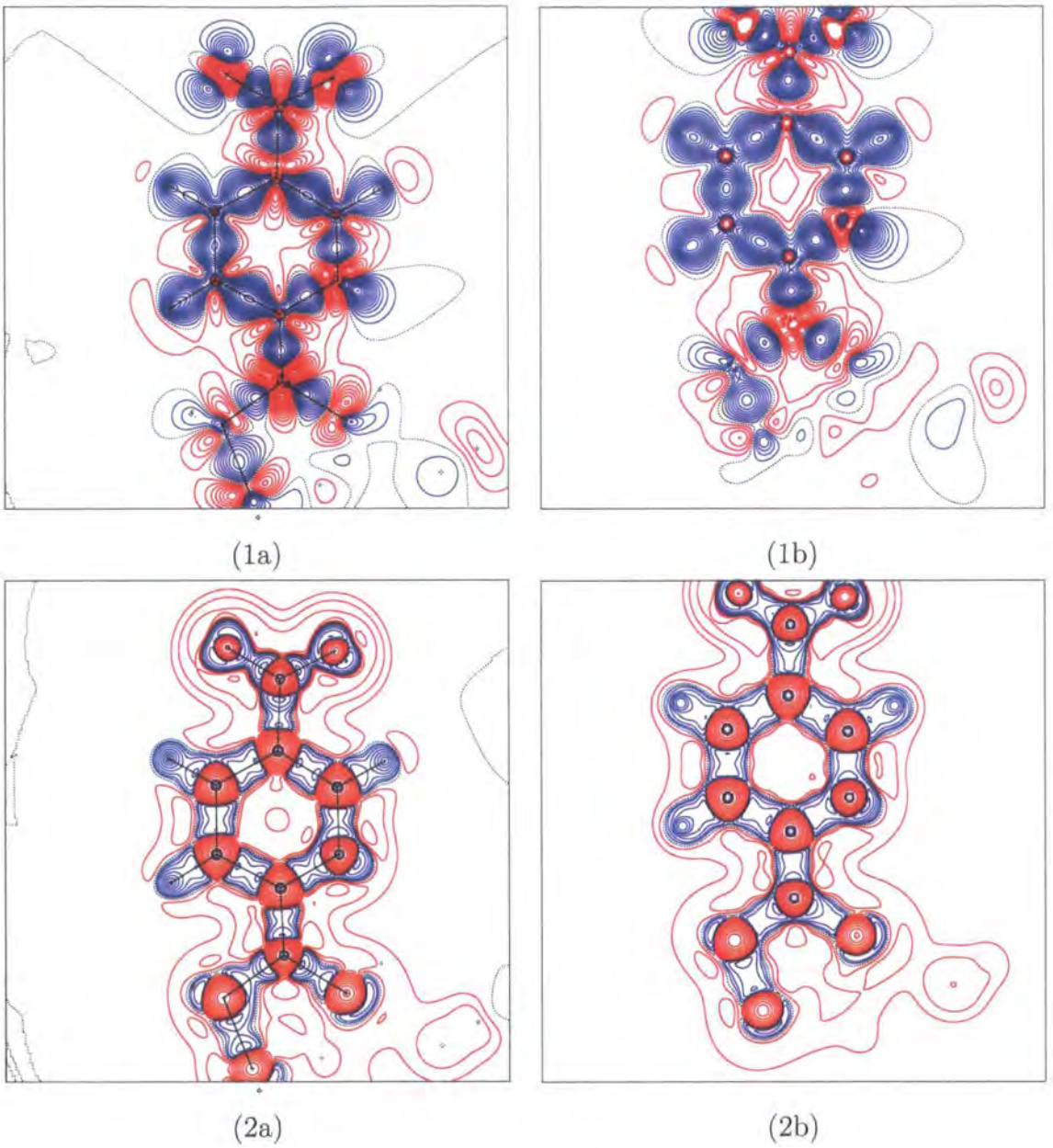

Figure 6.5: Deformation Density of PNP from (1a) Multipole (1b) Wavefunction fitting. Negative Laplacian of PNP from (2a) Multipole (2b) Wavefunction fitting. Same contour conventions and intervals used as Figure 6.2.1

The ELF and electrostatic-potential maps of PNP are shown in Figure 6.4.1. The differences observed in the ELF map of PNP are almost identical to those seen in those maps generated for DAN and MBANP, with the most conspicuous features being found around the edge of each molecule. In particular the sharp features extending out from the molecule observed in the ELF of all three compounds seen

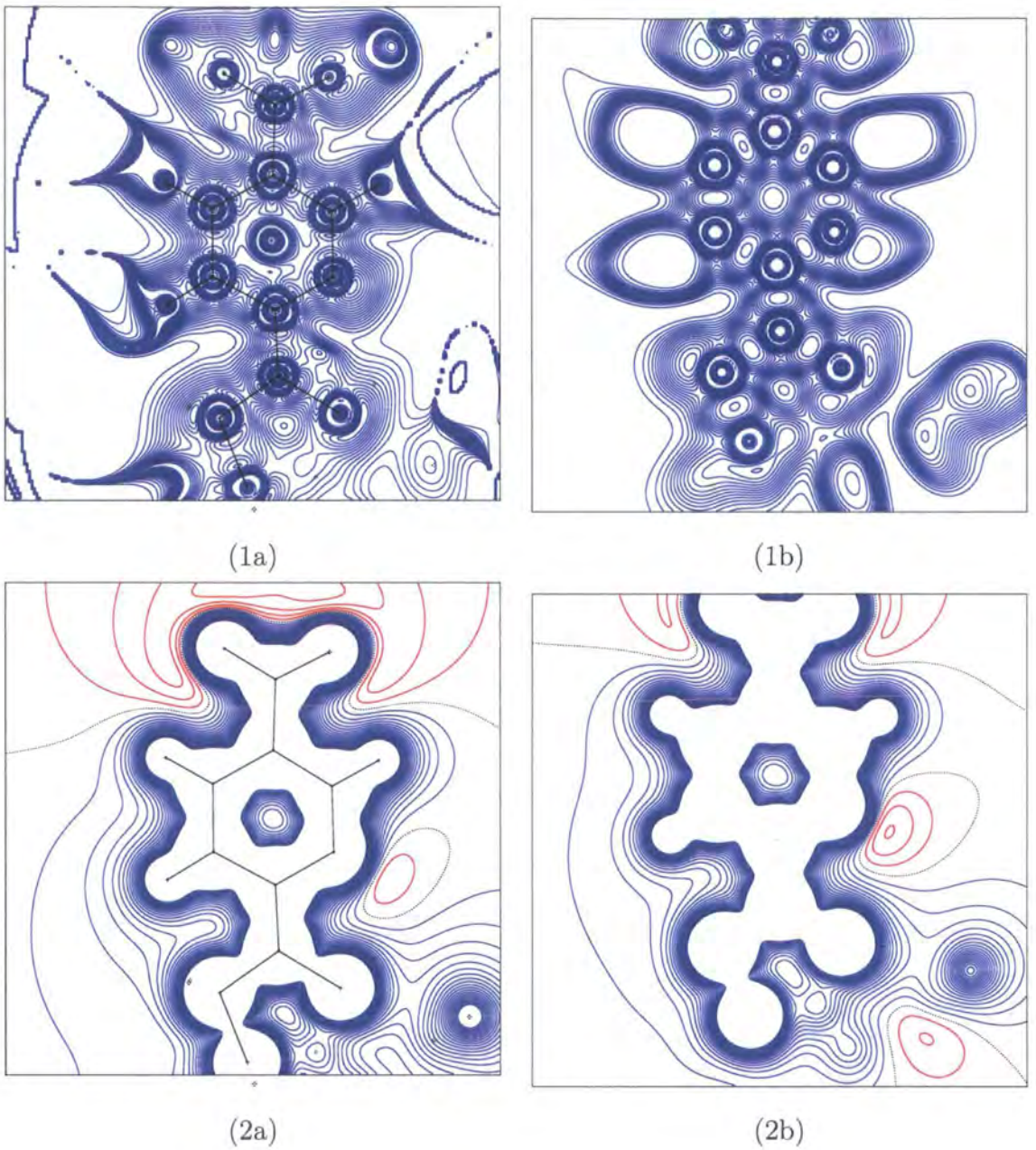

Figure 6.6: Electron Localisation Function (ELF) of PNP from (1a) Multipole (1b) Wavefunction fitting. Electrostatic Potential of PNP from (2a) Multipole (2b) Wavefunction fitting. Contours at intervals of 0.05, usig the same contour conventions as Figure 6.2.1

in the maps taken from the multipole models, seem to offer no reasonable physical interpretation, since one does not expect to find any significant electron density in this region whether localised or not.

The electrostatic-potential map from multipole refinement suggests that PNP is more polarised towards the nitro group than in the constrained-wavefunction case, which in fact shows three regions of negative electrostatic potential associated with the nitro group, the nitrogen atom of the pyridine ring and with the (out-of-plane) prolinol substituent.

	Multipole	Fitted		Multipole	Fitted
O(1)	0.1249	-0.379471	C(9)	0.0756	-0.058361
O(2)	-0.2771	-0.341903	C(10)	-0.0924	0.255200
O(3)	-0.2440	-0.351849	H(1O)	0.1339	0.201061
N(1)	-0.2144	-0.548806	H(11)	0.0988	0.047594
N(2)	-0.0865	-0.464258	H(12)	0.1220	0.091527
N(3)	0.0144	0.304262	H(2)	0.0877	0.073741
C(1)	-0.1616	0.176328	H(31)	0.1312	0.058902
C(2)	-0.1012	-0.011017	H(32)	0.0212	0.052915
C(3)	-0.2361	-0.069558	H(41)	0.1579	0.064934
C(4)	-0.1546	-0.076859	H(42)	0.0853	0.070505
C(5)	-0.0704	0.075011	H(51)	0.0692	0.100766
C(6)	0.0670	0.538687	H(52)	0.1013	0.061583
C(7)	0.0088	-0.231501	H(7)	0.1593	0.074559
C(8)	-0.2014	0.029193	H(8)	0.1821	0.140585
H(10)	0.1986	0.116229			

Table 6.8: Partial Atomic Charges for PNP

As expected, the clear differences in the electrostatic potential are reflected in the partial atomic charges and dipole moment, which are given in Tables 6.8 and 6.9 respectively. Both the charges and the components of the dipole moment display substantial differences between the two methods, resulting in an overall dipole difference of some 7.6D. As was seen for the cases of DAN and MBANP, it is the multipole model which again estimates a much larger dipole moment in the solid state.

	Multipole	Fitted	$\|\Delta\|$
μ_x	8.7(17)	4.430994	4.3
μ_y	-8.2(22)	-1.905434	6.3
μ_z	-7.9(18)	-4.680572	3.2
$\|\mu\|$	14.3(19)	6.721022	7.6

Table 6.9: Comparison of the molecular dipole moment for PNP (Debyes)

6.5 Conclusions

In this chapter, various maps and electrostatic properties of previous charge-density studies were compared with ones obtained by fitting a wavefunction to the same charge-density data. A visual comparison of the deformation and Laplacian maps show almost identical gross features indicating that both the charge density and fitting provides similar descriptions of the charge density and bonding. Many of the small differences can be explained when one considers that the planes of the maps taken from the multipole refinement and the fitted calculation are not identical as a consequence of the differences in how the programs allow the user to define the plane of the maps. However, we do see some clear differences in the core descriptions in the deformation maps, with constrained-wavefunction models exhibiting a large depletion of charge with respect to the promolecule density suggesting that the core density has changed considerably in the fitting procedure. Since these core deformations are neither seen in the charge-density study nor in results obtained from ab-initio calculations, that is to say, only appear once the wavefunction fitting has been applied, this might suggest that some unfavorable systematic effect is being introduced during the fitting procedure. One possible explanation for the depletion of charge at the atomic centres is that the thermal smearing model applied to the theoretical structure factors calculated from the wavefunction is inadequate. If the thermal motion is incorrectly modelled then one might expect to see the largest effects at places of the highest density i.e. the core.

More significant differences between multipole refinement and constrained-wavefunction fitting are observed in the ELF and electrostatic-potental maps. In all three systems, the electrostatic-potential maps from the charge-density analysis suggest a

much larger polarisation of the molecule, which is most evident in the case of DAN which shows a much larger region of negative electrostatic potential around the nitro group in the charge-density map than the one derived from the constrained wavefunction. This difference in charge separation is further highlighted when the dipole moments are compared. In each case, the dipole moments derived from charge-density analysis are significantly larger than from wavefunction fitting with a smallest (not insignificant) difference of 3.8D observed in the case of MBANP. This is not so surprising when one considers that the partial atomic charges even show sign charges for some atoms.

The ELF, which represents the organisation of chemical bonding in direct space, exhibits the largest differences between the methods of multipole refinement and wavefunction fitting and is therefore apparently more sensitive to the model density. However, it should be pointed out that the sharp, blocky features in the ELFs of the charge-density derived maps are thought to be artifacts of how the molecular envelope is handled in XD and not a physically meaningful feature of the electron-localisation function.

What is clear from the results presented above is that multipole refinement of X-ray diffraction data and constrained wavefunction fitting to the same data produce noticeably different descriptions of the charge-density distribution. However the task of deciding whether one or the other is a more legitimate representation of the charge density is not straightforward. Since we know that multipole refinements of purely X-ray diffraction data typically overestimate the dipole moment considerably, as discussed in Section 4.6, and that there is evidence to suggest that the signs of the partial charges are highly model dependent and often depend very much on exactly which parameters are refined [93], this in all likelihood explains why the dipole moments from charge-density analysis are elevated with respect to the fitted calculations. However it appears that the wavefunction-fitting procedure may be more dependent on the thermal-smearing model than first anticipated.

What is clear however is that there is much more consistency between the properties/maps across different molecules using the same technique to obtain the charge density than investigating the same molecule using the two different techniques of

charge-density analysis and wavefunction fitting. Clearly more work is required to understand how the modelling of the thermal motion affects the fitted density, while paying particular attention to the behaviour of the core electrons.

Chapter 7

Charge-Density Study of NNDPNA

7.1 Introduction

N,N-dimethyl-4-nitroaniline (NNDPNA) is a member of the nitroaniline family of NLO prototype materials. Despite its simple chemical structure and the ease with which good quality crystals can be obtained, NNDPNA has not been characterised in terms of its charge density, though the X-ray structure has been known since the mid-sixties [94].

However, the lower resolution of this early study judged by modern standards, resulted in the structure begin redetermined in 2002 by Borbulevych et al [95] along with a series of derivatives with substitutions at the 2-position and 3-position. This study looked at the effect of the substitutions of the bond lengths in order to elucidate the relationship between the various resonance forms of the materials and their associated hyperpolarisability. Using semi-empirical AM1[1] calculations to determine the hyperpolarisability, it was found that the ortho- and meta-substituted compounds had the smallest hyperpolarisability, which was attributed to a reduced contribution of quinoidal resonance form. In contrast, the para-substituted compound NNDPNA, whose dominant resonance form is the quinoid structure, had the

[1] Austin Model 1 [96]

largest hyperpolarisability of 28.34 $10^{-51}Cm^3V^{-1}$ of any of the compounds in the study. Their motivation for this approach was inspired by the bond-length alternation(BLA) studies by Marder et al [97,98], which were an early attempt to quantify the degree of delocalisation in polyene systems and relate it to their non-linear response. These studies showed a distinct relationship between the BLA parameter and the first hyperpolarisability β for a series of compounds with the chemical formula $(CH_3)_2N(CH{=}CH)_nCHO$.

This chapter describes a multipole refinement of high-resolution X-ray diffraction data collected on NNDPNA and its resultant properties. Charge-density studies are still not trivial experiments with many potential pitfalls. Though not an ideal charge-density experiment, the problems encountered during this piece of research highlight important considerations and as such are elaborated on later in this chapter. In addition, the neutron single-crystal structure of NNDPNA is reported in Appendix C and the intermolecular interactions that are so important in influencing the NLO properties have been characterised using a novel approach based on Hirshfeld surfaces and are included in Appendix B.

It was the intention of the author to include also the results of a periodic Hartree-Fock calculation on NNDPNA using the Crystal03 program [32] in order to provide a comparison to the charge-density study and to validate the one-electron properties obtained. One of the challenges associated with periodic ab-initio calculations is to reach a suitable convergence. Very often severe numerical instabilities are encountered, which are typically associated with linear dependencies arising from the most diffuse basis-set functions. Unfortunately a fully converged periodic ab-initio calculation on NNDPNA was not achieved, despite strenous attempts by trying various basis sets and Crystal03 parameters/tolerances.

7.2 Experimental

The material was obtained commerically from Acros Organics in the form of a 99% pure polycrystalline powder. Crystals for both the neutron (Appendix C) and X-ray diffraction study were grown from an ethanol solution using the vapour diffusion

method.

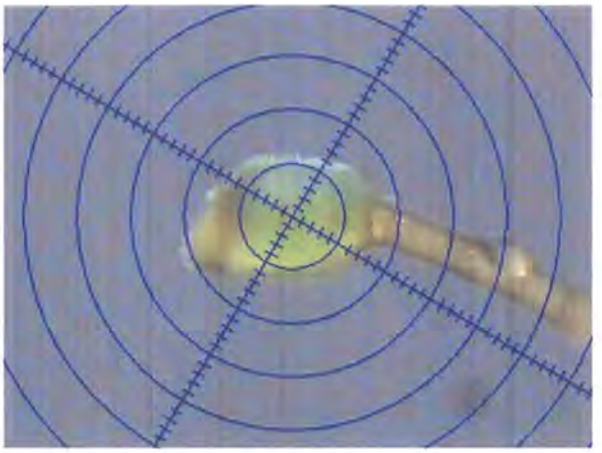

Figure 7.1: The NNDPNA crystal mounted on the goniometer

Diffraction data from a high-quality crystal (Figure 7.1) of dimensions 0.20 × 0.10 × 0.08 mm^3 were collected on a Bruker SMART 6000 single-crystal diffractometer using the Bruker SMART data-collection software [99]. All data were recorded at 120K using an Oxford Cryosystems Cryostream N_2 low-temperature device to reduce the effects of thermal motion. The data were collected in a series of ω-scans at two detector settings ($2\theta = -30°/-70°$) in order to cover as much reciprocal space as possible within the physical limits of the goniometer. Since the high-angle data are weaker due to a fall-off of scattering power with increasing Bragg angle it was necessary to collect those data at the longer exposure time of 50 seconds (cf. 4 seconds at low angle), in order to ensure adequate counting statistics. The coverage was 100% at $2\theta = 70°$ and at the limit of the region swept out by the detector the coverage fell to 89%. Table 7.2 summarises the data-collection strategy utilised.

7.2.1 Data Reduction

Data reduction was performed using Bruker SAINT data-reduction software [100]. The low-angle data were integrated separately to the high-angle data. This approach is favoured since the integration parameters will not be the same in both cases, as a consequence of the different exposure times. Significant problems were encountered when the low- and high-angle data were merged. The data-collection strategy is chosen to ensure that there is a significant region of overlap between the low- and

Run	2θ	ω	ϕ	χ	Width (°)	N_{frames}	Time (s)
1	-30.00	-30.00	0.00	54.74	-0.100	1800	4.00
2	-30.00	-30.00	60.00	54.74	-0.100	1800	4.00
3	-30.00	-30.00	120.00	54.74	-0.100	1800	4.00
4	-30.00	-30.00	180.00	54.74	-0.100	1800	4.00
5	-30.00	-30.00	240.00	54.74	-0.100	1800	4.00
6	-30.00	-30.00	300.00	54.74	-0.100	1800	4.00
7	-70.00	-70.00	0.00	54.74	-0.100	1800	50.00
8	-70.00	-70.00	45.00	54.74	-0.100	1800	50.00
9	-70.00	-70.00	90.00	54.74	-0.100	1800	50.00
10	-70.00	-140.00	132.00	54.74	-0.100	200	50.00
11	-70.00	-220.00	228.00	54.74	-0.100	300	50.00
12	-70.00	-70.00	135.00	54.74	-0.100	1800	50.00

Table 7.1: Data-collection strategy for NNDPNA

high-angle data. This overlap assists greatly in the scaling and merging of the two data sets. Given that the high-angle data were recorded directly after the low-angle data and that no changes were made to the data-collection conditions, one would expect linear scaling between the two data sets due only to the change in exposure time.

Surprisingly a linear relationship was not found between the data sets, so the low-angle and high-angle data were each merged separately using the program SORTAV [101]. Each data set was also corrected for absorption using SADABS v2.10 [102]. In addition, systematic absence violations were removed ($0k0$, $k = 2n + 1$ in $P2_1$) and all symmetry equivalent reflections were merged since anomalous dispersion was deemed insignificant. The multipole refinement was therefore performed with separate scale factors for each data set.

Even though the multipole refinement program XD [16] has the facility to use multiple data sets each with their own scale factor, it does not accept multiple instances of the same reflection. Since the low- and high-angle data were not merged into a single data set, there is a problem of how to treat the data in the over-

lap region. For reflections common to both data sets, the strategy chosen was to keep the reflection with the largest $I/\sigma(I)$ ratio. Though it is recognised that the estimated standard deviations in X-ray diffraction experiments only give at best general indication of the confidence in a particular measurement, this method does solve the problem of the overlap region and gave the best refinements of all the merging strategies attempted.

7.2.2 Multipole Refinement

The structure was solved and initally refined within the spherical-atom approximation using SHELXL [103]. The aromatic hydrogen atoms were added geometrically whilst the methyl hydrogen atoms were found in the Fourier difference map. These were refined using a riding model, setting U_{iso} to 1.5 times the U_{eq} of the corresponding carbon atom for the aromatic C–H's and 1.2 times the U_{eq} in the case of the methyl hydrogen atoms. The model obtained was used as the starting model for a multipole refinement, performed using the XD package [16].

Since this particular refinement is only based on the X-ray diffraction data, the bonds to hydrogen atoms are anomalously short, for reasons discussed in Section 1.1.3. Constraints were used during the refinement to maintain the C–H bond lengths at their equivalent neutron distances of 1.08Å for aryl hydrogen atoms and 1.09Å for the alkyl hydrogen atoms. These values were obtained from International Tables of Crystallography [104].

The XD program has a limited treatment of crystallographic symmetry. Consequently, in order for the charge density to retain the full crystallographic symmetry, site-symmetry restrictions must be applied. In the case of NNDPNA (point group 2), no site-symmetry restrictions are required. In addition, special care must be taken with polar spacegroups, which is the case with NNDPNA. The spacegroup $P2_1$ has one polar axis b, which means the y-coordinate of one atom must be fixed during the refinement. For the multipole refinement of NNDPNA, the y-coordinate of atom O(2) was fixed.

The refinement was performed on F rather than F^2, because although the convergence is general slower, there is less chance of getting stuck in false minima and

it does not give an unnecessary higher weighting to the high-angle data.

The choice of which multipole parameters are refined is dependent upon to which row of the periodic table the atom belongs. Atoms belonging to the first row are typically refined to the level of the octupoles and second-row atoms to the level of the hexadecapoles. Since NNDPNA comprises C, H, N and O, refinement is only necessary to the level of the octupoles. However, due to the lack of core electrons for hydrogen atoms, typically only the monopoles and bond-directed dipoles are refined for hydrogen. In addition, it is not possible to refine both the atomic displacement parameters and the multipole population parameters simultaneously for these atoms, so the hydrogen U_{iso} is fixed during a multipole refinement.

As mentioned in Section 1.1.2, the κ and κ' parameters give added flexibility to the multipole model allowing the expansion or contraction of the valence and deformation terms respectively. The κ parameter is actually defined on a per atom basis in Equation (1.18), while the κ' parameter is defined on a per multipole basis. However, it is common practice to use just one κ parameter and one κ' parameter for all atoms of the same chemical element. This greatly reduces the total number of parameters to be refined and improves the stability of the refinement. In the multipole refinement of NNDPNA, separate κ parameters were refined for the chemical elements carbon, nitrogen and oxygen. The κ and κ' parameters of all hydrogen atoms were fixed during the refinement to 1.16, corresponding to the Stewart-Davidson-Simpson (SDS) values [105].

7.2.3 Results

The crystallographic and refinements details for the charge-density study of NNDPNA are reported in Table 7.2. The refinement was carried out on 27493 reflections achieving an $R_{1,all}(F)$ of 0.0242 with a data to parameter ratio > 12.

Figure 7.2 shows the structure of NNDPNA with the thermal ellipsoids at the 50% probability level. One of the interesting features of the crystal structure of NNDPNA is the eclipsed orientation of the methyl hydrogen atoms (H(7A) and H(8A)), which enables extensive hydrogen bonding with the oxygen atoms of the nitro groups as shown in Figure 7.3.

Empirical Formula	$C_8H_{10}N_2O_2$
Formula Weight (g mol^{-1})	166.177
Crystal System	Monoclinic
Space Group	$P2_1$
Z	2
$F(000)$	88
Crystal Size (mm^3)	$0.20 \times 0.10 \times 0.08$
Crystal form, Colour	block, yellow
Temperature (K)	120
Wavelength λ (Å)	0.71073
a (Å)	3.8722(1)
b (Å)	10.4997(3)
c (Å)	9.6190(3)
β (°)	90.019(1)
V (Å^{-3})	392.59(5)
D_x (g cm^{-3})	1.51
μ (mm^{-1})	0.11
$(\sin\theta/\lambda)_{max}$ (Å^{-1})	0.47
Completeness (%)	97.1
N_{tot} (High Angle)	14641
R_{int} (High Angle)	0.0168
N_{tot} (Low Angle)	27493
R_{int} (Low Angle)	0.0254
N_{tot}	27493
N_{uniq}	4594
$R_{1,all}(F)$	0.0242
$R_{1,ref}(F)$	0.0196
$R_{w,ref}(F)$	0.0179
N_{ref}/N_v	> 12

Table 7.2: Details of the charge-density experiment on NNDPNA

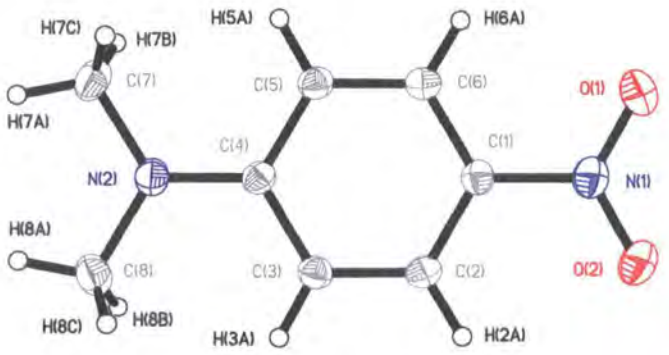

Figure 7.2: Structure of NNDPNA with thermal ellipsoids at 50% probability level

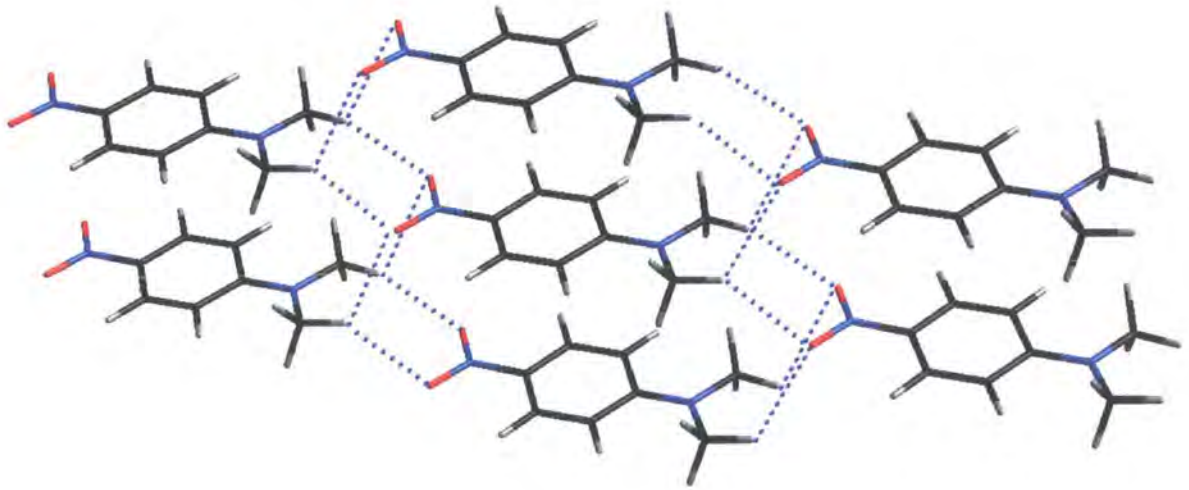

Figure 7.3: Packing diagram of NNDPNA. Dotted lines show the hydrogen bonding.

In practice no X-ray diffraction dataset is perfect and consequently it may not in fact be possible to refine all the multipole parameters. This is particularly true of the κ' parameter, which is the least well defined of all the multipole parameters. In this study on NNDPNA, the refinement was stopped at the κ level with none of the κ' parameters being refined since convergence could not be achieved and when attempted, the resultant multipole parameters were unreasonable. The differences between the two refinements are highlighted by the residual density map (Figure 7.4), which shows that in the κ' refinement, there are many more regions of density unaccounted for, particularly on the atomic positions and especially in the centre of the phenyl ring.

Complete lists of the fractional atomic coordinates and the atomic displacement

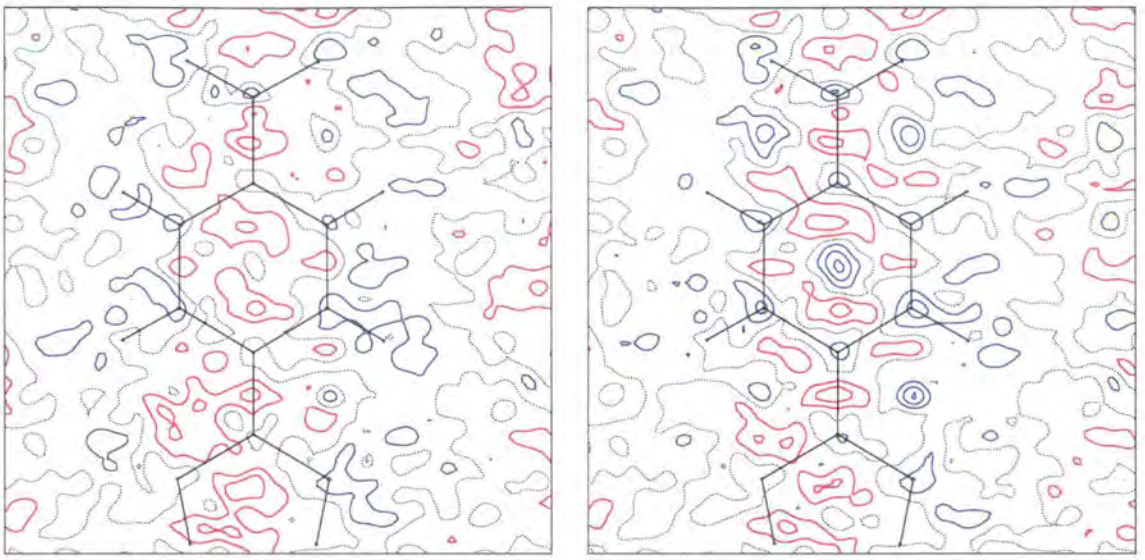

(a) (b)

Figure 7.4: NNDPNA: Residual fourier density map $|F_o - F_c|$ for (a) κ refinement (b) κ' refinement. Contour interval is 0.05eÅ^{-3}. Positive regions denoted by blue contours and negative regions by red contours.

	x	y	z		x	y	z
O(1)	0.39065(22)	0.33628(09)	1.31039(07)	H(2A)	0.54789	0.61923	1.05684
O(2)	0.59195(22)	0.52777	1.28700(07)	H(3A)	0.37565	0.61983	0.80972
N(1)	0.44315(12)	0.43328(10)	1.23968(05)	H(5A)	-0.06157	0.24567	0.86196
N(2)	0.04011(11)	0.43364(09)	0.68107(04)	H(6A)	0.09517	0.24957	1.10819
C(1)	0.33195(08)	0.43476(09)	1.09750(04)	H(7A)	-0.15353	0.33602	0.50843
C(2)	0.41093(09)	0.53904(09)	1.01345(04)	H(7B)	-0.35623	0.29958	0.66961
C(3)	0.31579(09)	0.53917(09)	0.87505(04)	H(7C)	0.06059	0.23972	0.63323
C(4)	0.13766(08)	0.43390(09)	0.81636(04)	H(8A)	0.02754	0.52163	0.48664
C(5)	0.06464(09)	0.32864(09)	0.90443(04)	H(8B)	-0.03703	0.62427	0.63196
C(6)	0.15820(09)	0.32991(09)	1.04289(04)	H(8C)	0.38245	0.56434	0.59485
C(7)	-0.11163(12)	0.32063(10)	0.61922(05)				
C(8)	0.10805(12)	0.54307(10)	0.59265(05)				

Table 7.3: Fractional atomic coordinates of NNDPNA

parameters of NNDPNA are given in Table 7.3 and Table 7.4 respectively.

The deformation-density map obtained from the multipole refinement is shown

	$U11$	$U22$	$U33$	$U12$	$U13$	$U23$
O(1)	0.04711(34)	0.03265(26)	0.02020(22)	-0.00422(26)	-0.00630(21)	0.00655(20)
O(2)	0.04291(31)	0.03540(29)	0.02014(23)	-0.01059(26)	-0.00613(20)	-0.00485(20)
N(1)	0.02554(17)	0.02485(16)	0.01587(15)	-0.00068(17)	-0.00168(12)	-0.00079(15)
N(2)	0.02358(15)	0.01910(13)	0.01679(14)	0.00116(14)	-0.00248(11)	-0.00113(13)
C(1)	0.01724(12)	0.01599(11)	0.01586(12)	0.00020(12)	0.00021(09)	-0.00095(11)
C(2)	0.01843(13)	0.01450(11)	0.01802(14)	-0.00160(11)	-0.00015(10)	-0.00153(11)
C(3)	0.01857(12)	0.01361(11)	0.01776(13)	-0.00082(11)	0.00017(10)	0.00021(11)
C(4)	0.01613(11)	0.01397(10)	0.01596(12)	0.00076(11)	-0.00053(09)	-0.00064(11)
C(5)	0.01845(12)	0.01394(11)	0.01884(14)	-0.00101(11)	-0.00166(10)	-0.00028(11)
C(6)	0.01916(13)	0.01474(12)	0.01796(14)	-0.00081(12)	-0.00022(10)	0.00106(11)
C(7)	0.02548(17)	0.02502(17)	0.02310(18)	0.00013(15)	-0.00618(13)	-0.00609(14)
C(8)	0.02755(17)	0.02685(17)	0.01924(17)	0.00106(16)	-0.00089(13)	0.00443(14)

Table 7.4: Atomic displacement parameters of NNDPNA

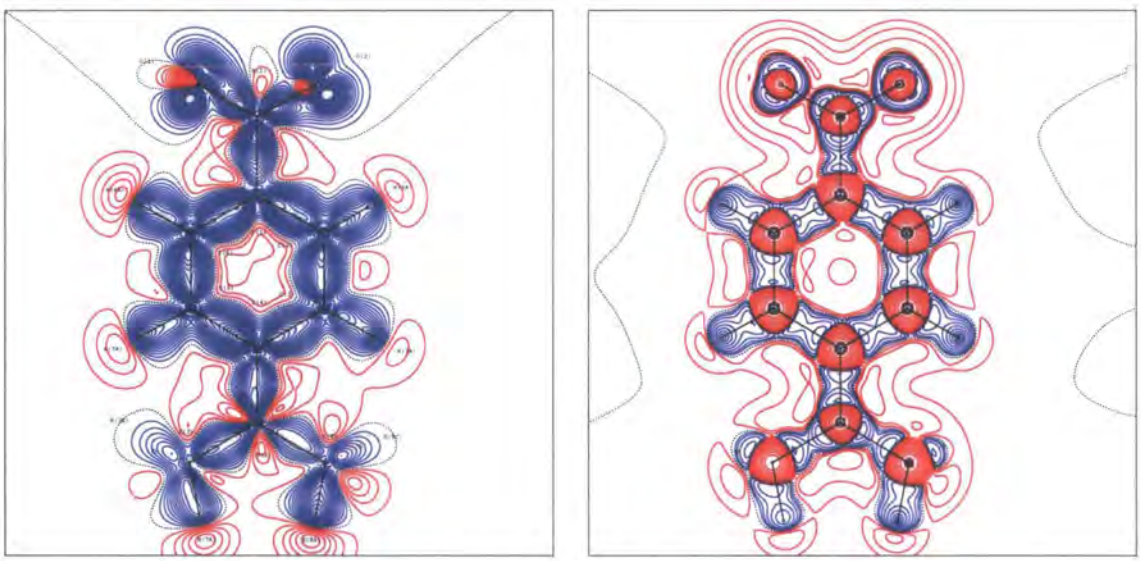

(a) (b)

Figure 7.5: (a) Deformation density of NNDPNA. Contours at intervals of 0.05eÅ^{-3}. (b) Negative Laplacian of the electron density of NNDPNA. Contours at intervals of $\pm 2^n$ eÅ^{-5}, where $n \geq 0$. Blue contours indicate positive regions and red indicate negative regions.

in Figure 7.2.3(a). The magnitudes and shapes of the deformations are consistent with what is expected for the functional groups present, with the majority of the

charge concentrated in the bonding regions. The negative Laplacian of density is shown in Figure 7.2.3(b), and demonstrates where the charge is locally accumulated or depleted. Notable features are the lone pairs on the oxygen atoms of the nitro group and the core structure of the C, N and O atoms.

	q	q_x	q_y	q_z		q	q_x	q_y	q_z
O(2)	-0.1581	-1.0293	-0.7542	-2.3903	H(2A)	0.1993	1.1388	1.8773	0.8974
O(1)	-0.2107	-0.5797	1.0296	-3.4132	H(3A)	-0.0234	-0.0582	-0.2211	0.1629
N(2)	-0.0088	0.0333	-0.0002	0.1133	H(5A)	0.0224	-0.1279	-0.2127	-0.1016
N(1)	0.1060	0.3957	0.0004	1.3707	H(6A)	0.1642	-0.4555	-1.5269	1.1307
C(4)	-0.1203	0.2362	-0.0043	0.7969	H(7A)	-0.0236	0.1746	0.1156	0.4922
C(1)	-0.0680	-0.1128	-0.0054	-0.4326	H(7B)	0.0254	-0.2841	-0.1711	-0.3405
C(2)	-0.0842	-0.2639	-0.4494	-0.2088	H(7C)	0.0224	-0.0762	-0.2186	-0.3379
C(3)	-0.1276	-0.1736	-0.6820	0.4995	H(8A)	-0.0143	0.0574	-0.0638	0.3126
C(6)	-0.1423	0.2254	0.7414	-0.5465	H(8B)	0.1004	-0.5244	0.9675	-1.5207
C(5)	-0.0030	0.0100	0.0158	0.0077	H(8C)	0.0724	0.1890	0.4789	-1.2207
C(8)	0.2201	-0.5531	1.2197	-3.7337					
C(7)	0.0511	-0.3382	-0.2902	-0.8041					

Table 7.5: Atomic partial charges of NNDPNA

The atomic partial charges obtained from the multipole refinement are given in Table 7.5. These clearly show the charge donation from the substituted amine to the nitro group, making NNDPNA a highly polar molecule. There also appears to be an unexpected charge asymmetry in the direction perpendicular to the charge transfer, which is highlighted by the very different charges observed on the methyl carbon atoms (7 and 8) and between the two oxygen atoms. Three of the hydrogen atoms (H(3A), H(7A) and H(8A)) also have apparent negative charges, which one would not expect to see based on an electronegativity argument for those groups.

The dipole moment for an isolated molecule of NNDPNA was calculated at the RHF/6-31G** level of theory using the Gaussian [55] program, and is reported in Table 7.6 along with the in-crystal dipole moment obtained from the multipole refinement. Based on these values alone, it would appear the NNDPNA has a re-

	Gaussian	Multipole
μ_x	-0.0565	-10.8(9)
μ_y	0.0552	0.7(20)
μ_z	-8.5718	-30.4(19)
$\|\mu\|$	8.5722	32.2(18)

Table 7.6: Dipole moment of NNDPNA (Debyes)

markable dipole-moment enhancement from the solid state compared to the isolated molecule of 23.6D. Such an enhancement is often explained solely in terms of the charge redistribution upon crystallisation due the effects of the crystal field and of intermolecular interactions.

There are many other examples of apparent dipole-moment enhancements over 100% in the literature [106–110]. The definitive and oft-cited example of dipole-moment enhancement in the solid state, is the work carried out by S.T. Howard et al [58] on MNA, in which an enhancement from 8.2D to 19.5D was observed, corresponding to an increase of ~238%. However, a careful reassessment of the MNA charge density study by Whitten et al [63] using X-ray/neutron diffraction data at 100K supplemented with ab-initio crystal Hartree-Fock calculations showed a considerably smaller enhancement of 30%-40% to give an overall enhancement of just $\sim$ 2.5D.

Whitten et al. [63] noticed that nearly all the examples of major dipole-moment enhancements were in non-centrosymmetric materials and in which the hydrogen atoms had been treated isotropically – a common approach in studies with an absence of neutron-diffraction data. It was noted that such a description of the hydrogen atoms not only affected the multipole parameters of the adjacent atoms but also those of other atoms *further* away in the structure. Their approach to this was to use ab-initio calculations to model the thermal motion and thus obtain estimates for the atomic displacement parameters of the hydrogen atoms [53, 111].

7.3 Conclusions

In this chapter, the charge-density analysis of the NLO prototype material NNDPNA was presented. Unfortunately significant problems were encountered during the merging of the X-ray diffraction data, which was collected necessarily at two different detector positions and with two different exposure times. In order to facilitate the multipole refinement, separate scale factors were used for the two data sets and the overlap of data was resolved by selecting those reflections in which we have the greatest confidence i.e. the largest ratio of I/σ.

From the refinement, reasonable maps of the deformation density and negative Laplacian of the density were obtained, showing the expected features for the functional groups present in NNDPNA. Despite this, there is mounting evidence to suggest that the in-crystal dipole moment obtained was significantly overestimated. Consequently, some sceptism must be applied to the interpretation of the one-electron properties obtained from such a model.

This work is certainly not the first example of observed dipole-moment increases of greater than 100% for a molecular crystal. Clearly greater care is required when carrying out charge-density experiments especially of non-centrosymmetric systems, with particular attention required in the treatment of the hydrogen atoms. With this in mind, it may not in fact be possible to obtain the most accurate charge densities from X-ray diffraction data alone.

Due to the problems and limitations already outlined, the X-ray diffraction data of NNDPNA should ideally be recollected and combined with the neutron diffraction data given in Appendix C in order to make full use of the accurate positional and atomic displacement parameters of the hydrogen atoms.

Chapter 8

Summary and Future Work

8.1 Summary

It is now possible to calculate CPHF dipole polarisabilities, CPHF hyperpolarisabilities and refractive indices directly from experimental wavefunctions constrained to the X-ray diffraction data using the Tonto quantum-chemistry package [37]. The implementation of the CPHF (hyper)polarisabilities were checked against the Gaussian quantum mechanics package and were found to be in excellent agreement.

The CPHF polarisabilities and associated refractive indices obtained from wavefunction fitting are comparable but by no means superior to the approximate polarisabilities derived by the Sylvain-Csizmadia approach [42]. In addition, refractive indices and CPHF hyperpolarisabilities appeared to be underestimated with respect to dispersion-corrected experimental measurements, which may suggest that even introducing the effects of the crystal field via fitting to the X-ray diffraction data is insufficient to reproduce accurately these experimental observations.

One of the more noticeable effects of the wavefunction fitting was large changes in the core-density descriptions of all atoms, which was highlighted with respect to the ab-initio charge density in the 'difference' maps and also with respect to the multipole-model charge density in the deformation density maps. It is unclear at the present time whether these core changes are genuine or the result of some undesirable effect introduced by way of the fitting procedure. It was speculated that the thermal-smearing model used may be the cause.

As well as a qualitative comparison between constrained-wavefunction calculations and charge-density analysis of the X-ray diffraction data, the dipole moments and partial atomic charges obtained from the two models were also compared and showed significant differences. Recent work by Whitten et al [63] showed that when hydrogen atoms are treated isotropically in multipole refinements, it has a large effect on the multipole parameters of *other* atoms in the model often resulting in dipole-moment enhancements greater than 100% instead of the $30\% - 40\%$ that is expected. In this regard, the dipole moments from the wavefunction-fitting seem to suggest much more reasonable dipole-moment enhancements than those obtained from the multipole refinements. Clearly great care must be taken with the collection of the X-ray diffraction data since it can lead to erroneous electrostatic properties from multipole refinements but also the wavefunction-fitting technique itself seems to be sensitive to systematic errors in the data, as was shown by the Fourier ripples in the crystal error map of PNP (Figure 5.5(b)).

The technique of constraining electronic wavefunctions to X-ray diffraction data shows great promise and there is still much work to be done to understand them. The following section oulines areas in which further work is recommended.

8.2 Future Work

Further investigate the differences between multipole refinements and constrained-wavefunction fitting of X-ray diffraction data for other compounds. In addition to looking at the maps and properties reported in this thesis, a more quantitative approach could be taken, looking at higher electrostatic moments (e.g. quadrupole moments), electric field gradients and additional topological features (e.g. bond critical points).

Recollect the high-resolution X-ray data set on NNDPNA and combine it with the neutron-diffraction data discussed in Appendix C. This should give greatly improved estimates of the electrostatic properties (partial atomic charges and dipole moments).

Apply the technique of constrained-wavefunctions to many more systems not

limited to organic NLO materials, for example, organometallic and inorganic compounds and consider other phenomena e.g. magnetic properties.

Appendix A

Estimation of the Accuracies of the Calculated Properties

The values reported for the linear and non-linear optical properties, namely the (hyper)polarisabilities and refractive indices (Chapters 4 and 5) give no indication as to their accuracies. These can be estimated however by considering the relationship between these calculated properties and the variability in the experimental structure factors, such as was performed on α-oxalic acid dihydrate to obtain esimates of the accuracies of various topological parameters of the charge density [91].

A random-error data set was constructed by applying a small perturbation to the experimental structure factors $F_o(\mathbf{h})$ with associated errors $\sigma(\mathbf{h})$ using the following scheme:

$$F_{re}(\mathbf{h}) = F_o(\mathbf{h}) + A\sigma(\mathbf{h}) \tag{A.0.1}$$

where $F_{re}(\mathbf{h})$ are the random-error structure factors and A is a normally distributed random variable with a mean of zero and a variance of one [112]. This approach also requires doubling the experimental $\sigma(\mathbf{h})$ values as discussed by Applebaum [113]. Consequently the termination point for fitting is now $\chi^2 = 2$ for constrained wavefunction calculations of random-error X-ray data sets, rather than $\chi^2 = 1$.

The material MNA was selected and a new constrained wavefunction calculation using the DZP+ basis set was performed on the experimental data, modified using

the above approach. New estimates for the dipole polarisability, hyperpolarisability and refractive indices were obtained and have been denoted 'Random' in subsequent tables. Consequently, percentage errors were calculated using the following scheme:

$$error = |\frac{x_{orig} - x_{ran}}{x_{orig}}| \times 100 \tag{A.0.2}$$

were x_{orig} represents the calculated quantity obtained from the original calculation reported in Section 4.8.3 and x_{ran} represents the corresponding quantity obtained using the random-error data set.

The percentage errors are small for the principal components of the polarisability, the mean polarisability and the refractive indices, which are all less than 5%. This is also true for most components of the full polarisability tensor except most notably two of the off diagonal components, α_{xy} and α_{yz}, which as expected are much more sensitive to errors in the experimental data.

The percentage errors for the dipole hyperpolarisability are however much larger on the order of about 20% with two of the off-diagonal elements (β_{xyy} and β_{yyz}) having very large errors. This again adds further evidence to the fact that the dipole hyperpolarisability is a much more sensitive quantity to calculate.

	α_{xx}	α_{yy}	α_{zz}	$\overline{\alpha}$
Fitted CPHF/DZP+	9.93	18.90	27.01	18.63
Fitted CPHF/DZP+ (Random)	10.04	18.98	26.20	18.40
Error (%)	1.11	0.42	3.00	1.23

Table A.1: MNA: Estimated errors in the principal components of the dipole polarisability and mean polarisability.

	Fitted CPHF/DZP+	Fitted CPHF/DZP+ (Random)	Error (%)
α_{xx}	23.592	23.084	2.15
α_{xy}	-1.517	-1.200	20.90
α_{xz}	6.356	6.019	5.30
α_{yy}	19.344	19.287	0.29
α_{yz}	-1.181	-1.001	15.24
α_{zz}	12.906	12.836	0.54

Table A.2: MNA: Estimated errors in the dipole polarisability tensor.

	n_1	n_2	n_3
Fitted CPHF/DZP+	2.053	1.677	1.343
Fitted CPHF/DZP+ (Random)	2.012	1.675	1.316
Error (%)	2.00	0.12	2.01

Table A.3: MNA: Estimated errors in the refractive indices adjusted for uni-cell volume at temperature of experimental values.

	Fitted CPHF/DZP+	Fitted CPHF/DZP+ (Random)	Error (%)
β_{xxx}	-321.695	-273.751	14.90
β_{xxy}	176.651	150.489	14.81
β_{xyy}	-9.194	-2.605	71.67
β_{yyy}	-44.787	-47.676	6.45
β_{xxz}	-170.590	-145.506	14.70
β_{xyz}	87.936	72.328	17.75
β_{yyz}	-3.309	0.713	121.55
β_{xzz}	-67.599	-57.744	14.57
β_{yzz}	35.691	27.469	23.04
β_{zzz}	-16.992	-13.388	21.21

Table A.4: MNA: Estimated errors in the dipole hyperpolarisability tensor components.

	Fitted CPHF/DZP+	Fitted CPHF/DZP+ (Random)	Error (%)
β_x	-398.488	-334.099	16.16
β_y	167.555	130.283	22.24
β_z	-190.891	-158.181	17.14

Table A.5: MNA: Estimated errors in the vector dipole hyperpolarisability.

Appendix B

Hirshfeld Surfaces and Fingerprint Plots

A recent innovation in the field of crystal structure analysis is the use of Hirshfeld surfaces to study the packing and interactions of molecules in the crystal. Hirshfeld surfaces provide an alternative means of partitioning the electron density to that of QTAIM discussed in Section 1.1.2. This approach is based upon the Stockholder partitioning scheme [114], which defines a "fuzzy" boundary for a molecule in the crystal, which is dependent upon a weighting function $w(\mathbf{r})$ (B.0.1). The Hirshfeld surface is defined for $w(\mathbf{r}) = 0.5$, that is, a surface inside which the electron density is dominated by contributions from the molecule for which that surface is defined.

$$w(\mathbf{r}) = \frac{\sum_{i \in molecule} \rho_i^{at}(\mathbf{r})}{\sum_{i \in crystal} \rho_i^{at}(\mathbf{r})} \tag{B.0.1}$$

Due to their simple definition, Hirshfeld surfaces are much faster to calculate than QTAIM's atomic basins and also have a number of other useful properties, such as that fact that they are smooth and therefore easily differentiable.

The surfaces themselves provide a convenient means of determining a "coordination number" for a molecule in the crystal, which is indicated by the number of flat faces of the surface. However, the real benefits of Hirshfeld surfaces come when some property is mapped onto the surface, typically by colour. One of the most useful of

these, is the property d_e, which is defined as the distance from a point on the surface to the nearest atom outside the surface (See Figure B.1 for the Hirshfeld surface of DAN with the d_e property mapped). Areas of red/orange indicate close contacts with neighbouring molecules and are typically seen for hydrogen bonds and other strong intermolecular interactions, whereas the darker blue/green regions indicate regions of greater distance from neighbours.

Likewise the internal distance d_i, is defined as the distance from a point on the surface to the nearest atom inside the surface. A plot of d_e versus d_i for every point on the surface is called a fingerprint plot (See Figure B.2 for the fingerprint plot of DAN). Features found in the fingerprint plots are characteristic of particular interactions. For example, a cluster of points (indicated by a brighter spot) at $d_e = d_i = 1.8$Å is characteristic of π-π stacking interactions. Important interactions can be easily spotted in fingerprint plots and as such, fingerprint plots summarise in a very intuitive way all the intermolecular interactions in a crystal, and provide a *unique* fingerprint for each crystal structure.

For further information on the development and interpretation of Hirshfeld surfaces with mapped properties and the related fingerprint plots consult McKinnon et al [115, 116] and Spackman et al [117, 118]. All of the Hirshfeld surfaces and fingerprint plots were generated using the CrystalExplorer program [119]

Hirshfeld surfaces (with d_e mapped and surrounded by a selection of close neighbours) and fingerprint plots have been generated for the main compounds investigated in this thesis (DAN, MBANP, PNP and NNDPNA) in order to understand better the packing arrangments and intermolecular interactions of these materials.

The crystal structure of DAN is dominated by strong hydrogen bonding between the amide side groups to form chains of DAN molecules, which is evident in the Hirshfeld surface by the large red spot (Figure B.1). The weaker (orange/yellow) interactions between the nitro and N,N-dimethyl substituted aniline groups are responsible for holding these chains together. The fingerprint plot for DAN is shown in Figure B.2. The two spikes pointing forwards the bottom left of the plot are characteristic of hydrogen-bonding interactions, which provides further evidence for the intermolecular interactions involving the amide side chains. The aptly name

"chicken wings", at $d_e = 1.1/d_i = 1.7$ and on the opposite side of the plot, are characteristic of C–H$\cdots\pi$ interactions. From the Hirshfeld surface we can see that these involve the hydrogens of the methyl-substituted aniline group with the phenyl ring. The small feature at $d_e = d_i = 1.2$ is due to a short contact distance between hydrogen atoms of the methyl groups attached to the aniline and amide substituents. Since these groups cannot be involved in favorable interactions, their close proximity is probably a consequence of the crystal-packing arrangement.

Figure B.3 shows the Hirshfeld surface for MBANP, which shows the presence of strong hydrogen-bonding interactions between the hydrogen atoms of the aniline group and oxygen atoms of the nitro group, which are again evident in the fingerprint plot (Figure B.4), by two large spikes pointing to the bottom left. The large wings are again evidence of significant C–H$\cdots\pi$ interactions, involving predominantly the methyl hydrogens of the aniline group with both the benzene and pyridine rings (shown as orange/yellow spots on the Hirshfeld surface). The short contacts between the hydrogen-bonding spikes are due to unfavorable close contacts between aromatic hydrogen atoms on neighbouring pyridine groups, again as a result of the crystal packing arrangement.

The Hirshfeld surface (Figure B.5) and fingerprint plot (Figure B.6) of PNP shows many of the features seen for DAN and MBANP. Hydrogen-bonding interactions between the hydrogen atom of the OH group and the oxygen atom of the nitro group gives rise to the characteristic spikes in the fingerprint plot. In addition, close contacts between the C–H groups on the prolinol ring give rise to even more pronounced features between these spikes. A seeming unique feature in the PNP fingerprint plot is the presence of short side spikes ($d_e = 1.75$ and $d_i = 2.0$ and related feature on the opposite side). These are in fact simply C–H$\cdots\pi$ interactions between the prolinol group and the pyridine ring, which have a much more limited range of contact distances.

Except for the amide side chain at the 2-position, DAN and NNDPNA are structurally very similar, so one might expect to see similar features in their fingerprint plots. The planar nature of NNDPNA results in a very dramatic Hirshfeld surface (Figure B.7) with a great number of close contact "hotspots". The broad wings

are again evidence of C–H$\cdots\pi$ interactions involving the aromatic hydrogens and the benzene ring. However, these interactions are more extensive in NNDPNA and therefore appear less diffuse in the plot, than for DAN. The bright spot at $d_e = d_i = 1.8$Å is characteristic of π–π stacking interactions, which are favoured in the case of NNDPNA because of its planarity. These can be seen in the Hirshfeld surface by the flat areas, situated above and below the phenyl rings.

One of the most noticeable features of the NNDPNAs fingerprint plot is the lack of hydrogen-bonding "spikes", which stand out in the plots for DAN, MBANP and PNP. In fact, there are important hydrogen-bonding interactions between the C–H's of the methyl groups and the oxygen atoms of the nitro group in NNDPNA, which are responsible for the two bright streaks appearing in the fingerprint plot. However, the contact distances are much longer in NNDPNA than for the hydrogen bonding interactions in DAN (Table B.1), which explains the presence of the streaks in the middle of the plot.

H8A$\cdots$O2	2.560	H82$\cdots$O2	2.468
H7A$\cdots$O1	2.601	H71$\cdots$O1	2.594
H8B$\cdots$O1	2.675	H73$\cdots$O1	2.450
H7C$\cdots$O2	2.713		
(a)		(b)	

Table B.1: Selected H$\cdots$O intermolecular contacts (Å) for (a) NNDPNA (b) DAN

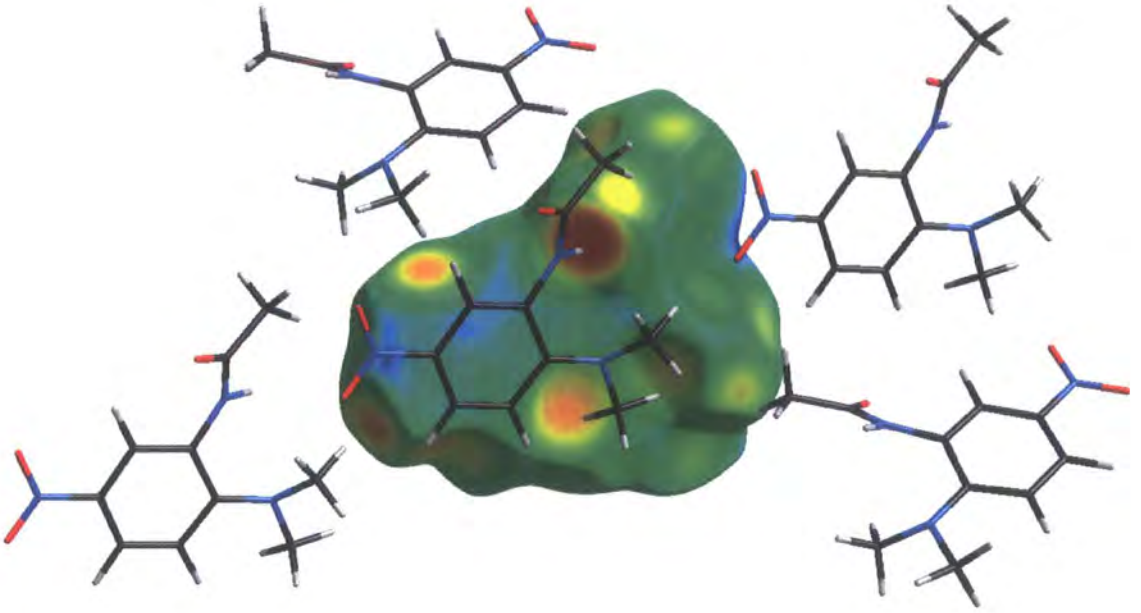

Figure B.1: Hirshfeld surface of DAN with the property d_e mapped onto the surface. All molecules shown are outside the surface.

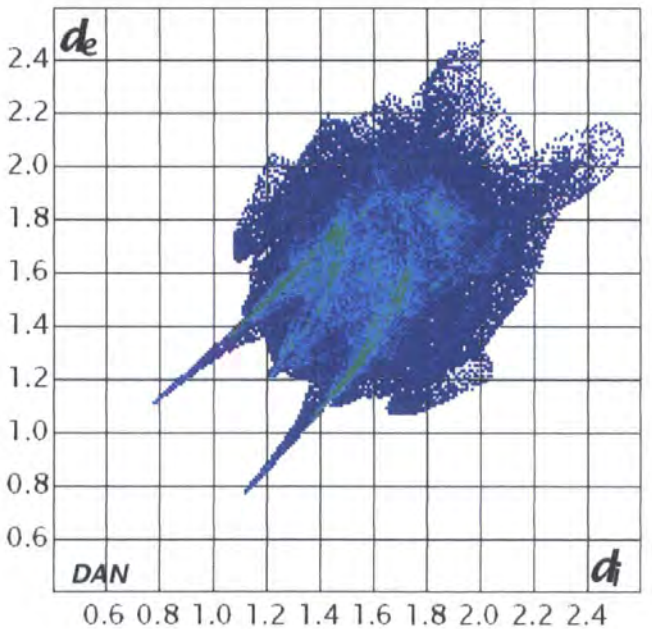

Figure B.2: Fingerprint plot of DAN

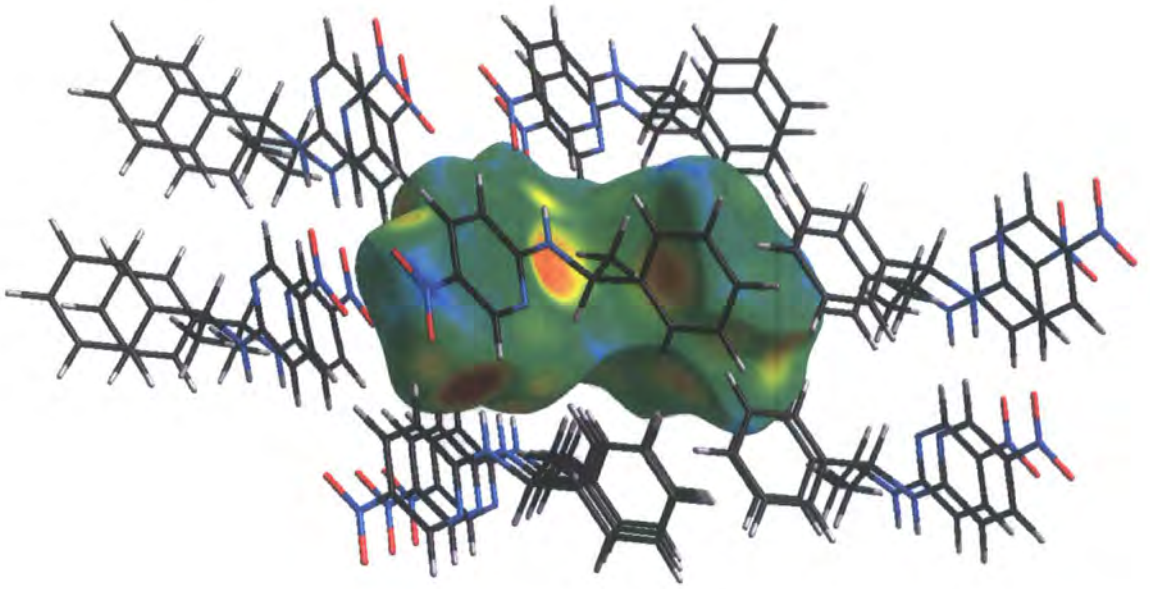

Figure B.3: Hirshfeld surface of MBANP with the property d_e mapped onto the surface

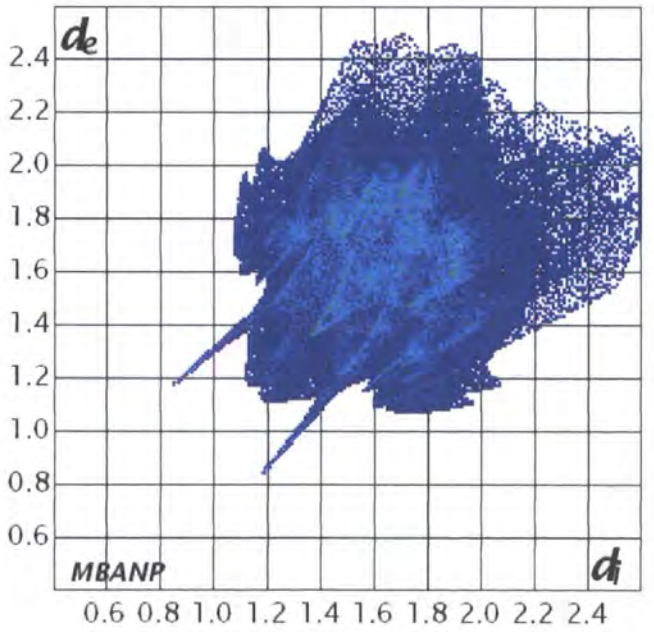

Figure B.4: Fingerprint plot of MBANP

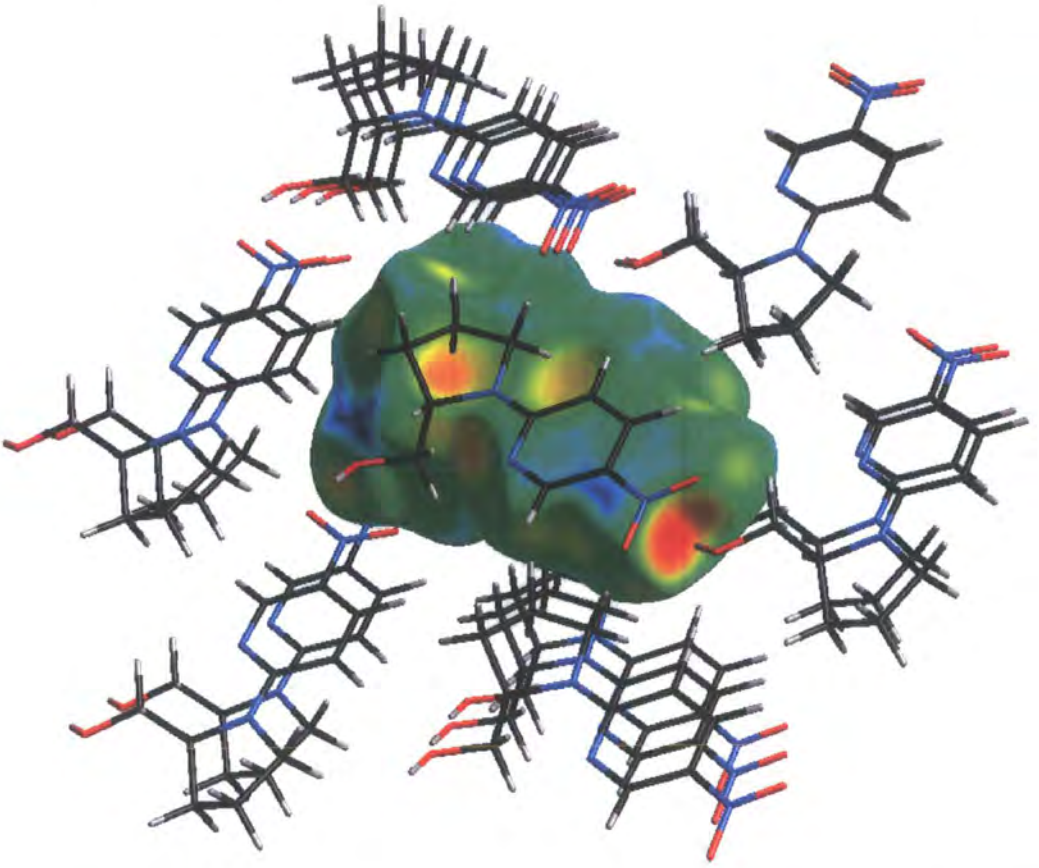

Figure B.5: Hirshfeld surface of PNP with the property d_e mapped onto the surface

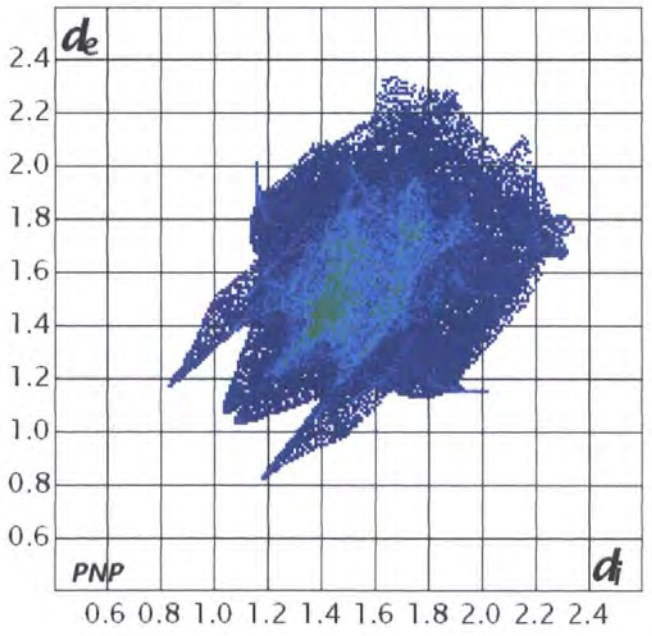

Figure B.6: Fingerprint plot of PNP

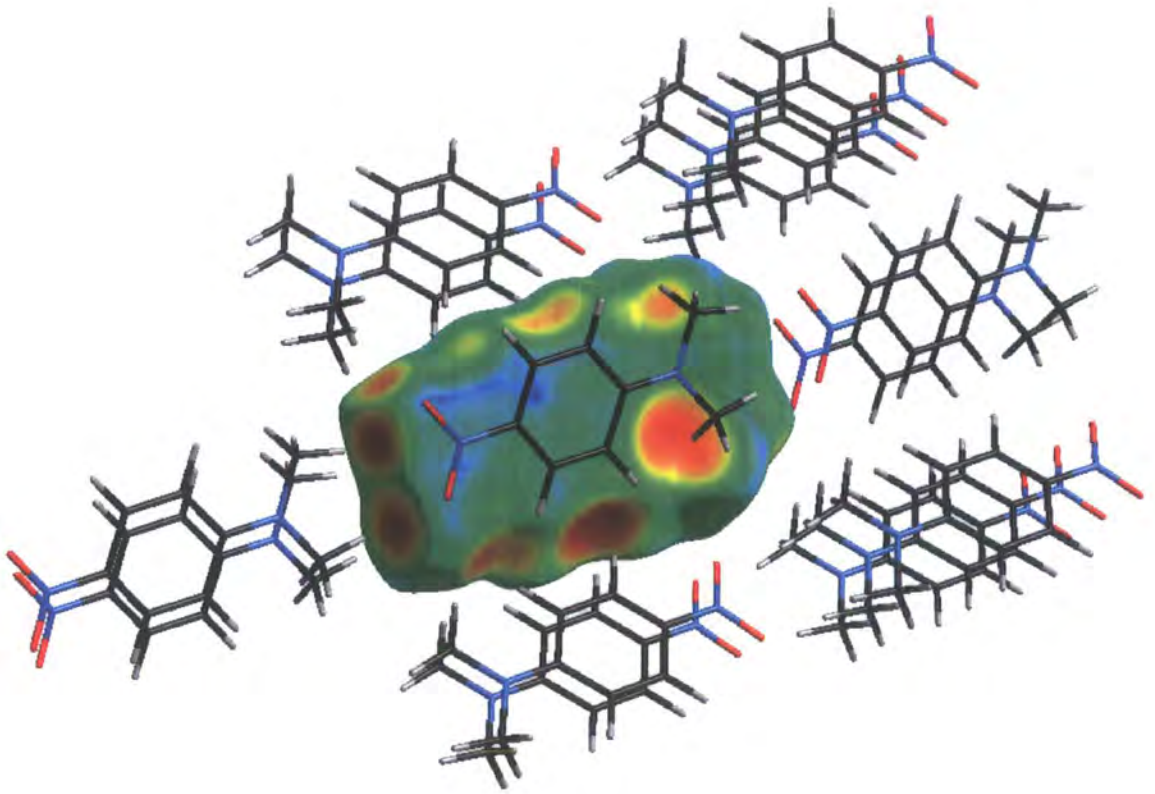

Figure B.7: Hirshfeld surface of NNDPNA with the property d_e mapped onto the surface

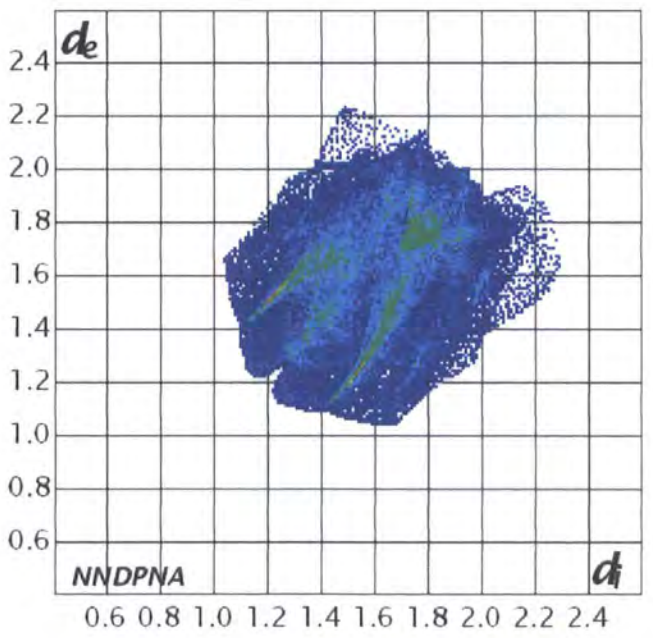

Figure B.8: Fingerprint plot of NNDPNA

Appendix C

Neutron Diffraction Study of NNDPNA

The complementarity of the X-ray and neutron diffraction techniques encouraged the collection of neutron diffraction data on N,N-dimethyl-4-nitroaniline (NNDPNA) in order to obtain accurate thermal and positional parameters. In the case of hydrogen, this information cannot be obtained from X-ray diffraction experiments alone and is consequently especially useful in the determination of accurate charge densities. Though not included in this present work, it is the intention of the author to perform a study combining the charge-density and neutron-diffraction data.

Neutron-diffraction data for NNDPNA were collected at 100K on the hot-source four-circle instrument D9 [120] at the Institut Laue-Langevin (ILL) in Grenoble, France. This instrument was particularly suited to this experiment, since each reflection was measured at the same position on the detector, thus minimising any possible systematic errors.

One large and one small crystal of NNDPNA were selected as candidate crystals. In order to check the quality, both were tested on the "Orient Express", an experimental thermal-beam Laue diffractometer run by Bachir Ouladdiaf at the ILL. Due to the limited dynamic range of the detector on this instrument, five separate exposures must be recorded and then averaged to give a single diffraction image. From the quality of the diffraction pattern, it is possible to judge the suitability of a crystal for a neutron-diffraction experiment before the lengthier process of mounting,

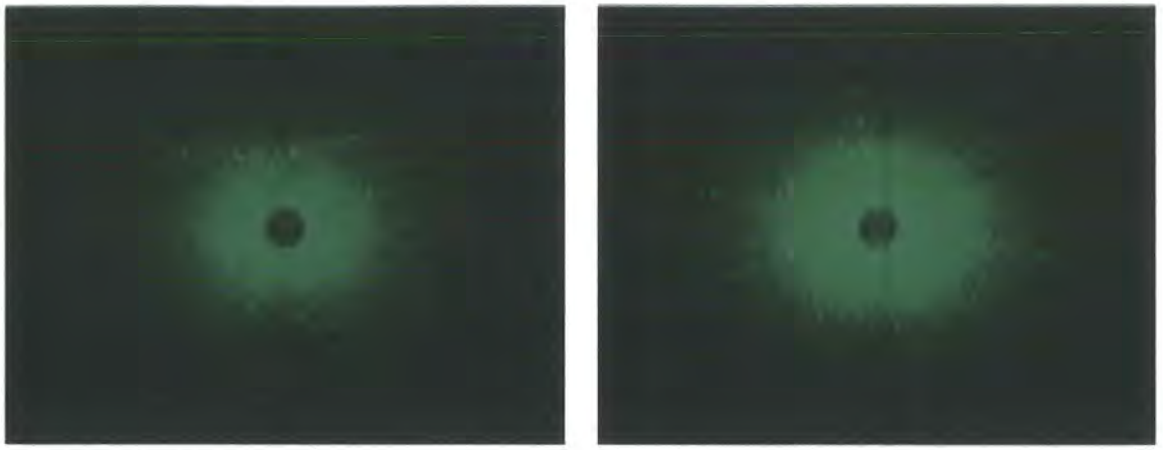

(a) (b)

Figure C.1: Laue diffraction patterns of (a) Large Crystal (b) Small Crystal

centering and recording a low-resolution data set is carried out.

Figure C.1 shows the diffraction images recorded for the large and small crystals on Orient Express. In the case of the large crystal, the presence of two peaks close together in reciprocal space, where only a single reflection is expected (based on the known unit cell), suggests that this crystal is probably twinned and therefore unsuitable for this study. The diffraction from the small crystal looks good, although the crystal is on the lower size limit of what is acceptable on D9. A low-resolution dataset ($\theta_{max} = 35°$) revealed that the crystal was in fact too small, giving data limited in both intensity and resolution. A larger crystal was eventually selected and due to time pressure was mounted immediately on D9.

A yellow ruler-shaped crystal of dimensions $6.41 \times 1.23 \times 0.53$ mm^3 was attached to a vanadium pin with Kwikfill glue and mounted on the offset χ circle in a Displex Cryostat [121]. The data were collected with MAD [122] using ω-x-θ scans up to 72° in 2θ. A wavelength of 0.8317Å was used throughout with an 8mm aperture for the incident beam. Two standard reflections [(1 -4 -6) and (0 -2 0)] were recorded after every 100 reflections and showed no significant variation over the course of the experiment. The orientation matrix was refined using RAFD9 [123]. The final unit-cell parameters obtained were in good agreement with those obtained from the X-ray diffraction experiment. The raw data were integrated using RACER [124] and a face-indexed Gaussian absorption correction was also applied using DATAP [125, 126].

The initial model for the neutron refinement was taken from an earlier X-ray charge-density study performed on NNDPNA. The structure was refined using SHELXL [103] by full-matrix least-squares on F^2 using neutron scattering lengths tabulated in the Neutron Data Booklet [21]. All atoms were refined with anisotropic displacement factors. Figure C.2 shows the neutron structure of NNDPNA with thermal ellipsoid at the 50% probability level. Table C.1 summarises the pertinent details of the data collection and refinement. A list of the fractional atomic coordinates and atomic displacement parameters for all atoms are given in Tables C.2 and C.3 respectively. In addition, structural details for NNDPNA are summarised in Tables C.4 and C.5, which list the bond lengths and bond angles respectively.

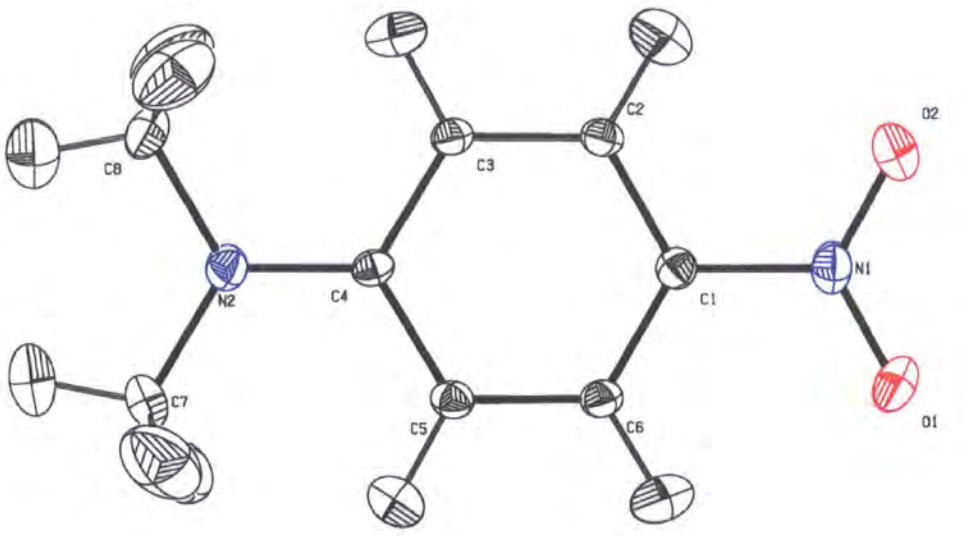

Figure C.2: Neutron Structure of NNDPNA with thermal ellipsoids at the 50% probability level

Empirical Formula	$C_8H_{10}N_2O_2$
Formula Weight (g mol^{-1})	166.177
Crystal System	Monoclinic
Space Group	$P2_1$
Z	2
$F(000)$	146
Crystal Size (mm)	$6.41 \times 1.23 \times 0.53$
Crystal form, Colour	Ruler, Yellow
Temperature (K)	100
Wavelength (Å)	0.8317
a (Å)	3.8859(4)
b (Å)	10.5070(10)
c (Å)	9.6161(9)
β (°)	90.012(5)
V (Å^{-3})	392.62(7)
μ (mm^{-1})	0.189
Absorption Correction	Gaussian
$(\sin\theta/\lambda)_{max}$ (Å^{-1})	0.7067
N_{ref}	1229
$R_{int}(F^2)$	0.0233
$R(F^2)$	0.0487
$wR(F^2)$	0.08427

Table C.1: Crystallographic details of the neutron-diffraction study on NNDPNA

	x	y	z
O1	0.4087(8)	0.7698(3)	1.2865(3)
O2	0.6093(9)	0.9596(3)	1.3100(3)
N1	0.5568(4)	0.86396(19)	1.23988(14)
N2	0.9597(3)	0.86366(15)	0.68114(13)
C1	0.6686(5)	0.8623(2)	1.09750(17)
C2	0.8416(5)	0.96695(18)	1.04318(18)
C3	0.9354(5)	0.96842(17)	0.90431(18)
C4	0.8632(4)	0.8635(2)	0.81633(18)
C5	0.6833(5)	0.75774(17)	0.87497(19)
C6	0.5892(5)	0.75797(18)	1.0132(2)
C7	0.8917(6)	0.7546(2)	0.5929(2)
C8	1.1112(6)	0.9765(2)	0.6193(2)
H2	0.9007(14)	1.0475(5)	1.1089(5)
H3	1.0679(14)	1.0511(5)	0.8636(5)
H5	0.6134(14)	0.6771(5)	0.8102(5)
H6	0.4452(14)	0.6785(5)	1.0567(5)
H7A	1.0094(19)	0.7685(6)	0.4921(6)
H7B	0.6204(15)	0.7397(7)	0.5760(7)
H7C	1.0013(19)	0.6668(6)	0.6366(6)
H8A	1.175(2)	0.9584(7)	0.5119(6)
H8B	1.3474(15)	1.0037(7)	0.6715(7)
H8C	0.9391(16)	1.0576(6)	0.6264(8)

Table C.2: Neutron fractional atomic coordinates of NNDPNA

	U_{11}	U_{22}	U_{33}	U_{12}	U_{13}	U_{23}
O1	0.0402(14)	0.0322(14)	0.0199(11)	-0.0099(12)	0.0051(10)	0.0059(11)
O2	0.0439(16)	0.0302(12)	0.0199(11)	-0.0025(13)	0.0045(10)	-0.0058(11)
N1	0.0233(6)	0.0245(6)	0.0144(5)	-0.0002(7)	0.0014(5)	0.0008(6)
N2	0.0224(6)	0.0168(5)	0.0153(6)	0.0012(6)	0.0013(5)	0.0015(6)
C1	0.0162(7)	0.0144(7)	0.0138(7)	0.0012(8)	-0.0011(6)	0.0011(8)
C2	0.0168(8)	0.0131(8)	0.0159(8)	-0.0008(7)	-0.0004(6)	-0.0013(8)
C3	0.0148(8)	0.0120(8)	0.0172(8)	-0.0008(7)	0.0012(6)	0.0006(7)
C4	0.0136(7)	0.0109(6)	0.0159(7)	0.0003(8)	0.0000(6)	0.0012(9)
C5	0.0173(8)	0.0121(8)	0.0160(8)	0.0005(7)	-0.0019(6)	0.0002(7)
C6	0.0179(9)	0.0129(8)	0.0157(8)	-0.0017(8)	-0.0008(7)	0.0013(7)
C7	0.0252(10)	0.0253(10)	0.0152(8)	0.0020(9)	0.0005(7)	-0.0044(8)
C8	0.0234(10)	0.0233(10)	0.0200(9)	-0.0004(8)	0.0055(7)	0.0053(8)
H2	0.046(3)	0.032(3)	0.032(3)	-0.007(2)	-0.003(2)	-0.0075(18)
H3	0.050(3)	0.022(2)	0.038(3)	-0.0130(19)	0.009(2)	-0.0006(17)
H5	0.047(3)	0.029(2)	0.029(2)	-0.010(2)	0.0036(18)	-0.0094(18)
H6	0.043(3)	0.026(2)	0.037(3)	-0.0118(19)	0.0027(19)	0.0039(18)
H7A	0.069(4)	0.051(4)	0.023(2)	-0.008(3)	0.014(2)	-0.006(2)
H7B	0.038(3)	0.068(4)	0.059(4)	-0.011(3)	-0.004(2)	-0.025(3)
H7C	0.068(4)	0.031(3)	0.040(3)	0.007(2)	-0.004(2)	-0.006(2)
H8A	0.094(6)	0.043(3)	0.030(3)	-0.010(3)	0.017(3)	-0.003(2)
H8B	0.036(3)	0.063(4)	0.061(4)	-0.020(3)	-0.006(2)	0.017(3)
H8C	0.044(4)	0.031(3)	0.070(5)	0.010(2)	0.015(3)	0.016(2)

Table C.3: Neutron atomic displacement parameters of NNDPNA

N1-O2	1.227(4)	C3-H3	1.083(5)
N1-O1	1.229(3)	C6-C5	1.379(3)
N2-C7	1.450(3)	C6-H6	1.089(5)
N2-C8	1.452(3)	C2-H2	1.081(5)
C1-N1	1.437(2)	C5-H5	1.086(5)
C1-C2	1.391(3)	C8-H8A	1.078(6)
C1-C6	1.398(3)	C8-H8B	1.085(6)
C4-N2	1.353(2)	C8-H8C	1.085(6)
C4-C3	1.418(3)	C7-H7A	1.082(6)
C4-C5	1.429(3)	C7-H7B	1.078(6)
C3-C2	1.384(2)	C7-H7C	1.099(6)

Table C.4: Neutron bond lengths (Å) for NNDPNA

N2-C4-C3	121.15(17)	C2-C3-C4	120.99(16)	N2-C8-H8B	111.6(4)
N2-C4-C5	121.08(17)	C2-C3-H3	118.8(3)	H8A-C8-H8B	107.2(6)
C3-C4-C5	117.77(15)	C4-C3-H3	120.2(3)	N2-C8-H8C	111.4(4)
C2-C1-C6	120.59(16)	O2-N1-O1	122.4(2)	H8A-C8-H8C	109.9(6)
C2-C1-N1	119.66(17)	O2-N1-C1	118.9(2)	H8B-C8-H8C	106.6(6)
C6-C1-N1	119.69(18)	O1-N1-C1	118.7(2)	N2-C7-H7A	109.9(4)
C4-N2-C7	120.68(16)	C3-C2-C1	119.90(17)	N2-C7-H7B	112.4(4)
C4-N2-C8	120.50(16)	C3-C2-H2	120.0(3)	H7A-C7-H7B	107.3(6)
C7-N2-C8	118.68(14)	C1-C2-H2	120.1(3)	N2-C7-H7C	111.7(3)
C5-C6-C1	120.13(17)	C6-C5-C4	120.61(17)	H7A-C7-H7C	107.0(5)
C5-C6-H6	120.4(3)	C6-C5-H5	119.2(3)	H7B-C7-H7C	108.3(6)
C1-C6-H6	119.5(3)	C4-C5-H5	120.1(3)		

Table C.5: Neutron bond angles (°) for NNDPNA

Appendix D

Programming Projects

D.1 XtalCommander

Since periodic ab-initio calculations are very computationally intensive, it would be convenient to be able to control, monitor and automate the running of these calculations in order to save time and resources. XtalCommander is a scripting language extension to the Perl programming language for the automation of Crystal03 [32] calculations. One of the major benefits of having access to a complete scripting language is that it allows the automation of tasks that would be remarkably tedious to do by hand, but more importantly allows the user to achieve tasks not anticipated by the creator of Xtalcommander.

The control of Crystal03 is achieved by directly mapping the Crystal03 input parameters to XtalCommander variables. For example, the Crystal03 parameter *MAXCYCLES* is mapped to the variable *$xc_maxcycles*. In addition, XtalCommander provides an extensive set of functions to achieve useful tasks. For example, the routine *xc_create_input*, creates a *.d12* Crystal03 input file based on the values of the mapped variables.

The heart of XtalCommander is the ability to create calculations, run them on available computers, return the output and do some user-defined processing on the results. XtalCommander offers two facilities for running calculations (Figure D.1). The first is a *blocking* calculation, which when submitted waits for the calculation to finish before proceeding with the script. The second type is the more powerful *non-*

blocking calculation, that allows calculations to be distributed over many computers. When a calculation of this type is submitted a *callback* function is registered at the same time. Unlike the scenario for blocking calculations however, the script does not wait for the calculation to finish before continuing, thus allowing the user to do other things. At some point in the future the calculation will end, at which point the callback routine is called, which is able do some kind of processing on the results.

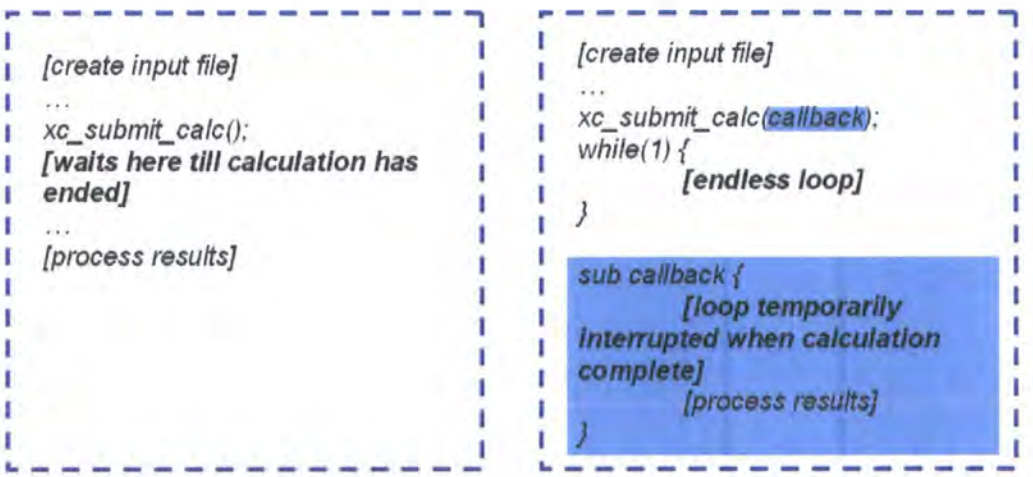

Figure D.1: Pseudocode for (a) Blocking Calculation (b) Non-blocking Calculation

XtalCommander provides many facilities for controlling and processing Crystal03 calculations including:

- Import geometry and crystallographic data from XD files.
- Automatically run sets of calculations with different parameters.
- Manage computers available to do calculations.
- Analyse the calculation output, e.g. check for numerical instabilities.
- Calculate properties, e.g. dipole moments.
- Transform the Crystal03 output, e.g. for multipole analysis.
- Archive the results of calculations.

D.2 HKL Tools

HKL Tools is a collection of codes for the manipulation of crystallographic data, which could be suitable as the basis for a more comprehensive crystallographic toolbox viz. CCTBX. The code is implemented with an object-orientated methodology, to provide the ability to create and manipulate a number of quantities fundamental to diffraction experiments.

The motivation for the creation of this tool set was due to the need to investigate the subtleties of the data merging and scaling of multiple charge-density datasets. In high-resolution data sets, it is typical to collect data sets at two different detector positions and ensure a sufficient overlap of the data sets. Due to the fall-off of intensity with 2θ, the higher-angle data is collected at a longer exposure time. The overlap is essential for the accurate scaling thus required. One consequence of having a region of overlap is the crystallographer then has a choice about how to merge that data. HKL tools provided a convenient and flexible method of testing various possibilities.

D.2.1 Framework: Crystallographic Objects and Associated Methods

reflection : Holds reflection data

Fields:	
h,k,l	Miller Indices
b	Batch Number (optional)
i	Intensity
s	Estimate Standard Deviation
Methods:	
get_dspacing(cell)	Calculate the d-spacing using Bragg Eqn
get_sthl(cell)	Calculate $\sin\theta/\lambda$
get_th(cell)	Calculate θ
compare_ref(ref2)	Are two reflections equivalent
get_bestref(ref2)	See discussion of 'Bestref' program below
get_shelx_string()	Create a textual representation in the SHELX format
get_xd_string()	Create a textual representation in the XD format

cell : Holds the unit cell parameters

Fields:	
a, b, c	Unit cell lengths (Å)
alpha, beta, gamma	Unit cell angles (°)
Methods:	
get_ralpha, get_rbeta, get_rgamma	Converts angles to radians
read_p4p(file)	Read cell parameters from SHELX .p4p file
get_volume	Calculate the cell volume

friedel : Abstract object for the manipulation of Friedel pairs

Fields:	No public fields
Methods:	
gen_pairs(ref)	Generates all the Friedel pairs for a particular space group
list_pairs	Returns all of the Friedel pairs generated using gen_pairs

omatrix : Holds the orientation matrix

Fields:	No public fields
Methods:	
read_p4p	Reads the orientation matrix from a SHELX p4p file

RefConditionCollection : Holds a collection of objects representing reflection conditions and makes use of the RefCondition object

Fields:	No public fields
Methods:	
check_present(ref)	Checks to see whether a reflection is absent
print_rcc	Displays all the reflection conditions

RefCondition : Holds a single reflection condition

Fields:	No public fields
Methods:	No public methods (Used by the RefConditionCollection)

D.2.2 Tools: Programs for Processing Datasets

processhkl: Applies a series of filters to either a SHELX or XD hkl file. The following filters can be applied:

- Remove systematic absence violations.
- Apply an upper and lower cutoff in θ.
- Apply an upper and lower cutoff in F_{obs}.
- Remove reflections with zero estimated standard deviation.

common: Creates a new hkl file containing all those reflections that are common to a series of SHELX hkl files.

bestref: Takes a series of hkl files and for each reflection common to more than one file, the routine 'bestref'[1] is called to determine which reflection is kept. The criteria currently implemented for 'bestref' is to keep the reflection with the largest value of I/σ.

D.3 Tontoprepare

Tontoprepare is a tool for converting the results from a charge-density refinement using the XD package into an input file for TONTO. This program is now distributed with the TONTO package. The following command-line options are supported:

[1] defined for the reflection object

Switch	Description	Default
-b [option]	Specify the basis-set	STO-3G
-d [option]	Specify the location of the basis-set files	Current Directory
-f	Apply filtering to the reflection data	-
-h	List the command-line options	-
-o [option]	Specify the filename for storing the reflection data	tonto.hkl
-s [option]	Specify the spacegroup using HM convention	-
-t [option]	Specify the location of tontoprepare's template files	Current Directory
-v	Display the version number	-
-x [option]	Specify the location of the XD input files	Current Directory

Table D.1: Command-line options available in Tontoprepare

In XD only reflections that meet certain criteria are included in the refinement procedure. The criteria are specified in XD by the SKIP instruction. The -f option applies the following default criteria for including observations:

Identifier	Min. Value	Max. Value	Comment
obsmin	0.0	1.0e10	Include observations where, $obsmax > obs > obsmin$
sigobs	3.0	1.0e06	Include observations where, $sigmax * obs > obs > sigmin * obs$
sinthl†	0.0	2.0	Defines upper and lower cutoffs in $\sin\theta/\lambda$

Table D.2: Default values for reflection omission in XD. † not applied by default

D.4 xd2shelx

xd2shelx is a program for converting XD files back into the SHELX format. Because XD provides no way to visualise the model apart from the various maps, it can be useful to convert back to SHELX files and display thermal-ellipsoid plots in order to check thermal and structural parameters are still reasonable during a charge-density refinement.

Appendix E

DZP Basis Set Description

This basis set was taken from Thakkar [127] based on a $(9s5p)/[4s/2p]$ contraction of a variationally optimised Gaussian basis set [128], supplemented with additional d-type polarisation functions for C, N and O with exponents 0.75, 0.80 and 0.85 respectively, and a p-type polarisation function for H, with an exponent of 1.0. This basis set was used in the wavefunction-fitting calculations performed on benzene, urea and MNA in Chapter 4.

C 0
S 6 1.
0.67799E+04 0.122200E-02
0.10172E+04 0.943000E-02
0.23157E+03 0.480230E-01
0.65547E+02 0.182197E+00
0.21253E+02 0.496064E+00
0.75339E+01 0.385105E+00
S 2 1.
0.75339E+01 0.471311E+00
0.28031E+01 0.571296E+00
S 1 1.
0.52151E+00 0.100000E+01
S 1 1.
0.l5957E+00 0.100000E+01
P 4 1.
0.18734E+02 0.181700E-01
0.41362E+01 0.112687E+00
0.12004E+01 0.376170E+00
0.38346E+00 0.648667E+00
P 1 1.
0.12129E+00 0.100000E+01
D 1 1.
0.75000E+00 0.100000E+01

N 0
S 6 1.
0.95556E+04 0.132700E-02
0.13736E+04 0.102400E-01
0.31273E+03 0.521460E-01
0.88547E+02 0.197926E+00
0.28756E+02 0.538041E+00
0.10246E+02 0.320789E+00
S 2 1.
0.10246E+02 0.524498E+00
0.38442E+01 0.517846E+00
S 1 1.
0.74650E+00 0.100000E+01
S 1 1.
0.22475E+00 0.100000E+01
P 4 1.
0.26667E+02 0.187960E-01
0.59557E+01 0.117689E+00
0.17440E+01 0.383034E+00
0.55629E+00 0.638961E+00
P 1 1.
0.17315E+00 0.100000E+01
D 1 1.
0.80000E+00 0.100000E+01

O 0
S 6 1.
0.11852E+05 0.144500E-02
0.17782E+04 0.111470E-01
0.40486E+03 0.567640E-01
0.11466E+03 0.215473E+00
0.37279E+02 0.584655E+00
0.13334E+02 0.246860E+00
S 2 1.
0.13334E+02 0.569590E+00
0.50385E+01 0.471791E+00
S 1 1.
0.10136E+01 0.100000E+01
S 1 1.
0.30250E+00 0.100000E+01
P 4 1.
0.34493E+02 0.202360E-01
0.77562E+01 0.126799E+00
0.22820E+01 0.394680E+00
0.71691E+00 0.624014E+00
P 1 1.
0.21461E+00 0.100000E+01
D 1 1.
0.85000E+00 0.100000E+01

H 0
S 3 1.
0.1873584E+02 0.334840E-01
0.2825712E+01 0.234719E+00
0.6401376E+00 0.813774E+00
S 1 1.
0.1756080E+00 0.100000E+01
P 1 1.
0.1000000E+01 0.100000E+01

Appendix F

Synthesis of AANP and COANP

2-adamantylamino-5-nitropyridine (AANP) and 2-cyclo-octylamino-5-nitropyridine (COANP) are two related organic NLO systems based on a pyridine core with a nitro accepting group and a mono-substituted amine donor group. The synthetic procedure used to make both AANP and COANP was based on the synthesis of COANP described by Günter et al [129].

All starting materials and solvents were obtained commercially from Aldrich or Lancaster and used as received. Purification by column chromotography was performed using Lancaster silica gel with pore size 60Å. TLC was carried out using Merck aluminium-backed pre-coated plates. ^{1}H-NMR and ^{13}C-NMR spectra were recorded at 400MHz using a Bruker 400MHz spectrometer. $CDCl_3$ was used as the solvent with tetramethylsilane as an internal standard. Evaporations were carried out at 20 mm Hg using a Büchi rotary evaporator and water bath, followed by evaporation to dryness (<2 mm Hg).

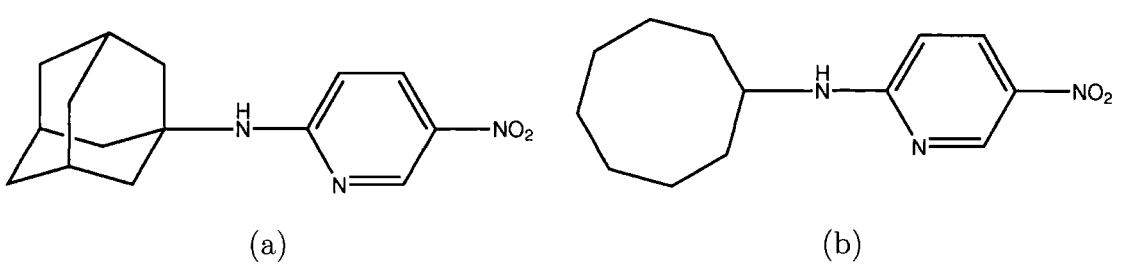

(a) (b)

Figure F.1: Schematic of (a) AANP and (b) COANP

F.1 AANP

A solution of 2-chloro-5-nitropyridine (0.948g, 5.979mmol) and adamantylamine (0.984g, 6.594mmol) in N-methylpyrolidinone (15ml) was treated with triethylamine (1.32ml). The light-brown solution was refluxed under argon protection for 2 hours. The brown oil was subjected to column chromatography (silica gel, hexane:EtOAc gradient elution). The layers were separated and the aqueous was extracted in EtOAc (3 x 20 ml). The combined layers were dried ($MgSO_4$) and the solvent removed under reduced pressure. The produce was obtained as a yellow crystalline solid (0990 g, 61%).

δ_H(400MHz; $CDCl_3$) 1.66 (6H, m), 2.03(6H, m), 2.09(3H, m), 5.29(1H, s), 6.35($1H_A$, d, *J 9.2*), 8.03 ($1H_B$, dd, *J 2.8* and *J 9.2*), 8.91 ($1H_C$, d, *J 2.8*); δ_C (400MHz; $CDCl_3$) 29.67, 36.44, 41.96, 53.19, 128.26, 132.57, 135.33, 146.80, 160.83; m/z (EI+) 272.95 (M^+, 81%) 134.99 ($C_{10}H_{15}{}^+$ (adamantyl), 100%); $C_{15}H_{19}N_3O_2$ requires: C(65.91%), H(7.01%), N(15.37%), actual: C(64.95%), H(6.97%), N(5.68%).

The crude product was recrystallised from acetone using the solvent evaporation technique. A yellow plate ($0.19 \times 0.16 \times 0.02$ mm^3) was selected and the crystal structure determined using a Bruker SMART 6000 CCD diffractometer at 120K. Figure F.2 shows the structure of AANP with thermal ellipsoids at 50% probability level. The structure obtained is in fact a solvate with acetone situated in channels along the [001] direction (Figure F.3). However the solvent is so severely disordered that modelling of the disorder has not proved possible. The disorder was handled using SQUEEZE [130,131], which subtracts the electron density associated with a void in the crystal structure from the observed structure factors. The corrected structure factors were then used to refine the structure as normal. Table F.1 summarises the crystallographic details of the structure determination of AANP.

A later recrysallisation by sublimation of the same sample performed by Dr D.S. Yufit yielded yellow cubic-shaped crystals. A subsequent crystal-structure determination showed that this material was in fact N,N-diethyl-5-nitropyridine-2-amine, a side product of the synthesis of AANP. Full crystallographic details can be found in Yufit et al [132].

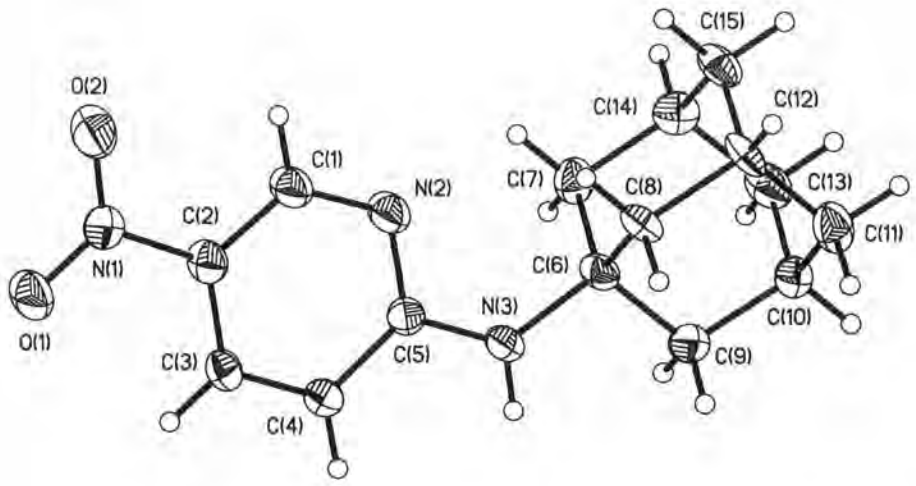

Figure F.2: Structure of AANP with thermal ellipsoids at 50% probability level

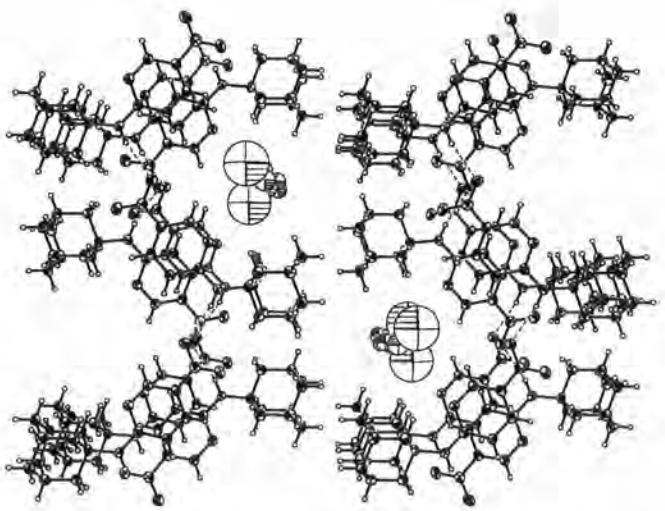

Figure F.3: Packing diagram of AANP and a representation of the disordered solvent looking along [100] direction.

Empirical Formula	$C_{15}H_{19}N_3O_2$
Formula Weight (g mol^{-1})	273.33
Crystal System	Orthorhombic
Space Group	$Pca2_1$
Z	4
$F(000)$	88
Crystal Size (mm^3)	$0.19 \times 0.16 \times 0.02$
Crystal form, Colour	Plate, Yellow
Temperature (K)	120
Wavelength (Å)	0.71072
a (Å)	15.7914(5)
b (Å)	15.6895(5)
c (Å)	6.6.373(2)
V (Å^{-3})	1644.45(4)
$(\sin\theta/\lambda)_{max}$ (Å^{-1})	0.6388
N_{ref}	2933
$R_{int}(F)$	0.0308
$R(F)$	0.0285
$wR(F)$	0.0298

Table F.1: Crystallographic details of the X-ray diffraction study on AANP

F.2 COANP

A solution of 2-chloro-5-nitropyridine (1.285g, 8.106mmol) and cyclooctylamine (1.078ml, 7.740mmol) in N-methylpyrolidinone (15ml) was treated with triethylamine (1.70ml). The light-orange solution was refluxed under argon protection for 2 hours. The brown oil was subjected to column chromatography (silica gel, hexane:EtOAc gradient elution). The layers were separated and the aqueous layer was extracted in EtOAc (3 x 20ml). The combined portions were dried ($MgSO_4$) and the solvent removed under reduced pressure. Unfortunately despite concerted efforts, all attempts to encourage COANP to crystallise failed.

Appendix G

Personal Development

G.1 Courses and Schools

- Diffraction and Scattering Methods (PG4)
  Dr A. E. Goeta

- Introduction to FORTAN Programming (408W)
  Prof. J. M. Hutson

- Advanced Skills Workshop (September 2005)
  Hosted by the National Crystallography Service, Southampton University.

- MSSC2004 - Ab Initio Modeling in Solid-State Chemistry
  (20th - 24th September 2004)
  Imperial University, London.

- BCA/CCG Intensive Teaching School in X-ray Structure Analysis
  (4th- 12th April 2005)
  Trevelyan College, University of Durham, Durham.

- IUCr Crystallographic Computing School (18th - 23rd August 2005)
  Held at Certosa di Pontignano, University of Sienna, Sienna, Italy.

- Advanced Skills Workshop (11th - 13th September 2006)
  Hosted by National Crystallography Service, Southampton University.

G.2 Departmental Seminars

- Homogeneous Catalysis: A Powerful Tool for Green Chemistry.
  Prof. Matthias Beller (Rostok University, Germany) – 22.10.03.

- Solution Chemistry, Speciation and Crystal Nucleation from Solutions.
  Prof. Roger Davy (UMIST) – 29.10.03.

- Pouring Oil on Troubled Water; Wetting and Phase Transitions in Surfactant/Alkane/Water Systems.
  Prof. Colin Bain (Oxford University) – 5.11.03.

- Infrared Imaging Comes of Age.
  Dr Robert Hoult (Perkin Elmer) – 19.11.03.

- Quantum Dots and their Potential Applications.
  Prof. Paul O'Brien (University of Manchester) – 4.2.04.

- Protein Folding and Mis-folding from an NMR Perspective.
  Prof. J. Waltho (University of Sheffield) – 18.2.04.

- Raman Microscopy: A Powerful Technique for Inorganic Chemsitry, Surface Analysis and Pigment Studies.
  Prof. Robin Clark (University College, London) – 25.2.04.

- Molecular Expression of Quantum Cellular Automata.
  Prof. Thomas P. Fehlner (University of Notre Dame) – 10.3.04.

- New Pd Catalysts for the Stille Reaction: Exploitation of a Serendipitous Discovery.
  Dr Ian Fairlamb (University of York) – 17.3.04.

- Molecule-based Magnets - New Chemistry and New Materials for the Millennium.
  Dr Joel S. Miller (University of Utah) – 25.4.05.

- Polymorphism in Organic Crystals and Pharmaceuticals.
  Prof. Ashwini Nangia (University of Hyderabad, India) – 2.6.05.

- First-Principles Predictions for Water Clusters and Condensed Phase.
  Krzysztof Szalewicz (University of Delaware) – 22.6.05.

- Gyrations and Gender.
  Prof. Susan Gibson (Imperial College, London) – 11.10.05.

- Atypical Responses of Functional Materials to External Stimuli.
  Prof. Komas Prassides (University of Durham) – 12.10.05.

- Precision Nano-chemical Engineering.
  Prof. Jon Preece (University of Birmingham) – 2.11.05.

- Making a Wholly Synthetic Muscle.
  Prof. Tony Ryan (University of Sheffield) – 15.11.05.

- Mass Spectrometry of Intact Non-covalent Complexes.
  Prof. Carol Robinson (University of Cambridge) – 22.6.06.

- Synthesis and Characterisation of Molecular Materials - Intermolecular Motifs in Crystal Packing of Luminescent Ga(III) Complexes.
  Prof. Alessandra Crispini (University of Calabria) – 24.8.06.

G.3 External Meetings and Conferences

- BCA CCG Autumn Meeting (12th November 2003)
  "Beyond Refinement; What Happens Next?"
  (Hosted by Accelrys, Cambridge Science Park)

- BCA PCG Winter Meeting (8th/9th December 2003)
  "Probing Structure at the Nanoscale:- Fact, Fiction or Hype?"
  (Hosted at Cosener's House, Abingdon, Oxon)

- 22nd Annual BCA Spring Meeting (5th - 8th April 2003)
  (Hosted at the Renold Building, UMIST, Manchester)
  Presented a poster "Charge Density Study of N,N-dimethyl-4-nitroaniline: A Closer Look at NLO Prototypes"

- 23rd Annual BCA Spring Meeting (11th - 14th April 2005)
  (Hosted at the James France Conference Centre, Loughborough University, Loughborough)
  Presented a poster entitled "Data Reduction from a Charge Density Perspective"

- IUCr Crystallographic Computing School (18th - 23rd August 2005)
  (Held at Certosa di Pontignano, University of Sienna, Sienna, Italy)
  Presented a talk entitled "XtalCommander: Interfacing to Crystal03 and Performing Distributed Calculations"

- Congress XX of the International Union of Crystallography (23rd - 31st August 2005)
  (Held at the Fortezza da Basso, Florence, Italy)
  Presented a poster entitled "Determination of 'Experimental' Wavefunctions from X-ray Diffraction Data"

- 24th Annual BCA Spring Meeting (3rd - 7th April 2006)
  (Hosted at the Faraday Complex, Lancaster Univeristy, Lancaster)
  Presented a poster entitled "Molecular Dipole Polarisabilities and Hyperpolarisabilities: Theoretical Determination and Preliminary Results"

G.4 Time Spent Away from Durham University

- 28th November 2003 - 1st Decemeber 2003
  ISIS Facility, CCLRC Rutherford Appleton Laboratory, Chilton, UK.
  Carried out a neutron-diffraction experiment on the behalf of Dr Jey Jau Lee on the instrument SXD. The purpose of the experiment was to obtain accurate nuclear positions and thermal parameters of triglycine sulphate (TGS) for use in a charge-density experiment.

- 11th - 15th February 2004
  SRS Facility, CCLRC Daresbury Laboratory, Warrington, UK.
  Assistance was provided to Victoria Money during the investigation of two

Fe spin-crossover compounds using the high-resolution powder diffractometer on Station 2.3. The allocated beam-time was spent collecting both RT and 120K datasets for $[FeL_2](BF_4)_2$ and $[FeL_2](ClO_4)_2$, where L = 2,6-di(pyrozol-1-yl)pyrazine.

- 25th March 2004 - 1st April 2004

  Institut Laue-Langevin, Grenoble, France.

  A neutron-diffraction experiment was performed on N,N-dimethyl-4-nitroaniline on the instrument D19 at a temperature of 100K, partly to test a new detector setup on the instrument. Unfortunately the crystal was at the boundaries of the acceptable size for the diffractometer and consequently not enough data with usable statistics were obtained.

- 10th - 17th May 2005

  Institut Laue-Langevin, Grenoble, France.

  A neutron-diffraction experiment was performed on N,N-dimethyl-4-nitroaniline on instrument D9 at 120K. For full details see Appendix C.

- 14th - 18th June 2005

  Institut Laue Langevin, Grenoble, France.

  A neutron diffraction experiment on 3-hydroxy-4-quinoxaline carboxylic acid was planned to be run on Vivaldi on behalf of Prof. A. Nangia (University of Hyderabad, India). Unfortunately technical difficulties prevented any data being collected during my time there. The purpose of the experiment was to look at obtain accurate hydrogen positions in order to facilitate the study of the short intramolecular hydrogen bond involving the keto and carboxylic acid substituent.

- 7th December 2005 - 28th February 2006

  University of Western Australia, Perth, Australia.

  Collaboration with D. Jayatilaka on wavefunction fitting calculations and calculation of (hyper)polarisabilities, much of which is discussed in this work.

Bibliography

[1] W.L. Bragg. *Proc. Camb. Phil. Soc.*, **17**, 43, (1914).

[2] A.E. Goeta and J.A.K. Howard. *Chem. Soc. Rev.*, **33**, 490, (2004).

[3] Cryostream Cooler. Oxford Cryosystems Ltd, Oxford, UK.

[4] A.E. Goeta, L.K. Thompson, C.L. Sheppard, C.W. Lehmann, J. Cosier, C. Webster, and J.A.K. Howard. *Acta Cryst.*, **C55**, 1243, (1999).

[5] W.R. Busing and H.A. Levy. *Acta Cryst.*, **22**, 457, (1967).

[6] T. Hahn (Editor). *International Tables for Crystallography, Vol. A.* Kluwer Academic Publishers, (1992).

[7] A.L. Patterson. *Z. Krist.*, **A90**, 517, (1935).

[8] *J. Chem. Phys.*, **4**, 381, (1936).

[9] C. Giacovazzo. *Direct Methods in Crystallography.* Academic Press, London, (1980).

[10] P. Coppens, T.M. Sabine, R.G. Delaphane, and J.A. Ibers. *Acta Cryst.*, **B25**, 2451, (1969).

[11] E. Clementi and D.L. Raimondi. *J. Chem. Phys.*, **38**, 2686, (1969).

[12] E. Clementi and C. Roetti. *At. Data Nucl. Data Tables*, **14**, 177, (1974).

[13] R.F. Stewart. *J. Chem. Phys.*, **51**, 4569, (1969).

[14] R.F. Stewart. *J. Chem. Phys.*, **58**, 1668, (1973).

[15] N.K. Hansen and P. Coppens. *Acta Cryst.*, **A34**, 909, (1978).

[16] T. Koritsanszky, P.R. Mallinson, S. Howard, A. Volkov, P. Macchi, Z. Su, C. Gatti, T. Richter, L.J. Farrugia, and N.K. Hansen. *XD: A Computer Program Package for Multipole Refinement and Analysis of Electron Densities from Diffraction Data.* Version 4.09, (2003).

[17] W.H.E. Schwarz, L. Mensching, P. Valtazanos, and W.von Niessen. *Int. J. Quantum Chem.*, **30**, 439, (1986).

[18] G.N. Ramachandran and R. Shrinivasan. *Nature*, **90**, 159, (1961).

[19] A.E. Haouzi, N.K. Hansen, C.L. Henaff, and J. Protas. *Acta Cryst.*, **A52**, 291, (1996).

[20] R.F.W. Bader. *Atoms in Molecules: A Quantum Theory.* Oxford University Press, (1990).

[21] A. Dianoux and G. Lander. *Neutron Data Booklet.* ILL, (2002).

[22] C. Giacovazzo, H.L. Monaco, D. Viterbo, F. Scordari, G. Gilli, G. Zanotti, and M. Catti. *Fundamentals of Crystallography.* Oxford University Press, (1994).

[23] P. Coppens. *X-Ray Charge Densities and Chemical Bonding.* Oxford University Press, (1997).

[24] C.C. Wilson. *Single Crystal Neutron Diffraction from Molecular Materials.* World Scientific, (2000).

[25] J. Baruchel, J.L. Hodeau, M.S. Lehmann, J.R. Regnard, and C. Schlenker (Editors). *Neutron and Synchrotron Radiation for Condensed Matter Studies: Volume 1, Theory, Instruments and Methods.* EDP Sciences - Springer-Verlag, (1993).

[26] R. McWeeny. *Methods of Molecular Quantum Mechanics.* Academic Press, London, (1992).

[27] P.W. Atkins and R.S. Friedman. *Molecular Quantum Mechanics.* Oxford University Press, Oxford, (2004).

[28] T.H. Dunning. *J. Chem. Phys.*, **53**, 2823, (1970).

[29] T.H. Dunning. *J. Chem. Phys.*, **90**, 1007, (1989).

[30] R. Ditchfield, W.J. Hehre, and J.A. Pople. *J. Chem. Phys.*, **54**, 724, (1971).

[31] S.F. Boys and F. Bernardi. *Mol. Phys.*, **19**, 553, (1970).

[32] V.R. Saunders, R. Dovesi, C. Roetti, R. Orlando, C. M. Zicovich-Wilson, N.M. Harrison, K. Doll, B.Civalleri, I. Bush, Ph. D'Arco, and M. Llunell. *CRYSTAL2003 User's Manual.* University of Torino, Torino, (2003).

[33] C. Pisani, R. Dovesi, and C. Roetti. *Hartree-Fock Ab Initio Treatment of Crystalline Systems*, volume Vol. 48. Springer-Verlag, (1988).

[34] P. Hohenberg and W. Kohn. *Phys. Rev. B*, **136**, 864, (1964).

[35] Y.A. Abramov. *Acta Cryst.*, **A53**, 264, (1997).

[36] D. Jayatilaka and D.J. Grimwood. *Acta Cryst.*, **A57**, 76, (2001).

[37] D. Jayatilaka, D.J. Grimwood, A. Lee, A. Lemay, A. J. Russell, C. Taylor, S.K. Wolff, P. Cassam-Chenaï, A. Whitten, and M.J. Turner. *Tonto (Version 2.X).* UWA, Perth, Australia, (2006).

[38] D. Jayatilaka. *Phys. Rev. Lett.*, **80**, 798, (1998).

[39] D.J. Grimwood and D. Jayatilaka. *Acta Cryst.*, **A57**, 87, (2001).

[40] D.J. Grimwood, I. Blytheway, and D. Jayatilaka. *J. Comput. Chem.*, **24**, 470, (2003).

[41] J.D. Wright. *Molecular Crystals.* Cambridge University Press, Cambridge, (1995).

[42] M.G. Sylvain and I.G. Csizmadia. *Chem. Phys. Lett.*, **136**, 575, (1987).

[43] A.E. Whitten, D. Jayatilaka, and M.A. Spackman. *J. Phys. Chem.*, **125**, 174505, (2006).

[44] M.P. Bogaard and B.J. Orr (Editor: A.D. Buckingham). *MTP International Review of Science, Physical Chemistry Series 2, Vol. 2 pp 149.* Butterworths, London, (1975).

[45] J.W. Rohleder and R.W. Munn. *Magnetism and Optics of Molecular Materials.* John Wiley & Sons, Chichester, (1992).

[46] A. Fkyerat, A. Guelzim, F. Baert, W. Paulus, G Heger, J. Zyss, and A. Périgaud. *Acta Cryst.*, **B51**, 197, (1995).

[47] A. Fkyerat, A. Guelzim, F. Baert, J. Zyss, and A. Périgaud. *Phys. Chem. Rev. B*, **53**, 16236, (1996).

[48] F. Hamzaoui, A. Zanoun, and G. Vergoten. *J. Mol. Struct.*, **697**, 17, (2004).

[49] A. Chouaih, F. Hamzaoui, and G. Vergoten. *J. Mol. Struct.*, **738**, 33, (2005).

[50] A.D. Buckingham. *Adv. Chem. Phys.*, **12**, 107, (1967).

[51] C. Huiszoon. *Mol. Phys.*, **58**, 865, (1986).

[52] A. Unsöld. *Z. Phys.*, **43**, 563, (1927).

[53] A.E. Whitten. *Ph.D. Thesis.* University of New England, Australia, (2005).

[54] M. Born and E. Wolf. *Principles of Optics. Electromagnetic Theory of Propagation, Interference and Diffraction of Light.* Cambridge University Press, Cambridge, (1999).

[55] M.J. Frisch, G.W. Trucks, H.B. Schlegel, G. E. Scuseria, M.A. Robb, J.R. Cheeseman, J. Montgomery, T. Vreven, K.N. Judin, J.C. Burant, J.M. Millam, S.S. Iyengar, J. Tomasi, V. Barone, B. Mennucci, M. Cossi, G. Scalmani, N. Rega, G.A. Petersson, H. Nakajima, Y. Honda, O. Kitao, H. Nakai, M. Klene, X. Li, J.E. Knox, H.P. Hratchian, J.B. Cross, V. Bakken, C. Adamo, J. Jaramillo, R. Gomperts, R.E. Stratmann, O. Yazyev, A.J.

Austin, R. Cammi, C. Pomelli, J.W. Ochtershi, P.Y. Ayala, K. Morokuma, G.A. Voth, P. Salvador, J.J. Dannenberg, V.G. Zakrzewski, S. Dapprich, A.D. Daniels, M.C. Strain, O. Farkas, D.K. Malick, A.D. Rabuck, K. Raghavachari, J.B. Foresman, J.V. Ortiz, Q. Cui, A.G. Baboul, S. Clifford, J. Ciolowski, B.B. Stefanov, G. Liuand A. Liashenko, P. Piskorz, I. Komaromi, R.L. Martin, D.J. Fox, T. Keith, M.A. Al-laham, C. Y. Peng, A. Nanayakkara, M. Challacombe, P.M.W. Gill, B. Johnson, W. Chen, M.W. Wong, C. Gonzalez, and J.A. Pople. *Gaussian.* Gaussian Inc, Wallingford CT, (2004).

[56] S.K. Kurtz and T.T. Perry. *J. Appl. Phys.*, **39**, 3798, (1968).

[57] R.D. Brown, P.D. Godfrey, and J. Storey. *J. Mol. Spectrosc.*, **58**, 445, (1975).

[58] S.T. Howard, M.B. Hursthouse, C.W. Lehmann, P.R. Mallinson, and C.S. Frampton. *J. Chem. Phys.*, **97**, 5616, (1992).

[59] A. Volkov. *Ph.D. Thesis.* University of New York, Buffalo, (2000).

[60] H.B. Bürgi, S.C. Capelli, A.E. Goeta, J.A.K. Howard, M.A. Spackman, and D.S. Yufit. *Chem. Eur. J.*, **8**, 3512, (2002).

[61] H. Birkedal, D. Madsen, R.H. Mathiesen, K. Knudsen, H.P. Weber, P. Pattison, and D. Schwarzenbach. *Acta Cryst.*, **A60**, 371, (2004).

[62] S. Swaminathan, B.M. Craven, and R.K. MuMullan. *Acta Cryst.*, **B40**, 300, (1984).

[63] A.E. Whitten, P. Turner, W.T. Klooster, R.O. Piltz, and M.A. Spackman. *J. Phys. Chem.*, **110**, 8763, (2006).

[64] G.L.D. Ritchie and J.N. Watson. *Chem. Phys. Lett.*, **322**, 143, (2000).

[65] R. Gay and B. Lemanceau. *Cahiers Phys.*, **74**, 38, (1956).

[66] A. Samoc. *J. Appl. Phys.*, **94**, 6167, (2003).

[67] P.J. Bounds and R.W. Munn. *Chem. Phys.*, **24**, 343, (1977).

[68] G.A. Jeffrey, J.R. Ruble, R.K. McMullan, and J.A. Pople. *Proc. R. Soc. London, Ser.*, **414**, 47, (1987).

[69] P.V. Vidakovic, M. Coquillay, and F. Salin. *J. Opt. Soc. Am. B: Opt. Phys.*, **4**, 998, (1987).

[70] J.M. Halbout, S. Blit, W. Donaldson, and C.L. Tang. *IEEE J. Quantum Electron.*, **15**, 1176, (1979).

[71] H. Birkedal. *Ph.D. Thesis.* University of Lausanne, Lausanne, (2000).

[72] C.H. Grossman and A.F. Garito. *Mol. Cryst. Liq. Cryst.*, **168**, 255, (1989).

[73] G.F. Lipscomb, A.F. Garito, and R.S. Nerang. *J. Chem. Phys.*, **75**, 1509, (1981).

[74] H. Graafsma, A. Paturle, L. Wu, H.S. Sheu, J. Majewski, G. Poorthuis, and P. Coppens. *Acta Cryst.*, **A48**, 113, (1992).

[75] P.A. Norman, D. Bloor, J.S. Obhi, S.A. Karaulov, M.B. Hursthouse, P.V. Kolinsky, R.J. Jones, and S.R. Hall. *J. Opt. Soc. Am.*, **B6**, 1013, (1987).

[76] J.C. Baumert, R.J. Twieg, G.C. Bjorklund, J.A. Logan, and C.W. Dirk. *Appl. Phys. Lett.*, **51**, 1484, (1987).

[77] T. Kondo, N. Ogasawara, and R. Ito. *Acta Cryst.*, **C44**, 102, (1988).

[78] T. Kondo, R. Morita, N. Ogasawara, S. Umegaki, and R. Ito. *Jap. J. Appl. Phys.*, **28**, 1622, (1989).

[79] R.J. Twieg and C.W. Dirk. *J. Chem. Phys.*, **85**, 3537, (1986).

[80] D.S. Yufit. *private communication*, (2006).

[81] P. Keroc, M. Zgonik, K. Sutter, Ch. Bosshard, and P. Günter. *J. Opt. Soc. Am. B*, **7**, 313, (1990).

[82] M. Born and E. Wolf. *Principles of Optics.* Pergamon, Oxford, (1980).

[83] R.D. Clark, A. Romero, O.Y. Borbulevych, M.Y. Antipin, V.N. Nesterov, and T.V. Timofeeva. *Acta Cryst.*, **C56**, 336, (2000).

[84] R.T. Bailey, F.R. Cruickshank, S. Lochran, D. Pugh, J.N. Sherwood and.J. Langley, and J.D. Wallis. *Bull. Mater. Sci.*, **22**, 421, (1999).

[85] T. Kondo, F. Akasi, M. Kumagai, and R. Ito. *Opt. Rev.*, **2**, 128, (1995).

[86] K. Sutter, Ch. Bosshard, W.S. Wang, G. Surmely, and P. Günter. *Appl. Phys. Lett.*, **53**, 1779, (1988).

[87] C. Bosshard, K. Sutter, P. Pretre, J. Hulliger, M. Flörsheimer, P. Kaatz, and P. Günter. *Organic Nonlinear Optical Materials.* Gordon and Breach, Switzerland, (1995).

[88] M.S. Paley, J.M. Harris, H. Looser, J.C. Baumert, G.C. Bjorklund, D. Jundt, and R.J. Twieg. *J. Org. Chem.*, **54**, 3774, (1989).

[89] C. Bosshard, G. Knöpfle, P. Pretre, and P. Günter. *J. Appl. Phys.*, **71**, 1594, (1992).

[90] C.C. Teng and A.F. Garito. *Phys. Rev. B*, **28**, 6766, (1983).

[91] D. Jayatilaka and D.J. Grimwood. *Acta Cryst.*, **A58**, 232, (2002).

[92] J.M. Cole, A.E. Goeta, J.A.K. Howard, and G.J. McIntyre. *Acta Cryst.*, **B58**, 690, (2002).

[93] M.R. Probert. *private communication*, (2006).

[94] T.C.W. Mac and J. Trotter. *Acta Cryst.*, **18**, 68, (1965).

[95] O.Y. Borbulevych, R.C. Clark, A. Romero, L. Tan, M. Antipin, V.N. Nesterov, B.H. Cardelino, C.E. Moore, M. Sanghadasa, and T. Timofeeva. *J. Mol. Struct.*, **604**, 73, (2002).

[96] M.J.S. Dewar, E.G. Zoebisch, E.F. Healy, and J.J.P. Stewart. *J. Am. Chem. Soc.*, **107**, 3903, (1985).

[97] S.R. Marder, D.N. Beraton, and L.T. Cheng. *Science*, **252**, 103, (1991).

[98] S.R. Marder, J.W. Perry, B.G. Tiemann, C.B. Gorman, S. Gilmour, S.L. Biddle, and G.A. Bourhill. *J. Am. Chem. Soc.*, **115**, 2524, (1993).

[99] Bruker. *SMART v5.629.* Bruker Analytical X-ray Systems, Madison, WI, (2003).

[100] Bruker. *SAINT v6.45A.* Bruker Analytical X-ray Systems, Madison, WI, (2003).

[101] R.H. Blessing. *Acta Cryst.*, **A51**, 33, (1995).

[102] Bruker. *SADABS.* Bruker Analytical X-ray Systems, Madison, WI, (2002).

[103] G.M. Sheldrick. *SHELXL97.* University of Göttingen, Germany, (1997).

[104] A.J.C. Wilson (Editor). *International Tables for Crystallography, Vol. C.* Kluwer Academic Publishers, (1992).

[105] R.F. Stewart, E.R. Davidson, and W.T. Simpson. *J. Chem. Phys.*, **42**, 2175, (1965).

[106] R.S. Gopalan, G.U. Kulkarni, and C.N.R. Rao. *Chem. Phys. Chem.*, **1**, 127, (2000).

[107] G.U. Kulkarni, P. Kumaradhas, and C.N.R. Rao. *Chem. Mater.*, **10**, 3498, (1998).

[108] P. Munshi and T.N.G. Row. *Acta Cryst.*, **B58**, 1011, (2002).

[109] A. Volkov, G. Wu, and P. Coppens. *J. Synchrotron Rad.*, **6**, 1007, (1999).

[110] R.S. Gopalan, G.U. Kulkarni, M. Ravi, and C.N.R. Rao. *New J. Chem.*, **25**, 1008, (2001).

[111] A.E. Whitten and M.A. Spackman. *Acta Cryst.*, **B62**, 875, (2006).

[128] T. Koga and A.J. Thakkar. *Theor. Chim. Acta*, **85**, 391, (1993).

[129] P. Günter, Ch. Bosshard, K. Sutter, H. Arend, G. Chapuis, R.J. Twieg, and D. Dobrowolski. *Appl. Phys. Lett.*, **50**, 486, (1987).

[130] A.L. Spek. *Acta Cryst.*, **A46**, C–34, (1990).

[131] A.L. Spek. *PLATON - A Multipurpose Crystallographic Tool.* Utrecht University, Utrecht, The Netherlands, (2002).

[132] D.S. Yufit, M.J. Turner, and J.A.K. Howard. *Acta Cryst.*, **E62**, 1237, (2006).

[112] W.H. Press, S.A. Teukolsky, W.T. Vetterling, and B.P. Flannery. *Numerical Methods in Fortran 77, 2nd Ed. pp 279-280.* Cambridge University Press, (1992).

[113] D. Applebaum. *Probability and Information: an Integrated Approach.* Cambridge University Press, (1996).

[114] F.L. Hirshfeld. *Theor. Chim. Acta*, **44**, 129, (1977).

[115] J.J. McKinnon, A.S. Mitchell, and M.A. Spackman. *Chem. Eur. J.*, **4**, 2136, (1998).

[116] J.J. McKinnon, M.A. Spackman, and A.S. Mitchell. *Acta Cryst.*, **B60**, 627, (2004).

[117] M.A. Spackman and P.G. Byrom. *Chem. Phys. Lett.*, **267**, 215, (1997).

[118] M.A. Spackman and J.J McKinnon. *Cryst. Eng. Comm.*, 378, (2002).

[119] S.K. Wolff, D.J. Grimwood, J.J. Mckinnon, D. Jayatilaka, and M.A. Spackman. *Crystal Explorer v1.5.1.* University of Western Australia, Perth, Australia, (2005).

[120] http://www.ill.fr/YellowBook/D9.

[121] J. Archer and M.S. Lehmann. *J. Appl. Cryst.*, **19**, 456, (1986).

[122] J.R. Allibon. *MAD.* ILL, Grenoble, France, (2005).

[123] A. Fihol. *Rafin, Rafnb, Rafdb, Rafd19, Rafd9.* ILL Technical Report 87FI19T.

[124] C. Wilkinson and G.J. McIntyre. *RACER.* ILL, Grenoble, France, (2005).

[125] G.J. McIntyre. *DATAP.* ILL, Grenoble, France, (2005).

[126] P. Coppens, L. Leiseowitz, and D. Rabinovich. *Acta Cryst.*, **18**, 1035, (1965).

[127] A.J. Thakkar, T. Koga, M. Saito, and H. Re. *Int. J. Quantum Chem.,Quantum Chem. Symp.*, **27**, 343, (1993).